Doctoral dissertation

Cell Design of Solar Seawater Battery and its Anode Material Development

Jinhyup Han

Department of Energy Engineering

(Battery Science and Technology)

Graduate School of UNIST

2019

Cell Design of Solar Seawater Battery and its Anode Material Development

Jinhyup Han

Department of Energy Engineering
(Battery Science and Technology)

Graduate School of UNIST

Cell Design of Solar Seawater Battery and its Anode Material Development

A dissertation
submitted to the Graduate School of UNIST
in partial fulfillment of the
requirements for the degree of
Doctor of Philosophy

Jinhyup Han

06/13/2019 of submission

Approved by

Advisor
Youngsik Kim

Cell Design of Solar Seawater Battery and its Anode Material Development

Jinhyup Han

This certifies that the dissertation of Jinhyup Han is approved.

06/13/2019

signature

Advisor: Youngsik Kim

signature

Yunseok Choi

signature

Kwanyong Seo

signature

Kwangjin An

signature

Ji-Wook Jang

Abstract

Lithium-ion batteries (LIBs) have become the most important rechargeable battery for portable devices, electric vehicles (EVs) and large scale energy storage systems (ESSs) with high energy density and long cycle life. However, such an increasing demand for LIBs may induce a price increase of Li, Co-containing law materials and anode materials. Here we present a new battery system that is not affected by the price of cathode materials and low cost Pb-based anode materials for post LIBs.

First, we introduce a new concept energy storage device that uses natural seawater as a cathode material. Seawater batteries store sodium (Na) ions from the seawater into the anode side during charging and then the harvested Na metal can be discharged with seawater to produce electricity. We discuss the cell design and development of coin-type seawater batteries, and the novel use of TiO_2 nanotubes as a photo-anode to increase voltage efficiency. The cell design of seawater batteries and improved voltage efficiencies are mainly discussed.

Second, we present Pb-based composite anode materials for sodium-ion batteries (SIBs) and seawater batteries. Lead and lead oxides have advantages of low cost and high volumetric energy density. Here, we report Pb-O-C composite anodes synthesized by simple a high energy ball milling process. The electrochemical data tested in sodium cells show higher reversible capacity and improved cycle stability when compared to previously reported data of lead and lead oxides materials. The reaction mechanism and effect of composite structure are discussed in detail.

Studies of this novel solar seawater battery and Pb-based anode materials are in the early stage and further performance improvements are under development. However, we expect they to have global application for low cost ESSs in the near future.

Contents

List of Figures

List of Tables

List of publications

I contributed to the following publications during my PhD course.

Peer-reviewed publications

1. K. Kim, **J. Han**, JS Park, J. Lee "Preparation and evaluation of activated carbon supported catalysts derived waste materials for hybrid type Na-air battery", *Materals Letters*, 2019, **245**, 6-9
2. **J. Han**, S. Hwang, W. Go, Senthilkumar, S. T**.**, D. Jeon, and Y. Kim, "Development of coin-type cell and engineering of its compartments for rechargeable seawater batteries", *Journal of Power Sources*, 2018, **374**, 24-30
3. S. Hwang, JS Park, YI Kim, W. Go, **J. Han**, YJ Kim, and Y. Kim, "Rechargeable seawater battery-from concept to applications", *Advanced Materials*, 2018, e1804936
4. P. Manikandan, K. Kishor, **J. Han**, and Y. Kim, "Advanced Perspective on Synchronized Bifunctional Activities of P2-Type Material to Implement Interconnected Voltage Profile for Seawater Battery", *Journal of Materials Chemistry A,* 2018, **6**, 11012-11021
5. Senthilkumar, S. T**.**, H. Bae**,** **J. Han**, and Y. Kim, "Enhancing Capacity Performance by Utilizing the Redox Chemistry of the Electrolyte in a Dual-Electrolyte Sodium Ion Battery", *Angewandte Chemie,* 2018, **57**, 5335-5339
6. Senthilkumar, S. T**.,** **J. Han**, JS Park, S. Hwang, Y. Kim, "Energy efficient Na-aqueous-catholyte redox flow battery", *Journal of Power Sources*, 2017, **12**, 324-330
7. K. Kim, S. Hwang, JS Park, **J. Han**, J. Kim, Y. Kim, "Highly improved voltage efficiency of seawater battery by use of chloride ion capturing electrode", *Journal of Power Sources*, 2016, **313**, 16-50

List of patents

Patent registration

1. Sealing machine for coin-type seawater battery, Y. Kim, **J. Han**, 2018-12-31, 10-1935903, S. Korea
2. Rechargeable battery module using ion containing solution, Y. Kim, **J. Han**, W. Go, 2018-10-15, 10-1909890, S. Korea
3. Coin-type module & integrated module for grid scale energy storage, Y. Kim, **J. Han**, W. Go, 2018-05-31, 10-1865383, S. Korea
4. Coin cell Type seawater battery and its manufacturing method, Y. Kim, **J. Han**, 2016-11-07, 10-1675481, S. Korea
5. Coin type rechargeable seawater battery for jig and module, Y. Kim, **J. Han**, S. Hwang, 2016-11-07, 10-1675482, S. Korea

Patent application

1. Battery system for hydrogen gas production, Y. Kim, J. Jang, S. Hwang, **J. Han**, 2019-02-26, KO 10-2019-002336
2. Solar seawater battery & unassisted photo-charging solar seawater battery, Y. Kim, J. Lee, J. Kim, S. Hwang, **J. Han**, 2018-10-10, KO 10-2018-0118465
3. Bifunctional P2 type high energy $Na_{0.5}Co_{0.5}Mn_{0.5}O_2$ Electrocatalyst for seawater battery, Y. Kim, P. M, **J. Han**, 2018-03-30, KO 10-2018-0038505
4. Sealing machine for coin-type seawater battery, Y. Kim, **J. Han**, 2017-12-21, EPO16800298.8
5. Coin type rechargeable battery, and method for manufacturing the same, Y. Kim, **J. Han,** S. Hwang 2017-11-27, JP 100121382
6. Coin type rechargeable battery, and method for manufacturing the same, Y. Kim, **J. Han,** S. Hwang 2017-11-24, US 15/576,762
7. Cointype module & integrated module for grid scale energy storage, Y. Kim, W. Go, **J. Han**,

2017-04-03, JP 2017-518095

8. Cointype module & integrated module for grid scale energy storage, Y. Kim, **J. Han**, W. Go, 2017-03-09, US 15/509975
9. Sodium-ion hybrid electrolyte redox flow battery, Y. Kim, S.T. senthilkumar, **J. Han**, 2017-07-10, KO 10-2017-0087289
10. Sealing machine for coin-type seawater battery, Y. Kim, **J. Han**, 2017-01-16, KO 10-2017-0007037
11. Rechargeable battery module using ion containing solution, Y. Kim, W. Go, **J. Han**, 2016-09-01, KO 10-2016-0112516P
12. Cointype module & integrated module for grid scale energy storage, Y. Kim, W. Go, **J. Han**, 2016-06-03, KO 10-2016-0069586
13. Seawater secondary battery and seawater secondary battery system, Y. Kim, H. Kim, M. Jung, J. Park, **J. Han,** 2016-05-24, US 15/162,753
14. Coin type rechargeable seawater battery for jig and module, Y. Kim, **J. Han,** S. Hwang, 2016-05-13, KO 10-2016-0059039
15. Coin type rechargeable battery, and method for manufacturing the same, Y. Kim, K. Kim, M. Jung, H. Kim, **J. Han,** 2015-05-26, KO 10-2015-0073108
16. Seawater secondary battery and seawater secondary battery system, Y. Kim, H. Kim, M. Jung, J. Park, **J. Han,** 2014-11-27, KO 22-2014-0167764

Conference contributions

International

1. *EES Spring Meeting,* Seattle, U.S., May **2018**, "Development of coin-type cell and engineering of its compartments for rechargeable seawater batteries", Oral presentation
2. *UK-Korea symposium,* London, U.K., **2016**, "Cell design of coin-type seawater batteries", Poster presentation

Domestic

3. *The Korean Institute of Electrical Engineers symposium,* Gwang-ju, Korea, November **2017**, "Cell design of coin-type seawater batteries", Oral presentation
4. *Energy symposium,* Dae-jeon, Korea, September **2017**, "Development of coin-type cell and engineering of its compartments for seawater batteries", Oral presentation

Awards

1. "**Grand prize Award**" *The Korean Institute of Electrical Engineers symposium*, Gwang-ju, Korea, November **2017**
2. "**Future Jackpot Award**" *JETS conference*, Dae-jeon, Korea, January **2017**
3. *I-corps program*(Certificates), Washington D.C., USA, July **2016**
4. "**Bixpo creative prize**" *BIXPO 2016 Bitgaram Internatioal Exposition of Electric Power Technology International Invention Fair*, Gwang-ju, Korea, November **2016**
5. "**Special awards**" *BIXPO 2016 Bitgaram Internatioal Exposition of Electric Power Technology International Invention Fair*, Gwang-ju, Korea, November **2016**

Chapter 1

Introduction of energy storage systems (ESSs)

1.1 Needs for ESSs

Excessive emissions of CO_2 from the combustion of fossil fuels, such as coal or oil, are the main causes of climate change and environmental pollution, which are the global issues to be solved for a sustainable society.[1-4] These environmental concerns, as well as growing energy demands, require the development of new types of systems and technologies for energy conversion and storage based on renewable energy (Figure 1). However, renewable sources, such as wind and solar, are variable; and renewable power generation, dependent on their sources, provide only intermittent electrical energy.[5-9] Figure 2 shows solar generated electricity during daytime, but much less electrical energy is generated on night-time. Furthermore, power generation by renewable sources are highly affected by the region. Therefore, to satisfy the increasing demand for renewable energy resources, other types of ESSs are essential than intermittent and locally affected systems.

The main purpose of ESSs is to store renewable energy efficiently and use it with high energy efficiency on demand.[10-12] Currently, Lithium-ion batteries (LIBs) are considered as one of the next-generation batteries for the ESSs market.[13-15]

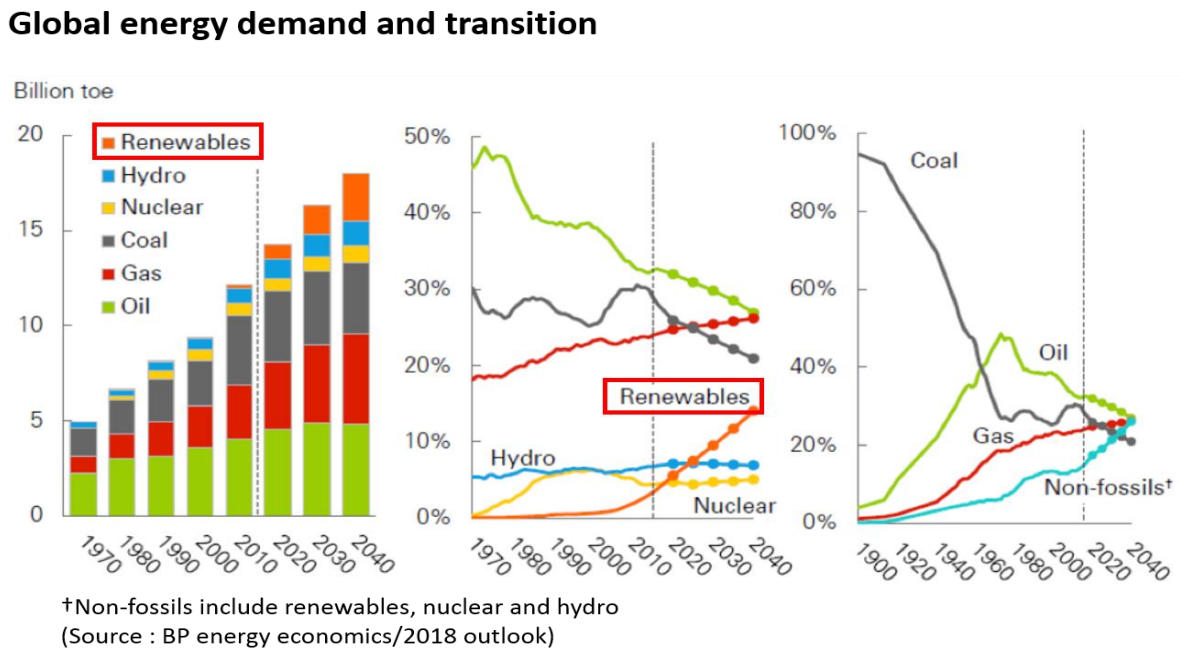

Figure 1. Increasing demand for renewable energy.

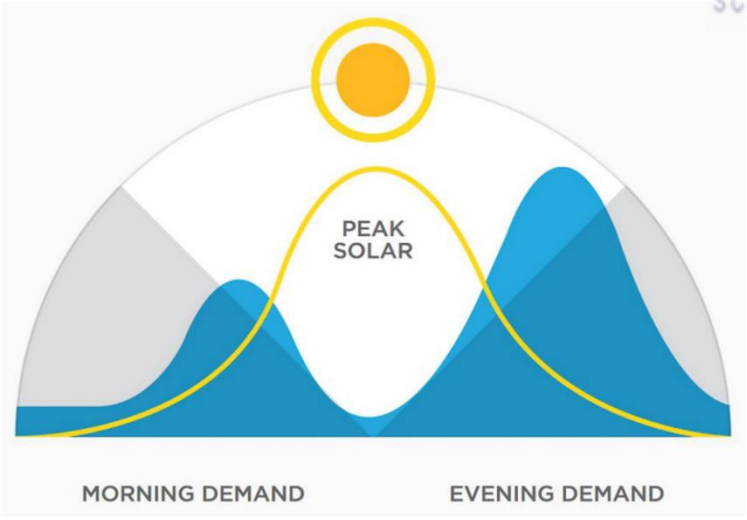

(Source : Tesla/EXTREME TECH)

Figure 2. Renewable power generation provided intermittently electricity.

1.2 Principle and challenges of lithium-ion batteries

Figure 3 represents a basic Li-ion battery, which is composed of a positive (cathode) and a negative electrode (anode) separated by a liquid electrolyte, enabling ion transfer between the two electrodes.[16, 17] To maximize energy density, the electrodes are in close proximity, but electronically isolated by a separator of porous plastic film to avoid a short circuit. During charge and discharge of the battery, lithium ions transfer between the anode and cathode across the electrolyte, while electrons simultaneously move through external circuit, generated by redox reactions at the cathodes.[18] More specifically, when the battery circuit is closed without externally applying a potential or current, charge can only flow the anode to the cathode in a spontaneous manner because the former has a higher chemical potential than the latter. Therefore, this process is spontaneous and it delivers energy to the circuit. If the battery can be charged by an external power source, Li^+ in the cathode move to the anode while electrons flow to the anode through an external wire to maintain neutrality.[19] Graphite has a layered structure and it is electronically reduced in an aprotic organic electrolyte containing lithium salts and lithium ions are intercalated (or doped) between the layers of graphite on charging. On discharging, Li ions are de-intercalated from the layers of graphite and inserted to the positive electrode of layered structure $LiCoO_2$, as shown in Figure 3. In the $LiCoO_2$/graphite cell system, the overall cell equation is as follows:[20-22]

$$LiCoO_2 + Li_{a-dx}C \rightleftharpoons Li_{1-dx}CoO_2 + Li_aC$$

(Charging: to the right, discharging: to the left in direction)

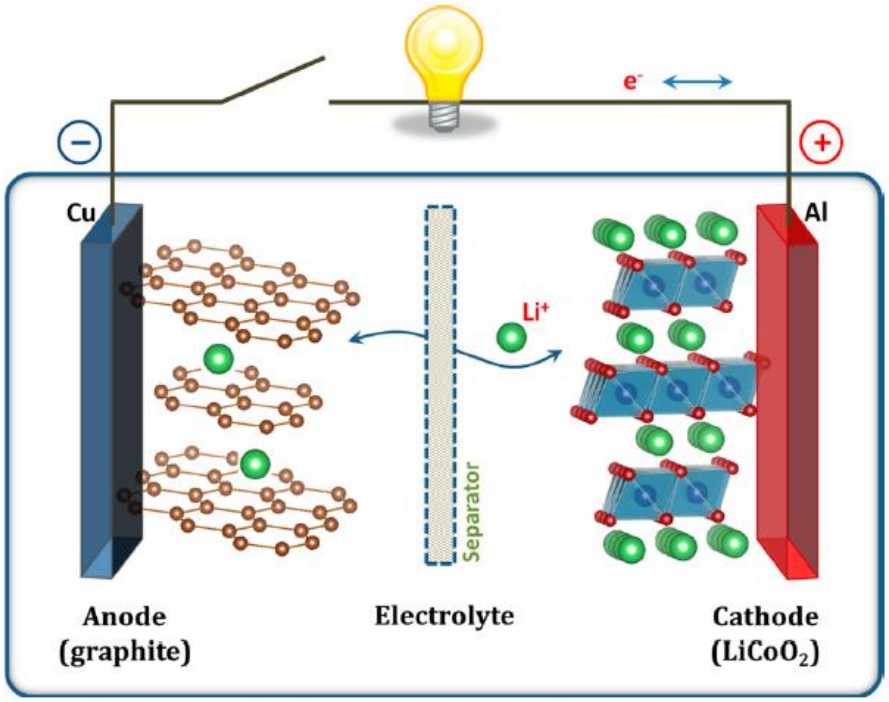

Figure 3. Schematic illustration of the commonly used Li-ion battery based on a graphite anode and a $LiCoO_2$ cathode.[16]

Among various electrochemical energy storage systems (e.g., lithium-ion, metal-air,[23, 24] redox-flow batteries[25-27]), the LIBs show good electrochemical performance, such as high voltage with low redox potential ($E^{\circ}(Li^{+}/Li)$= -3.04V vs. SHE) and high energy density (~300 Wh/kg), long cyclability (≥2,000 times) and competitive energy cost (250–400 \$ kWh^{-1})[11, 28, 29]. Because of these various advantages, LIBs are being used in a wide variety of areas, from ESSs to electrical vehicles (EVs) and portable devices (Figure 4). However, their long-term sustainable use may be limited because of the steeply rising prices of lithium, cobalt-containing raw materials and anode materials due to the increasing demand for LIBs in electric vehicles and large-scale ESSs (Figure 5). Also, the scarcity of lithium and cobalt resources significantly limits future ESS applications. Therefore, in order to solve the problem of price in such cathodes, recent researches have focused on reducing the cobalt ratio in the cathode or developing cobalt-free cathode materials.[30-33]

We approach different ways and would like to introduce a new battery system that uses natural seawater as its cathode, which does not rely on expensive lithium and cobalt materials.

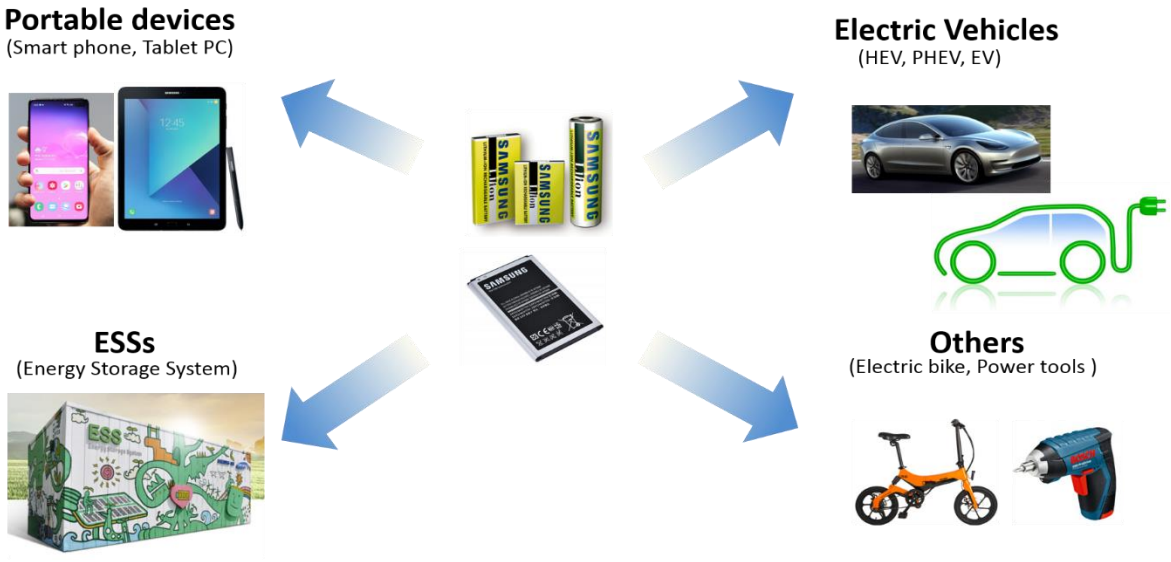

(Source : SAMSUNG, TESLA, BOSCH)

Figure 4. Various applications of LIBs

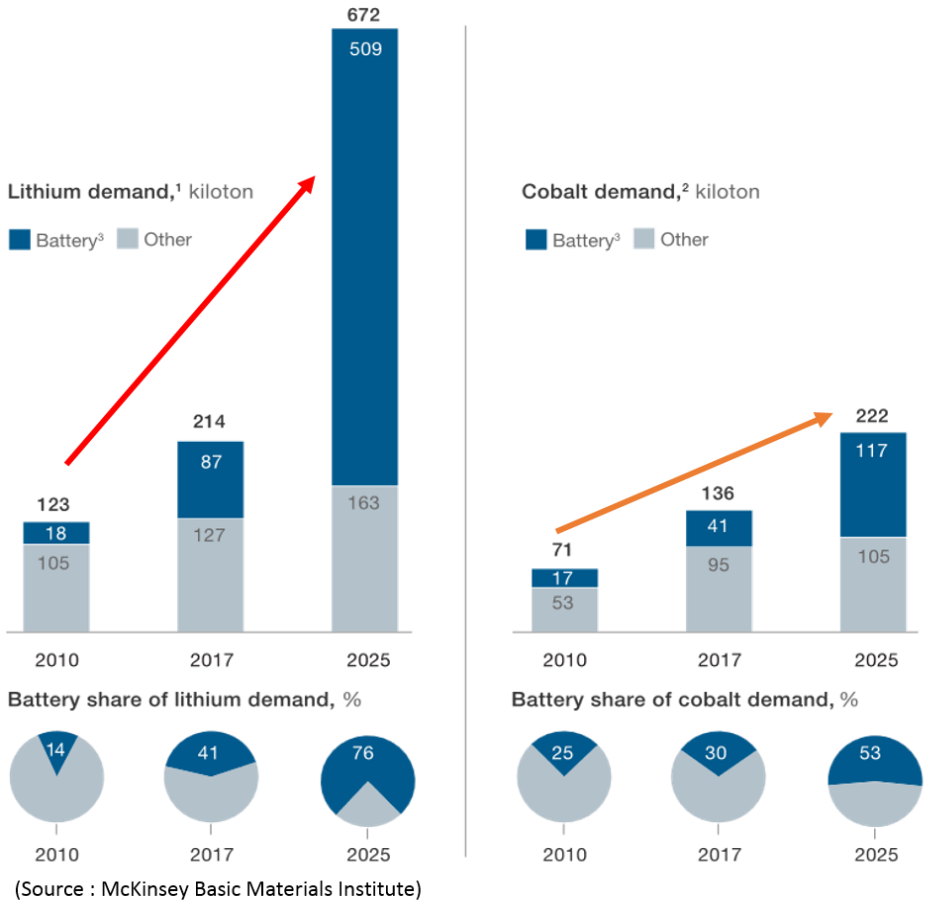

(Source : McKinsey Basic Materials Institute)

Figure 5. Demand for lithium and cobalt will continue to evolve.

1.3 Seawater batteries

Our group has recently introduced a new battery system that is not affected by the price of cathode materials by using earth-abundant, natural seawater as the active materials.[34-59] Seawater batteries store electrical energy in chemical bonds of Na via the oxidation of seawater on the cathode side and the reduction of Na^+ ions extracted from seawater on the anode side. When discharging, the battery converts the stored chemical energy into electric energy by transferring Na^+ ions back into seawater, while reducing seawater. The open structured cathode configuration, which enables continuous supply of fresh seawater, allows for the unlimited utilization of seawater during the charge/discharge operation. In principle, the use of natural seawater as the cathode material in batteries can significantly reduce material and manufacturing costs (considerable amount of Na^+ ions (~0.47 M) in seawater, Figure 6).[60] In this regards, seawater batteries would be cheaper and more environmentally benign than existing batteries, including LIBs, thus being an attractive option for low-cost, large-scale ESSs applications.

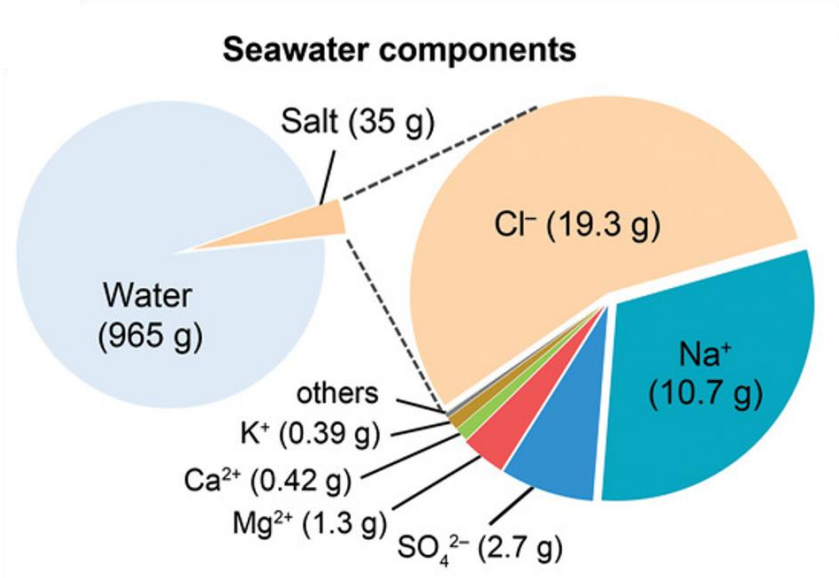

Figure 6. Composition of seawater containing of ~0.47 M of NaCl.[60]

Figure 7 illustrates the schematic of the basic structure and the components of a seawater battery cell. The cell composed of two compartments, an anode and a cathode, which are separated by a NASICON ceramic electrolyte ($Na_3Zr_2Si_2PO_{12}$). The anode compartment consists of a sodium metal anode attached to a current collector and a non-aqueous liquid electrolyte. The cathode part is composed of a cathode current collector and seawater catholyte. Utilizing seawater that contains Na^+ and Cl^- ions, the batteries operate based on the redox reactions of Na^+ ions at the anode side and the simultaneous evolution/reduction reactions of gaseous O_2 and Cl_2 in seawater at the cathode side during charge/discharge processes. In principle, the oxygen evolution reaction (OER) and oxygen reduction reaction (ORR) are thermodynamically preferred over the chlorine evolution (ClER) and chlorine reduction reaction (ClRR), according to the Pourbaix diagram of a water electrolyte containing Cl^- ions; however, the proportion of the two reactions depends on the operating conditions near the cathode current collector. Considering the pH of seawater (~8), Na^+ ion content in seawater (~0.47 M) and oxygen partial pressure at 100% saturation from ambient air (~0.2 atm), the half-cell and full-cell reactions during the charge/discharge processes and the theoretical cell voltage (E_{cell}) can be expressed as follows : [34]

$$\text{Anode: } Na^+ + e^- \leftrightarrow Na;\ E^o \approx -2.71\ V \quad (1)$$

$$\text{Cathode: } O_2 + 2H_2O + 4e^- \leftrightarrow 4OH^-;\ E^o \approx 0.77\ V\ vs.\ NHE\ (pH=8) \quad (2)$$

$$\text{Overall: } 4Na(s) + 2H_2O + O_2(aq) \leftrightarrow 4NaOH(aq);\ E_{cell} \approx 3.48\ V \quad (3)$$

During discharge, the Na metal anode is oxidized to Na^+ ions and transported into the seawater catholyte through the NASICON solid-electrolyte. At the same time, the ORR occurs, forming water-soluble NaOH at the cathode part. The seawater cell is charged by the reduction of Na^+ ions from seawater onto the anode in the opposite manner, while seawater oxidation (OER) occurs at the cathode side.

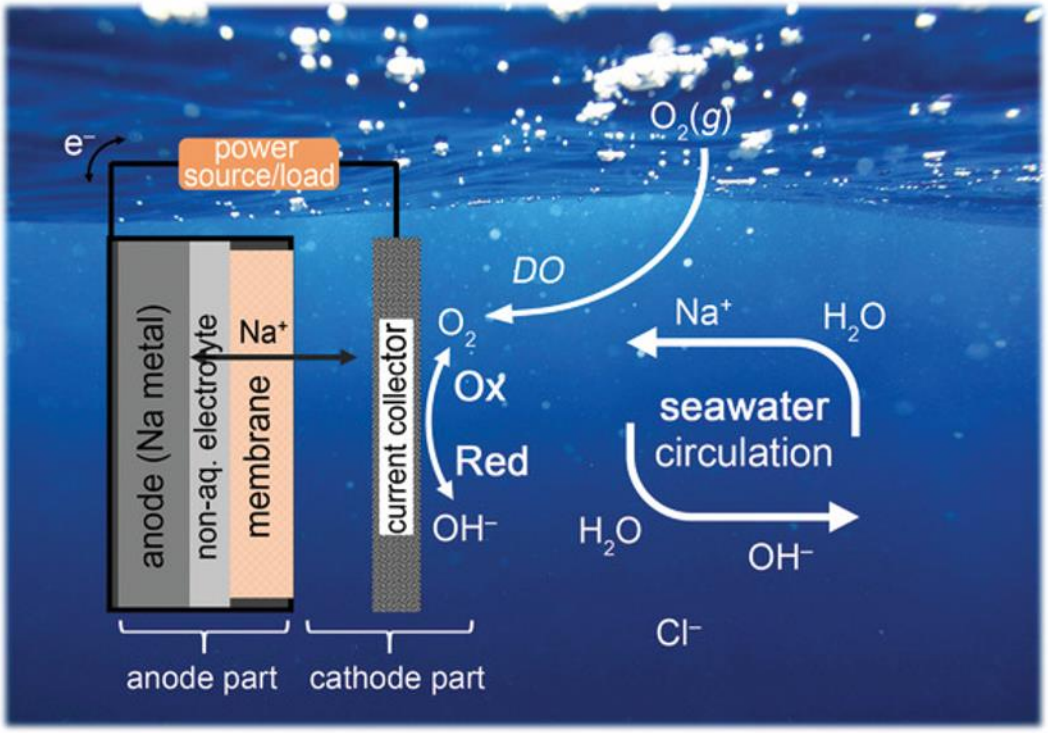

Figure 7. Schematic illustration showing basic cell structure and working mechanism of a seawater batteries upon charging and discharging.[60]

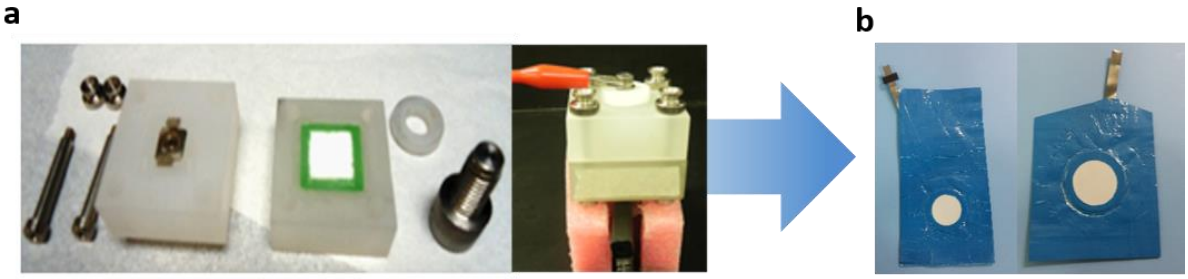

Figure 8. (a) Hand-made cell (ver.1) and (b) pouch-type cell (ver.2)

The seawater battery employs multilayer electrolytes consisting of non-aqueous (anolyte) and aqueous (seawater catholyte) electrolytes and a ceramic electrolyte (NASICON) between them. Such a structural feature of the cell requires a new type of cell platform and a testing environment other than a typical 2032 coin-type cell. Initially, the possibility of this battery system is confirmed by fabricating a hand-made cell and pouch-type cell. However, there is a problem of seawater leakage and in the case of pouch cells, cell performances are vary depending on the person who made it (Figure 8). Hence, it is essential to have the normalized cell and its standard testing condition so that the potential chemicals can be easily tested and their results can be compared.

Chapter 2 shows coin-type cell design and engineering its compartment for rechargeable seawater batteries (Figure 9). To improve the durability, solid electrolytes (NASICON membrane) are designed to be round in shape and some parts are coated with polypropylene to prevent corrosion from seawater. Furthermore, enhancing sluggish kinetic of the oxygen reduction reactions (ORR), we have designed flow-cell tester. Based on these findings, further experiments on promising materials in seawater batteries can be conducted using the customized coin-type cell.

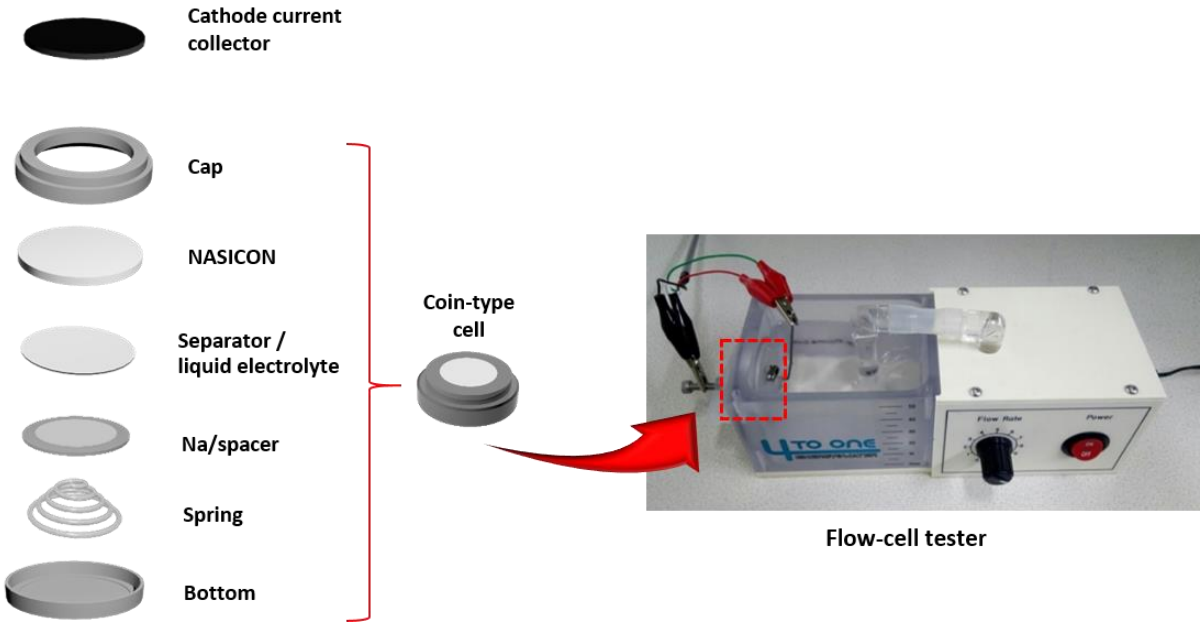

Figure 9. Components of coin-type cell and flow-cell tester

1.4 Challenges of seawater batteries

The problem of seawater batteries is the low voltage efficiency due to the sluggish kinetic of oxygen evolution reactions (OER) and oxygen reduction reactions (ORR).[40, 61] Table 1 shows the voltage efficiency of the seawater batteries. Basically, the voltage efficiency of the seawater batteries is 77.5 % by using Bare Heat-treatment carbon felt (HCF). The voltage efficiency can be improved by using electrocatalysts such as carbon-based, Pt/C and metal-oxide based materials etc. (Figure 10). It can be seen Table 1 that voltage efficiency can be improved ~90 %. However, there are several problems in using an electrocatalysts. The process of coating and drying the electrocatalysts on the surface of the carbon felt is complicated and the surface coating is not stably attached for a long period of time. Also, the price of Pt/C electrocatalyst, which has the most effect as a catalyst, is very expensive ($860/50g, Sigma aldrich). And even though it increases the voltage efficiency through the electrocatalysts, there is a fundamental limitation to using the catalyst because it is always accompanied by overpotential during charging and discharging process (OER and ORR reaction, Figure 11)[62].

Table 1. The voltage efficiency of the cells with various cathode current collectors.

Sample	Bare HCF	Vulcan-coated HCF	Pt/C-coated HCF	Porous carbon-coated HCF	CMO-coated HCF
Voltage efficiency [%]	77.5	83.2	90.0	89.1	89.9

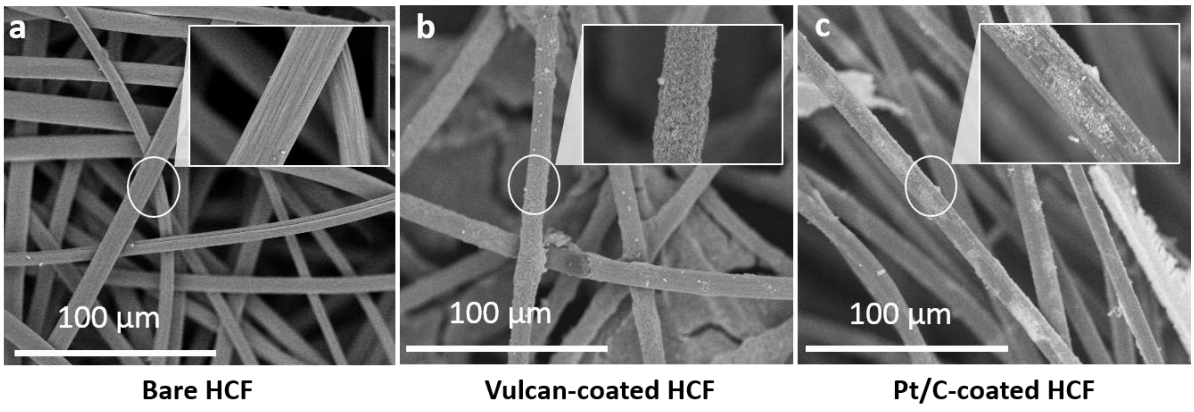

Figure 10. SEM images of (a) bare HCF, (b) vulcan-coated HCF and (c) Pt/C-coated HCF.

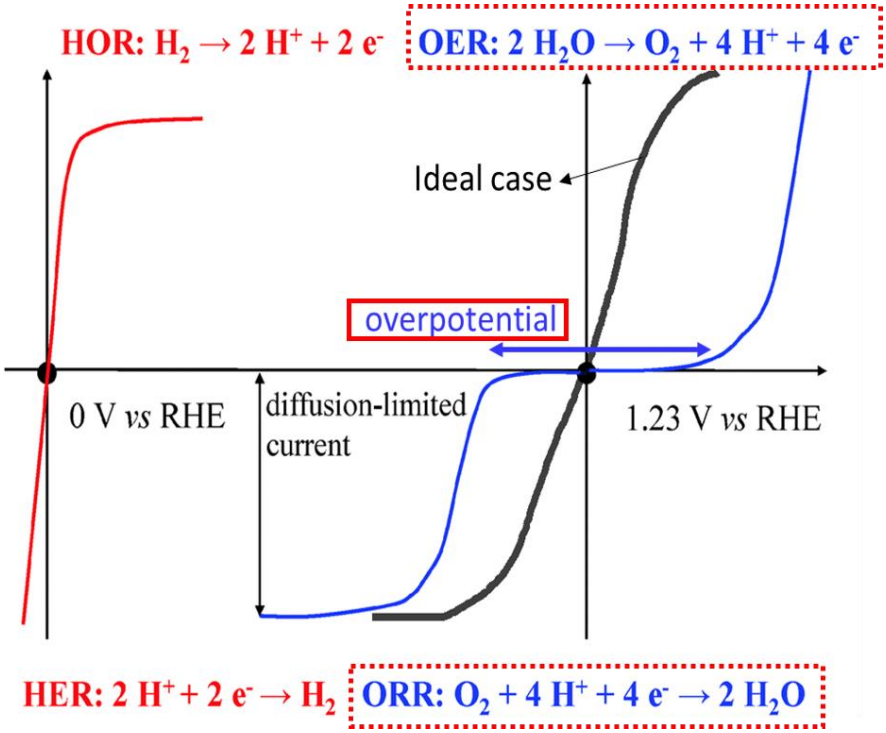

Figure 11. The polarization curves for electrochemical reactions. The blue curves refer to the oxygen-involving reactions.[62]

To overcome the low voltage efficiency of the seawater battery, we employed photoelelctrode. Photoelectrode is and electrode that, following the absorption of light, can initialize electrochemical transformation. In general, photoelectrode research is focused on hydrogen production.[63-66] In this study, we are not interested in the hydrogen production, but the electrons generated in the water oxidation using the photoelectrode are used to lower the charging voltage of the seawater battery so as to ultimately increase the voltage efficiency sharply (Figure 12, Figure 13).[67, 68] There are several requirements for using photoelectrodes in seawater batteries. In order to be applied to seawater batteries, the price should be cheap, stable in seawater condition (pH ~8), suitable band position, easy to synthesize and nonhazardous for humans and the environments. Considering these requirements, there are various photoelectrodes, but the limitations are as follows (Table 2).

So, titanium dioxide (TiO_2) photoelectrode is considered very close to an ideal semiconductor for photoelectrode because of its high stability in seawater, low cost and safety toward both humans and the environment.

Chapter 3 demonstrate an efficient photoelectrochemical-assisted rechargeable seawater battery (Figure 14). By integrating TiO_2 nanostructure-based photoelectrodes with the seawater batteries, we can achieve significant enhancement of the voltage efficiency during the charging/discharging processes. Moreover, TiO_2 nanostructures showed excellent photoelectrochemical performances in seawater in association with the efficient photocharging. Hence, the outcome of this research can provide a systematic study of potentially active materials, photoelectrodes used in solar seawater batteries and their effectiveness on the electrochemical performances.

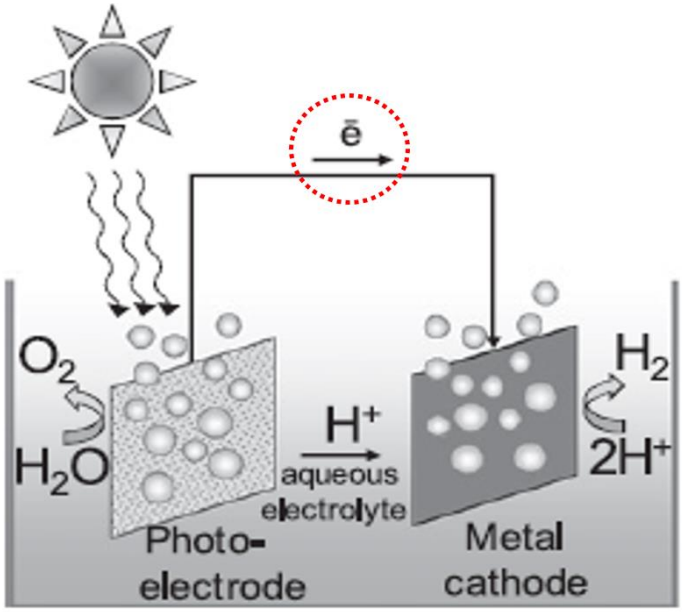

- **Photoanode :** $2hv \rightarrow 2e^- + 2h^+$
  $2h^+ + H_2O_{(liquid)} \rightarrow 1/2O_{2(gas)} + 2H^+$
- **Cathode :** $2H^+ + 2e^- \rightarrow H_{2(gas)}$

Figure 12. Schematic illustration of photoelectrochemical (PEC) water splitting. [67]

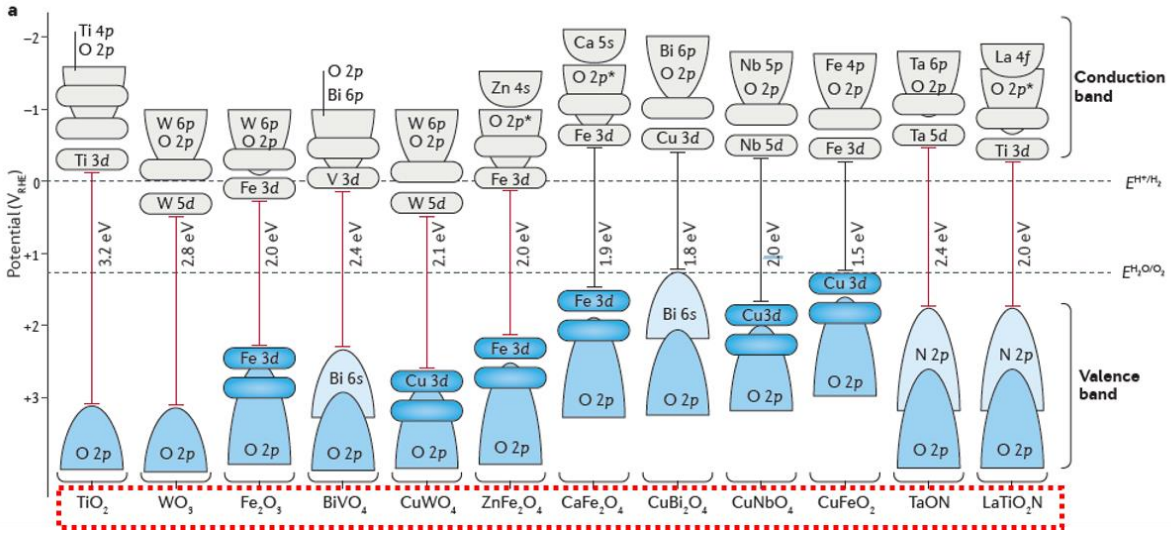

Figure 13. Various types of photoelectrodes.[68]

Table 2. Limitations of photoelectrodes for application to seawater battery

Photoelectrodes	Limitations
✓ GaAs ✓ PbS ✓ CdS	Not stable in aqueous media and toxic
✓ ZnO	Readily dissolves in water to yield $Zn(OH)_2$

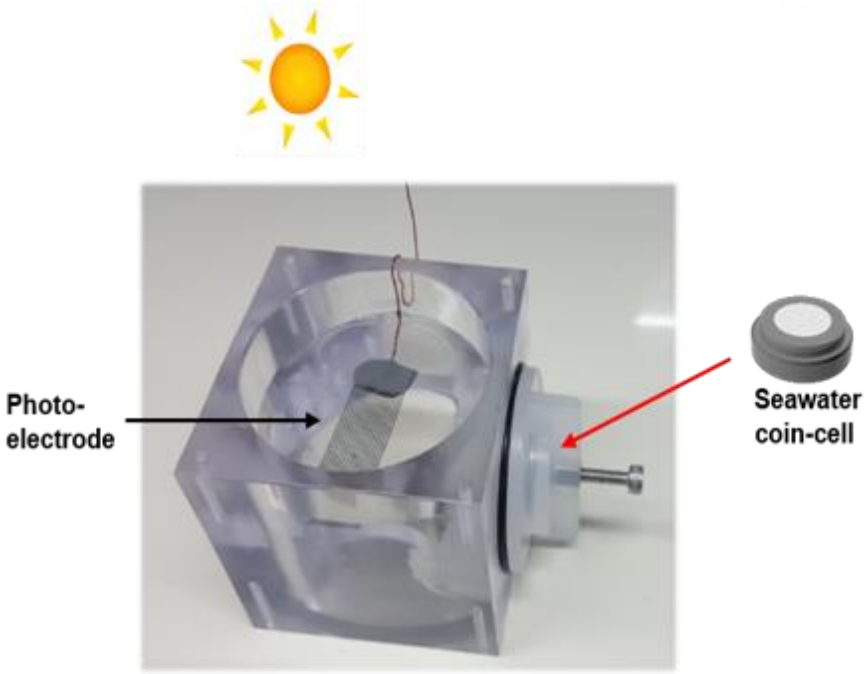

Figure 14. Digital image of solar seawater battery.

1.5 Pb-based composite anodes for sodium-ion and seawater batteries

The ever-growing demand for electrical energy storage in large scale energy storage systems (ESSs) necessitates the development of new high-performance and low-cost anode materials. Since the anode part of the seawater batteries is similar to the structure of the anode part of the SIBs, various anode materials can be applied. There are various materials as anode material candidates of the seawater batteries as shown in the following Figure 15,[69] and three kinds of materials, such as amorphous Sb_2S_3 nanoparticles, hard carbon and phosphorous/carbon composite, are applied to the seawater batteries. The amorphous Sb_2S_3 nanoparticles exhibited capacity of 470-485 mAh/g with an average discharge voltage of ~1.9 V and coulombic efficiencies of 88% during 70 cycles.[35] In the case of a hard carbon anode, it was confirmed that the cycle performance was longer than 400 cycles. The hard carbon anode showed up to 400 cycles and high reversible anode capacity (291 mAh/g at the 400th cycle), as well as good capacity retention (98.3%).[47] The phosphorus/carbon composite anode exhibited a stable cycling performance with a high reversible capacity exceeding 920 mAh/g with a coulombic efficiency of more than 92% over 80 cycles.[46]

So far, there have been several researches for seawater battery anodes, but I present Pb-based composite anode materials which is low-cost and has not been studied.

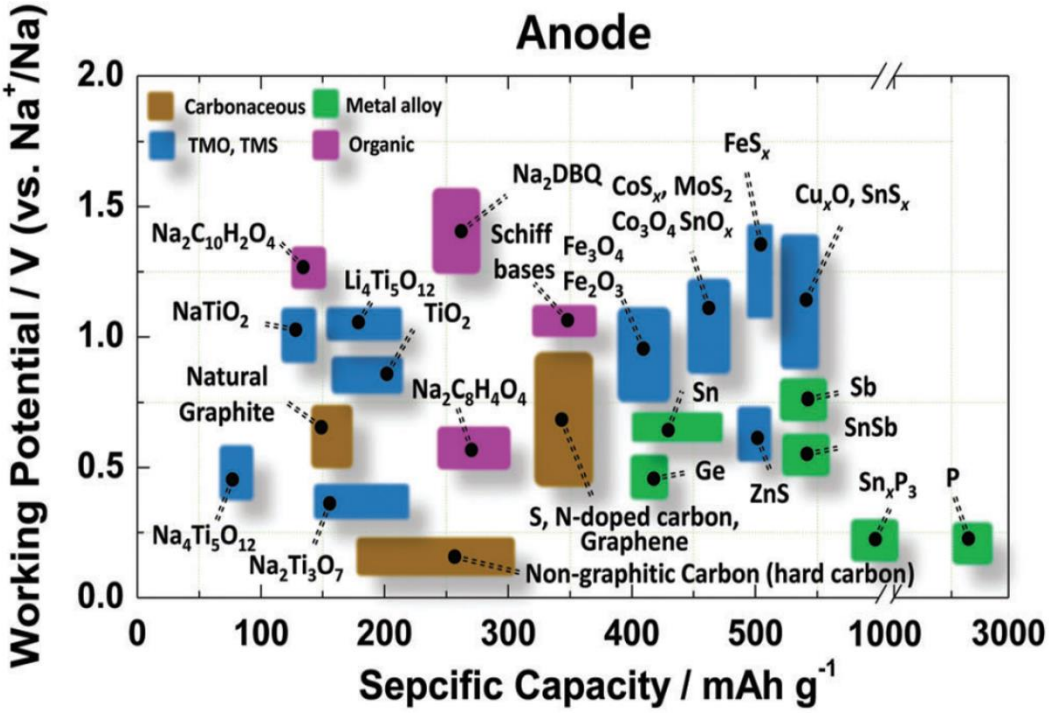

Figure 15. Various anode materials for SIBs.[69]

Little studied however are lead (Pb) and lead oxides (PbO, Pb_3O_4) that have advantages of low cost and high volumetric energy density.[70] In fact when the Argonne BatPaC model (cost calculating system, http://www.cse.anl.gov/batpac.) is used with Pb as anode for SIBs, and layered sodium transition metal oxide cathode are coupled together the energy density for a sodium-ion pouch cell design is 549 Wh/L, and the cost is projected quite low at 63.5 USD/kWh. These metrics are certainly competitive with many grid storage battery systems. However, lead toxicity is a concern. But Pb has always been one of the most recycled materials in the world, with a high recycling rate close to 99 % in the United States (Figure 16).[71] Certainly, with the rapid in-line progress of lithium- and sodium-ion battery recycling technologies, lead-based materials could become a viable contender for high-energy, low-cost anodes in the future if the performance can be improved and validated.

Chapter 4 shows Pb-based composite anode materials for sodium-ion batteries (SIBs) and seawater batteries. Lead and lead oxides have advantages of low cost and high volumetric energy density. We report Pb-O-C composite anodes synthesized by simple a high energy ball milling process. The electrochemical data tested in sodium cells show higher reversible capacity and improved cycle stability when compared to previously reported data of lead and lead oxides materials. The reaction mechanism and effect of composite structure are discussed in detail.

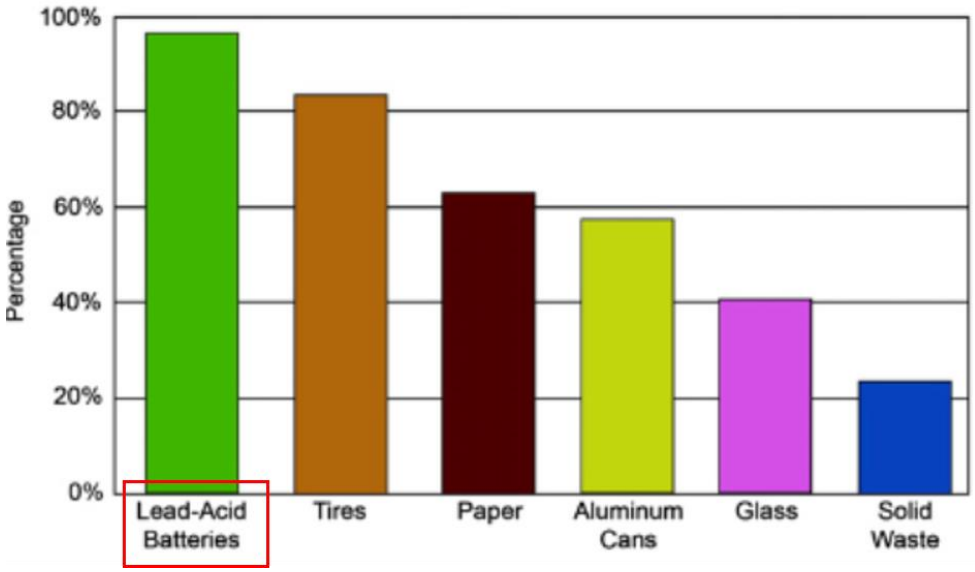

Figure 16. Recycling rate by type of waste. (99%_Lead-Acid batteries)[71]

1.2 Scope and organization of this dissertation

The objective of this dissertation is the study of cell design and engineering for solar seawater battery and its anode material development.

The chapters are categorized as follows:

Chapter 2 shows coin-type cell design and engineering its compartment for rechargeable seawater batteries.

Chapter 3 demonstrate an efficient photoelectrochemical-assisted rechargeable seawater battery. By integrating TiO_2 nanostructure-based photoelectrodes with the seawater batteries.

Chapter 4 shows Pb-based composite anode materials for sodium-ion batteries (SIBs) and seawater batteries.

Chapter 2

Development of coin-type cell and engineering of its compartments for rechargeable seawater batteries

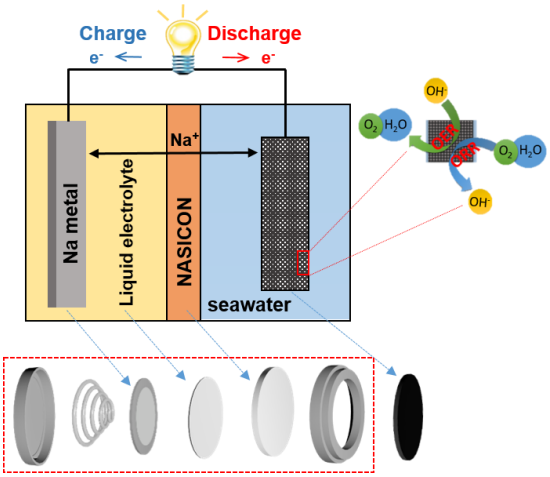

Cell design and optimization of the components, including active materials and passive components, play an important role in constructing robust, high-performance rechargeable batteries. Seawater batteries, which utilize earth-abundant and natural seawater as the active material in an open-structured cathode, require a new platform for building and testing the cells other than typical Li-ion coin-type or pouch-type cells. Herein, we present new findings based on our optimized cell. Engineering the cathode components—improving the wettability of cathode current collector and seawater catholyte flow—improves the battery performance (voltage efficiency). Optimizing the cell component and design is the key to identifying the electrochemical processes and reactions of active materials. Hence, the outcome of this research can provide a systematic study of potentially active materials used in seawater batteries and their effectiveness on the electrochemical performance.

This chapter has been published.

Reproduced with permission from J. Han, S. Hwang, W. GO, S.T. Senthilkumar, D. Jeon and Y. Kim, "Development of coin-type cell and engineering of its compartment for rechargeable seawater batteries", *Journal of Power Sources*, **2018**, 374, 24-30.

2.1 Introduction

Excessive emissions of CO_2 from the combustion of fossil fuels are the main causes of climate change and environmental pollution, which are the global issues to be solved for a sustainable society. These issues require the development of new types of systems and technologies for energy conversion and storage based on renewable energy [1, 72]. The increasing demand for the efficient utilization of renewable energy has led to the development of various types of energy storage systems (ESSs) [11, 73]. The main purpose of ESSs is to store renewable energy and use it with high energy efficiency on demand. Currently, lithium-ion batteries (LIBs) technology is a mature battery technology that holds a major position in the ESS market because of their high energy density (~300 Wh kg^{-1}), long cyclability (≥2,000 times), and competitive energy cost (250–400 \$ kWh^{-1}) [11, 28, 74]. However, their long-term sustainable use may be limited because of the steeply rising prices of Li-containing raw materials due to the increasing demand for LIBs in electric vehicles and large-scale ESSs and due to their finite geographical distribution [16].

Our group has recently introduced a novel, low-cost, and eco-friendly rechargeable seawater battery using earth-abundant, natural seawater as the active material [34, 36, 75-80]. Figure 17 illustrates the schematic of the basic structure and the components of a seawater battery cell. The cell consists of two compartments, an anode and a cathode, which are separated by a NASICON ceramic electrolyte ($Na_3Zr_2Si_2PO_{12}$). The anode compartment is composed of a sodium metal anode attached to a current collector and a non-aqueous liquid electrolyte. The cathode part consists of a cathode current collector and seawater catholyte. Utilizing seawater that contains Na^+ and Cl^- ions, the batteries operate based on the redox reactions of Na^+ ions at the anode side and the simultaneous evolution/reduction reactions of gaseous O_2 and Cl_2 in seawater at the cathode side during charge and discharge processes. In principle, the oxygen evolution/reduction reaction (OER/ORR) is thermodynamically preferred over the chlorine evolution/reduction reaction (ClER/ClRR), according to the Pourbaix diagram (Figure 20) of a water electrolyte containing Cl^- ions; however, the proportion of the two reactions depends on the operating conditions near the cathode current collector. Considering the pH of seawater (~8), Na^+ ion content in seawater (~0.47 M) and oxygen partial pressure at 100% saturation from ambient air (~0.2 atm), the half-cell and full-cell reactions during the charge/discharge processes and the theoretical cell voltage (E_{cell}) can be described as follows [34]:

$$\text{Anode: } Na^+ + e^- \leftrightarrow Na;\ E^o \approx -2.71\ V \quad (1)$$

$$\text{Cathode: } O_2 + 2H_2O + 4e^- \leftrightarrow 4OH^-;\ E^o \approx 0.77\ V\ vs.\ NHE\ (pH=8) \quad (2)$$

$$\text{Overall: } 4Na(s) + 2H_2O + O_2(aq) \leftrightarrow 4NaOH(aq);\ E_{cell} \approx 3.48\ V \quad (3)$$

During discharge, the Na metal anode is oxidized to Na^+ ions and transported into the seawater catholyte through the NASICON membrane. At the same time, the ORR occurs, forming water-soluble NaOH at the cathode side. The cell is charged by the reduction of Na^+ ions from seawater onto the anode in the opposite manner, while seawater oxidation (OER) occurs at the cathode side.

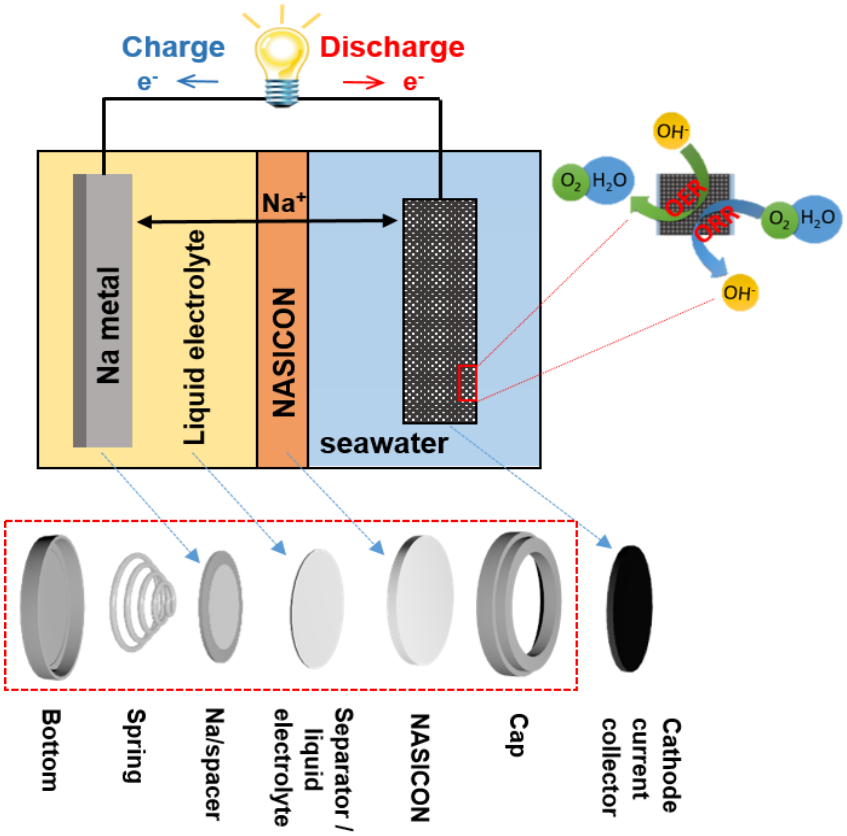

Figure 17. Schematic diagram of the seawater battery (top) and disintegrated cell components of the coin-type cell (bottom)

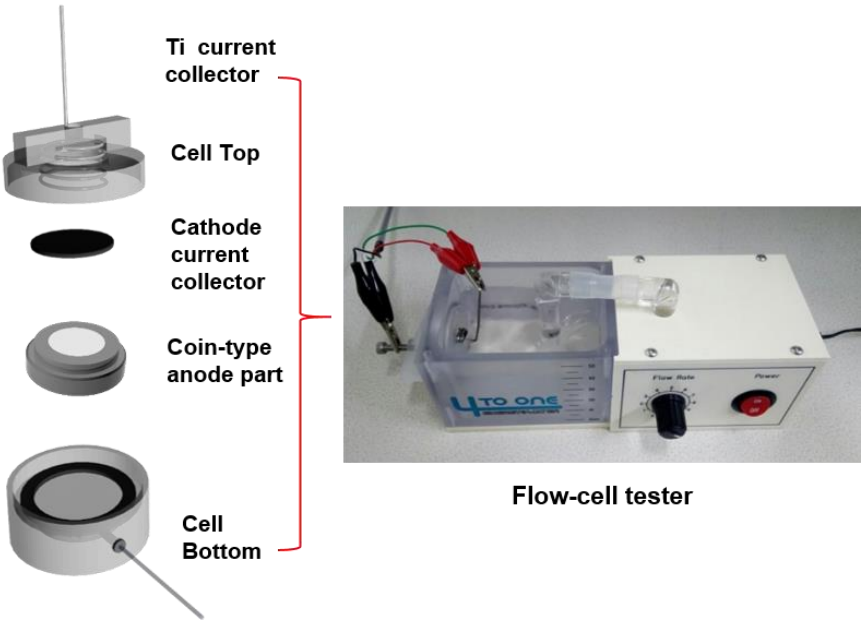

Figure 18. Assembled coin-type cell and flow-cell tester.

The coin-type anode part is designed by taking into consideration the essential cell components of the seawater batteries (Figure 17). The coin-type anode part and cathode current collector (Heat-treatment carbon felt) are loaded to coin-cell jig and tested using flow-cell tester. The cathode part should be in direct contact with seawater and the anode part should be completely sealed. So a coin-cell jig is needed. To prevent corrosion in seawater, the current collector of titanium current collector is used and all components are designed with polypropylene material. In the case of the flow-cell tester, the motor runs continuously and circulates the seawater constantly (Figure 18).

The seawater battery system employs multilayer electrolytes consisting of non-aqueous (anolyte) and aqueous (seawater catholyte) electrolytes and a ceramic electrolyte (NASICON) between them. Such a structural feature of the cell requires a new type of cell platform and a testing environment other than a typical 2032 coin-type cell. Previously, we have reported a comparative study between sodium, beta-alumina (Na, β"-Al_2O_3), and $Na_3Zr_2Si_2PO_{12}$ as the Na^+ ion conducting solid electrolyte for seawater batteries [37]. We also investigated non-aqueous electrolytes at the anode side such as ether-based or ionic liquid electrolytes [43, 76], as well as negative electrodes to replace the Na metal, and hence to achieve Na metal-free seawater batteries [36, 76, 79]. It was found that the cell design, the choice of the component material, and its engineering could affect the cell performance of the materials being investigated as potential electrodes and electrolytes. Hence, it is essential to have the normalized cell and its standard testing condition so that the potential chemicals can be easily tested and their results can be compared to those obtained in the other labs. This will greatly contribute to the further development of seawater batteries by providing many choices of key materials. For example, the great success of the Li-ion battery technology also started with developing a coin-type cell design that allowed researchers to investigate and discover its key electrode and electrolyte materials.

In this work, we show the importance of cell components in seawater batteries and the optimized cell performance by engineering them and highlighting the significance of the cell design and component engineering. The effect of wettability of the cathode current collector was investigated. As a low-cost, highly conductive cathode current collector, a commercially available carbon fiber felt was selected and the surface wettability was examined to improve the charge-discharge behaviors. In addition, the flow effect of the seawater catholyte was studied by conducting a comparison test of flow ON/OFF states. Furthermore, we proved the sluggish kinetics of the OER/ORR on the cathode current collector in seawater, which induces major kinetic limitations during the charge and discharge processes of seawater batteries, by comparing a seawater cell with a fast Na-ion-intercalating electrode material. To improve the cathode reaction kinetics, we employed several electrocatalysts facilitating the OER/ORR, highlighting significance of the role of the cathode current collector in achieving low-cost, high-performance seawater batteries.

Figure 19. Digital images of the flow cell tester used in this work.

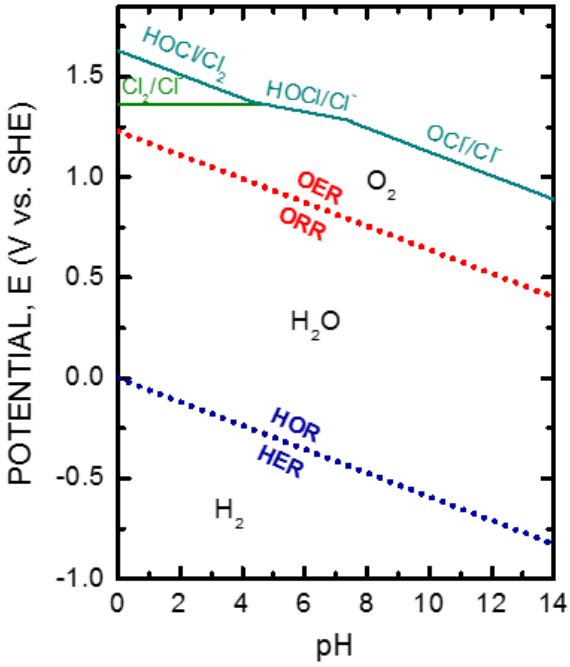

Figure 20. Pourbaix diagram showing the redox reaction potentials of H_2, H_2O, O_2, and Cl^-.

OER: $\boldsymbol{4OH^- \rightarrow O_2 + 2H_2O + 4e^-;\ E^o \approx 0.75\ V\ vs.\ NHE}$ **(pH=8)**

ClER: $2Cl^- \rightarrow Cl_2 + 2e^-;\ E^o \approx 1.36\ V\ vs.\ NHE$

The OER and ClER could be competitive at the cathode side (in seawater) during charging of seawater batteries

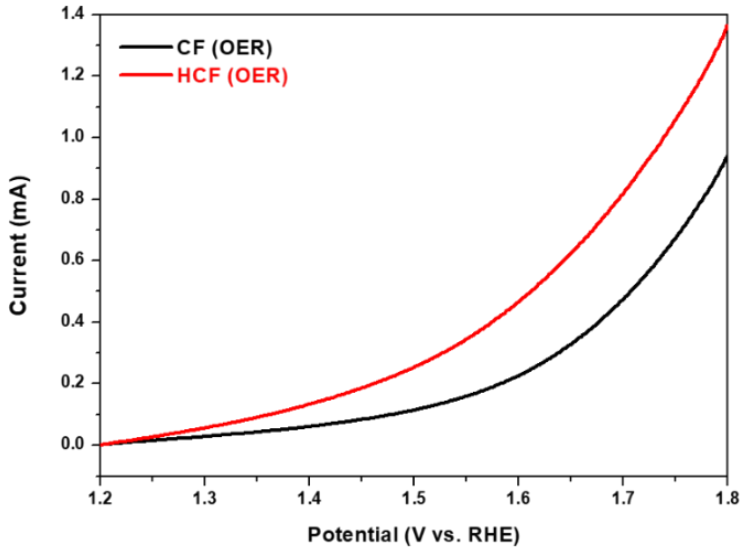

Figure 21. Anodic polarization curves of the CF and HCF measured in N_2-saturated seawater. All the polarization data were recorded at a scan rate of 5 mV s-1 and a rotating speed of 1200 rpm.

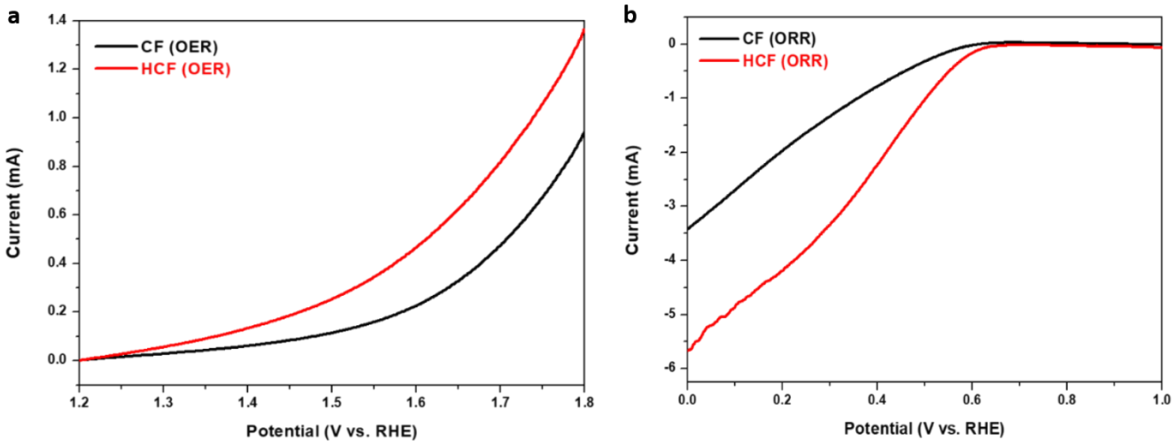

Figure 22. Comparison between the CF and HCF. Anodic polarization curves for the OER measured in N_2-saturated seawater (a) and cathodic polarization curves (b) for the ORR in O_2-saturated seawater. All the polarization data were recorded at a scan rate of 5 mV s- and a rotating speed of 1200 rpm.

2.2 Experimental detail

2.2.1 Preparation of solid electrolyte

NASICON ($Na_3Zr_2Si_2PO_{12}$) was used as a solid electrolyte to separate the seawater cathode from the anode. The NASICON was fabricated by a solid-state reaction based on our previous study [38, 75, 76]. Briefly, the precursor powders of $Na_3PO_4 \cdot 12H_2O$, SiO_2, and ZrO_2 (Aldrich) were uniformly mixed using a mechanical ball mill and calcined at 400 °C and 1,100 °C in ambient air. The calcined powder was ground and uniaxially pressed into pellets at 7 MPa. The pellets were sintered at 1,230 °C for 10 h in ambient air. The diameter and thickness of final NASICON membranes were 16 mm and 1.0 mm, respectively, and the measured density was around 3.07 g cm^{-3} (~94% of the theoretical value).

2.2.2 Assembly of coin-type anode compartment

The seawater coin-cells were assembled by the following procedure. For the anode compartment, the solid electrolyte (NASICON membrane) was attached to the open and round upper cap (anode top part) made of polypropylene. Na metal (99.9%, Sigma Aldrich) was attached to the surface of a round stainless steel spacer and the non-aqueous electrolyte (~20 μl) was injected. Polyethylene separators with a thickness of 16 μm and a diameter of 19 mm (Celgard) were inserted between the Na metal and NASICON and then the upper cap and anode bottom part were sealed by using an epoxy glue (J-B Weld 8280), which was dried for 24 h in ambient air. A 1.0 M $NaCF_3SO_3$ (Sigma Aldrich) salt was dissolved in tetraethylene glycol dimethylether (Sigma Aldrich) and stirred for 4 h in Ar atmosphere, which was used as a non-aqueous electrolyte. The coin-cell assembly was performed in a glove box under a high-purity Ar atmosphere (oxygen and water < 1.0 ppm).

2.2.3 Preparation of cathode current collector and coating of electrocatalysts

Carbon felts (XP-30A, Toyobo Co., Ltd) were used as the cathode current collector for seawater batteries. The thickness and electrical resistance was around 4.3 mm and 0.15-0.20 Ω cm^2, respectively. Prior to the use, carbon felts with a diameter of 16 mm were heat-treated to improve the hydrophilicity of the surface at 500 °C (at a ramping rate of 2 °C min^{-1}) for 2 h in ambient air. Electrocatalysts were employed to improve the reaction kinetics during charge and discharge. In this work, we used four types of electrocatalyst powders, Pt/C (20 wt%, Alfa Aesar), Vulcan XC-72R (fuel cell store), cobalt manganese oxide (CMO), and porous carbon. CMO nanocubes were synthesized by the heat treatment of $Mn_3[Co(CN)_6]_2 \cdot nH_2O$ in ambient air. The $Mn_3[Co(CN)_6]_2 \cdot nH_2O$ precursors were prepared by the co-

precipitation method and accompanied by the changes in the chemical composition. In the case of porous carbon, the grapefruit shell was dried at 100 °C and carbonized at 800 °C. The detailed fabrication process of the CMO and porous carbon particles can be found in previous reports [34, 78]. Nickel hexacyanoferrate (NiHCF) cathode current collector particles were synthesized by a one-step co-precipitation reaction. First, $Ni(NO_3)_2 \cdot 6H_2O$ was dissolved in deionized (DI) water (solution A); then, NaFe(CN)6 was dissolved in DI water (solution B). Solution A was dropped onto solution B using a syringe and two solutions were mixed. Finally, the mixture was dried in a convection oven at 80 °C [77].

The catalyst slurries and NiHCF nanoparticles were prepared by mixing the nanoparticles, conducting agent (Super-P, TIMCAL), and poly (vinylidene fluoride) (PVDF, Sigma Aldrich) binder with a weight ratio of 80:10:10 in N-methyl-2-pyrrolidone (NMP, Sigma Aldrich) with a THINKY MIXER (AR-100). As-prepared catalyst slurries were uniformly coated on heated carbon felts (HCF) and then dried in a convection oven at 80 °C. The loading amount of each catalyst was 4 mg cm^{-2}.

A flow-cell tester was prepared to test the seawater coin-cell; the cathode part was in contact with the seawater and the anode part was blocked by seawater. Polycarbonate was used as the flow-cell tester material to prevent corrosion in seawater. A 16-mm carbon felt air-electrode material was used as a current collector and titanium spring as a cathode conducting wire.

The method of assembling the coin cell into the flow-cell tester is as follows. First, the assembled coin cell was placed between the cell top and bottom and then assembled by turning. Second, the coin-cell anode compartment was combined with the seawater container, which is filled with 200 ml of seawater. Using this flow-cell tester, we studied various factors affecting the electrochemical performance of coin-type seawater batteries.

2.2.4 Electrochemical tests

A flow-cell tester (4TOONE Energy Co., Ltd) was used in these experiments. Galvanostatic charge-discharge measurements were conducted for all the batteries using a Wonatech (WBCS 3000) electrochemical instrument. Natural seawater from Ilsan beach, Ulsan, Republic of Korea (GPS 35.497005, 129.430996) was used after filtration and the ionic species and relative concentrations can be found elsewhere (Table *3*). Most of the first charge and discharge characteristics of the cells were tested at 0.025 $mAcm^{-2}$ for 5 h or 10 h; other charge and discharge curves of the cells were measured at various current densities ranging from 0.005 to 0.05 $mAcm^{-2}$. All the electrochemical measurements were performed at room temperature.

2.2.5 Characterizations

The wettability (hydrophilicity) of the carbon felt surface was examined using a contact angle meter (Phoenix 300, SEO Company). The oxygen content in seawater during battery discharging was monitored using a dissolved oxygen (DO) meter (ORION STAR A216, Thermo Fisher). The DO meter probe was set at ~1 cm from the surface of the cathode current collector. The chemical bonding states of the carbon felt surface were analyzed by X-ray photoelectron spectroscopy (XPS, Thermo Fisher) with an Mg Kα X-ray source. The specific surface area was estimated by N_2 adsorption-desorption isotherms at 77 K (BELSORP-max) and the Brunauer-Emmet-Teller (BET) method. The surface morphology was observed by scanning electron microscopy (SEM, FEI Verios 460).

2.3 Results and discussion

2.3.1 Design of coin-type cell

The basic structure and components of a seawater battery cell are schematically depicted in the bottom portion of Figure 17. A photograph of a coin-type cell assembled into a flow-cell tester is shown in Figure 18. The key point of the cell is to completely separate the highly reactive Na metal anode part from the seawater catholyte, with only the NASICON exposed for the selective transport of Na^+ ions between the two compartments. The NASICON ceramic was designed to be round in shape with a diameter of 16 mm for better processability and durability. Based on the size and shape of the NASICON ceramic, the upper cap and lower bottom were designed and made of stainless steel (Figure 23). The whole part of the upper cap was coated with polypropylene to prevent direct electronic contact with the bottom and to protect the stainless steel cap from rust when exposed to corrosive seawater (Figure 24). The NASICON ceramic was then sealed with the upper cap using an epoxy glue. The epoxy should be carefully selected to be stable with both seawater and the non-aqueous electrolyte. After loading the active material and cell compartments (spring and spacer) in the bottom part, the NASICON upper cap was placed on the bottom part and sealed by the specially designed sealing machine (Figure 25). The assembled coin-type anode part, highlighted by a red dotted box (Figure 17), was combined with cathode current collector and then loaded into a cell tester for electrochemical testing, where the seawater catholyte can be circulated in ambient air through a simple pumping apparatus (Figure 18, Figure 26).

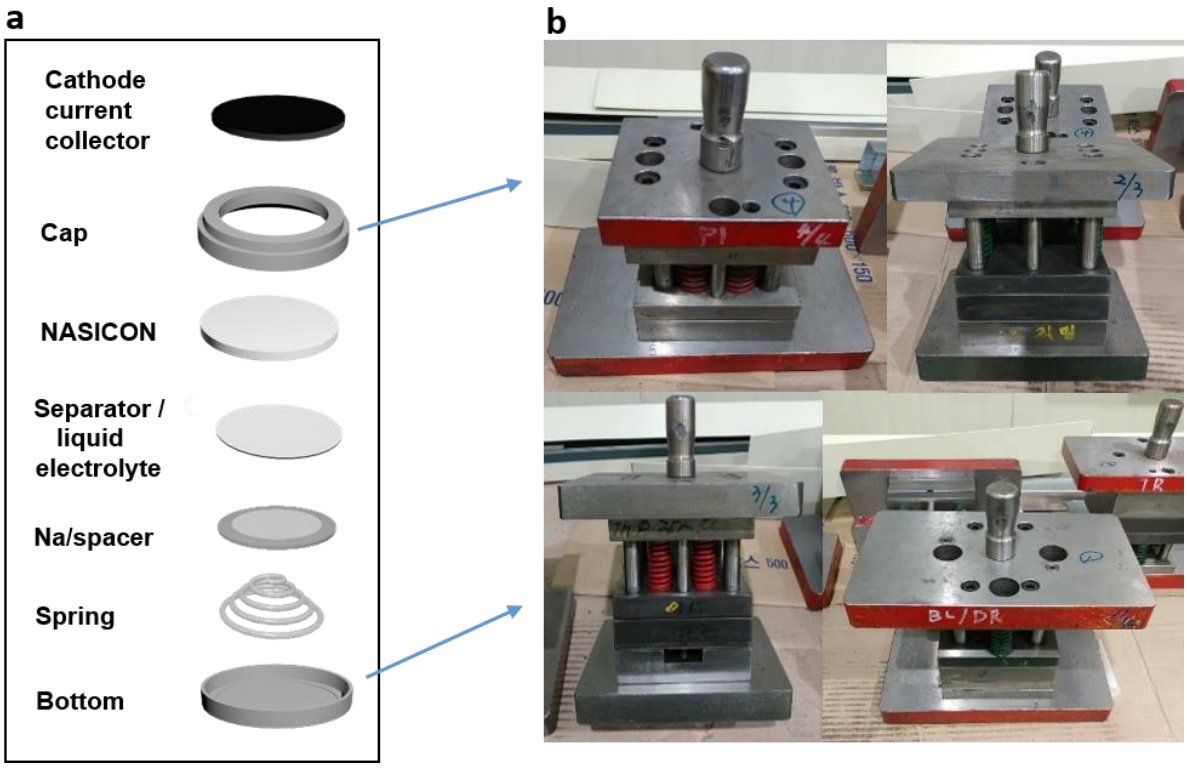

Figure 23. (a) Cell components of seawater battery. (b) Various molds for making seawater coin cell parts.

Figure 23 (a) shows that seawater battery coin-cell parts designed by considering the core components of a seawater cell. The 2032 coin cell parts in a lithium ion battery cannot be used as a seawater battery cell parts because cathode part of seawater battery must be contacted with seawater directly. So, cap and bottom were made for only seawater battery by using various kinds of molds.

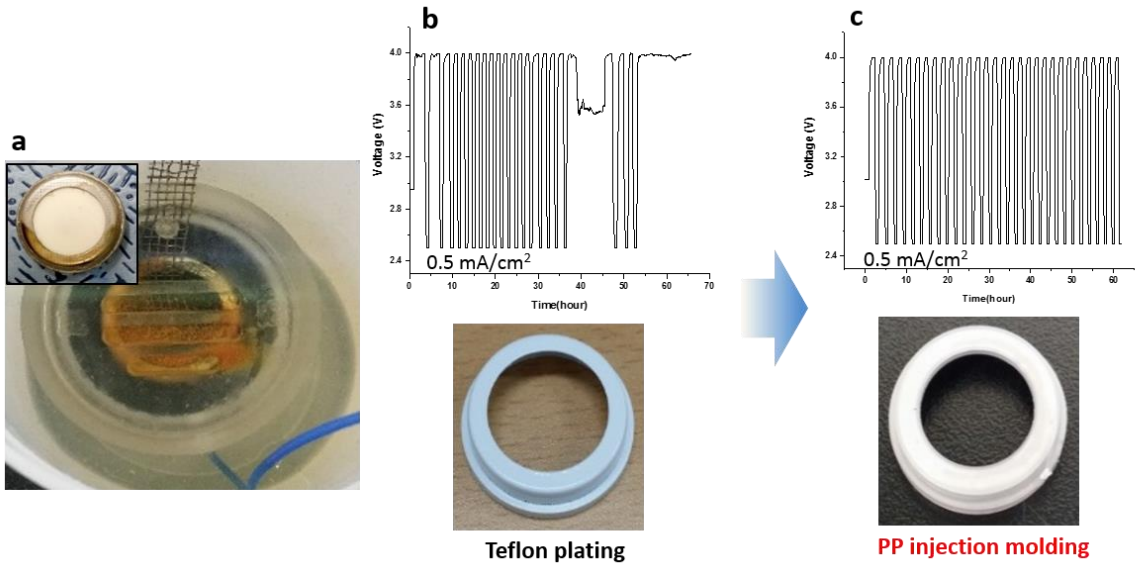

Figure 24. The problem of seawater corrosion. (a) Rusted stainless steel seawater coin-cell. (b) Teflon coated seawater coin-cell cap. (c) Polypropylene seawater coin-cell cap through injection molding method.

Figure 24 (a) shows that corrosion problems have occurred in seawater due to the use of stainless steel which is used as a lithium ion battery coin-cell parts. In order to solve the corrosion problem, the surface of the cap was coated with teflon. When tested at a current rate of 0.5 mA/cm^2, it was confirmed that charge/discharge was working at first time, but discharge did not proceed after ~40 hours.

However, the cap that was in the polypropylene injection molding had no problem of charge/discharge process, and showed good cycle stability. So we decided to use the PP injection cap as cell parts through various trial and error.

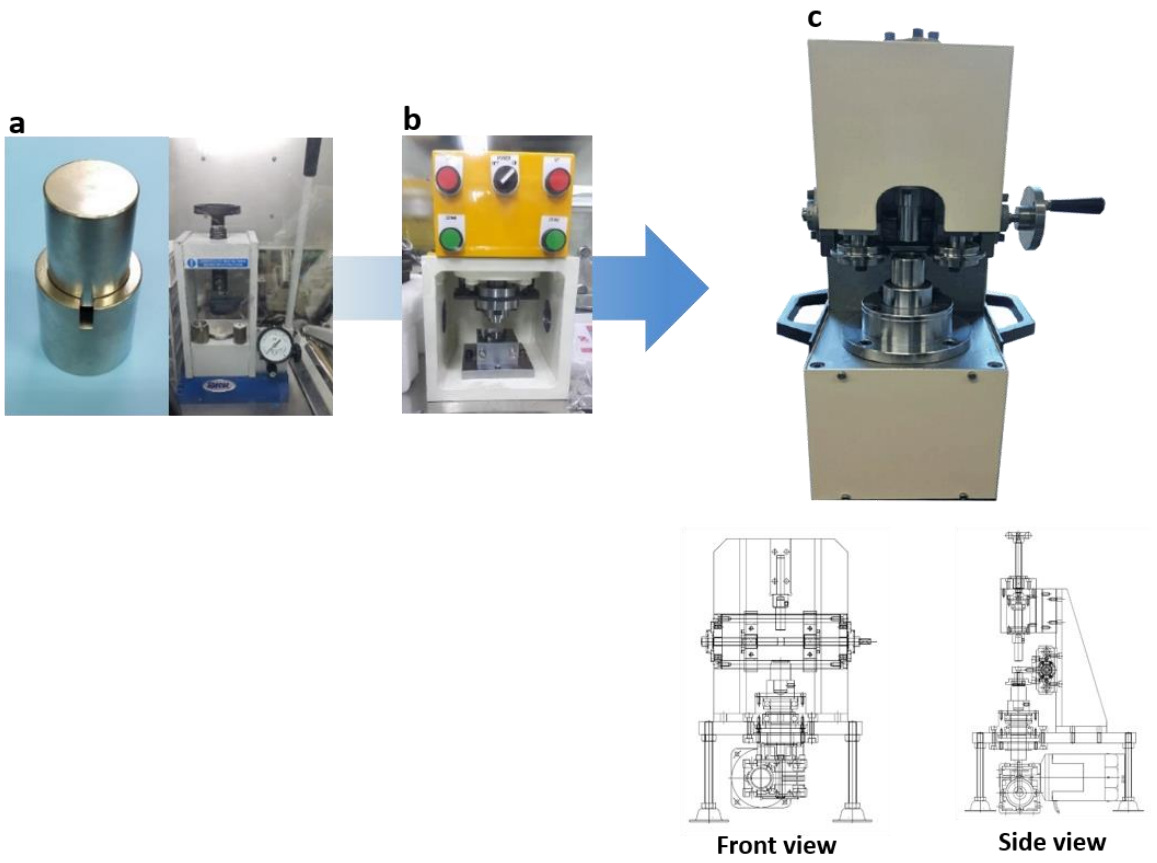

Figure 25. Three types of seawater coin-cell crimper. (a) Ver.1; mold and manual press type. (b) Ver.2; up and down auto press machine. (c) Ver.3; side roller method of auto crimper.

At first, the seawater coin-cell was assembled using crimper of mold and manual press type (Figure 25 (a)). To assemble coin-cell convenient, up and down auto press machine was designed (Figure 25 (b)). However, unlike conventional batteries, seawater battery use a solid electrolyte as a core component so ceramic broken problem occurred during assembly. To solve this problem, a side roller auto crimper was designed (Figure 25 (c)). The pressure was applied on the side, which completely solved the ceramic broken problem.

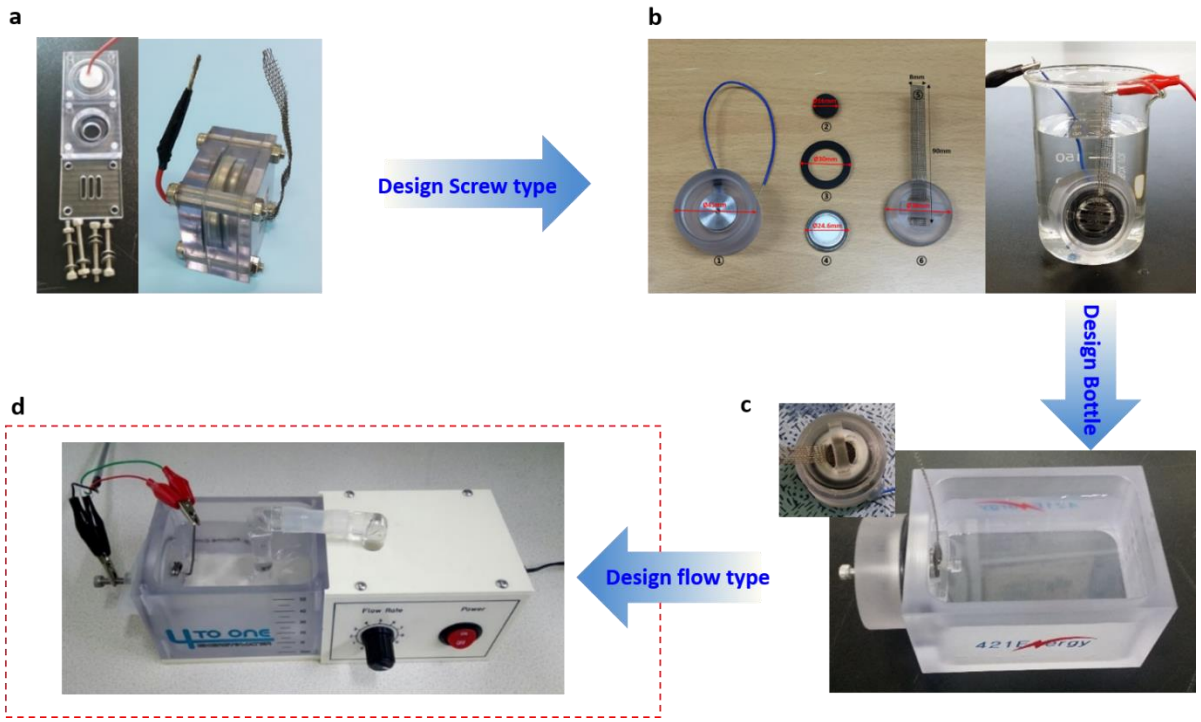

Figure 26. Development of flow type tester. (a) Ver.1; bolt and nut type Jig. (b) Ver.2; screw type Jig. (c) Ver.3; static type tester. (d) Ver.4; Flow type tester.

Figure 26 (a) shows that first version of tester for seawater batteries. At first time, we made a tester using bolts and nuts, but there was a seawater leakage. To prevent seawater leakage problem, screw type Jig was developed (Fig. (b)). But there was no container and it was difficult to control the seawater volume. Static type tester was fabricated to control seawater volume (Fig. (c)). Finally, flow type tester was designed utilizing seawater flow mode (Fig. (d)).

2.3.2 Cathode current collector and its requirements

The cathode current collector is required to have good electronic conductivity, good chemical and electrochemical stability, a large surface area (more active sites), and cost-competitiveness to be used in the seawater cell described in Section 2.3.1. Among several candidates, a commercially available carbon felt was selected and tested in this work because it meets those requirements and has been extensively used in fuel cells and redox flow batteries [81, 82]. However, the surface of carbon felts is typically hydrophobic due to the presence of sizing agents for mechanical reinforcement; thus, aqueous electrolytes, including seawater, are not wetted well on pristine carbon felts. We performed heat treatment of carbon felts at 500 °C in ambient air [81] and analyzed the surface wettability by measuring their contact angles before and after the heat treatment. Figure 27 (a) shows the contact angles of a seawater droplet on the pristine carbon felt (PCF) and HCF. The PCF did not allow complete wetting even after 5 min; the contact angle was measured as 135°. On the other hand, the HCF allowed the penetration of the water droplet within 1 s. Thus, the contact angle could not be measured, indicating that the air-heating process makes the surface of the carbon felts hydrophilic. We compared the electrochemical performance of PCF and HCF as cathode current collectors for seawater batteries. Figure 27. (b) exhibits the initial charge-discharge voltage curves of seawater cells using the PCF and HCF air-electrodes at a current rate of 0.025 mA cm^{-2} for 5 h at each step (OFF state). The PCF cell showed the charge and discharge voltages of 4.1 V and 2.5 V, respectively, resulting in a large voltage gap between the charge and discharge curves (ΔV) of ~1.6 V. On the contrary, the cell using HCF showed a relatively low ΔV of ~1.4 V. This result indicates that the improvement in the surface wettability of cathode current collector (here, carbon felts) enhances the reaction kinetics during charge/discharge processes by reducing ΔV. We performed XPS and N_2 sorption isotherm measurements to analyze the changes in the surface chemistry and the area of carbon felts by heat treatment. The heat treatment in air resulted in an increase in the C–O bond-to-C=O bond ratio and in the specific surface area of carbon (Figure 27. (c) and (d)). For the O 1s spectra, the surface of HCF had a large ratio of the C–O bond (phenolic, at 533 eV)-to-C=O bond (carbonyl, at 531 eV), compared to that of the PCF surface [83-85]. The specific surface area (S_{BET}) increased from ~0.62 m^2/g to ~2.23 m^2/g by about 3.6 times after the heat treatment (the inset in Figure 27. (c) and (d)). Therefore, the increased surface area and changes in the functional groups on the surface, as a result of the air-heating process, were responsible for the improved surface wettability and the reduced ΔV, which could improve the energy efficiency of seawater batteries.

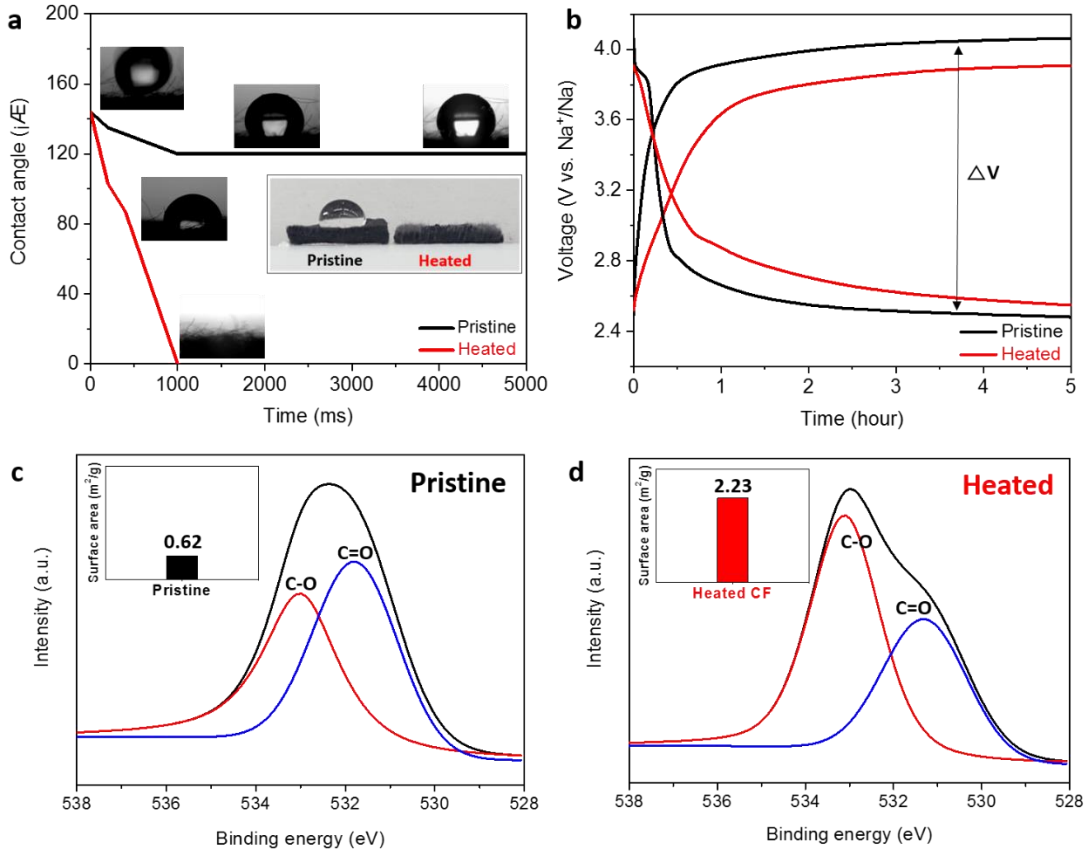

Figure 27. (a) Comparison of the contact angle of water on the pristine carbon felt (PCF) and heated carbon felt (HCF) and their photographs (inset), (b) galvanostatic charge-discharge voltage profiles of the cells using PCF and HCF, measured at 0.025 mA cm^{-2} for 5 h at each step, and (c, d) XPS O 1s spectra of PCF and HCF. The insets in Figure 27 (c) and (d) show S_{BET}.

Table 3. Ionic species in natural seawater, detected by ion chromatography

Components	Na^{2+}	Cl^{-}	SO_4^{2-}	Mg^{2+}	Ca^{2+}	K^{+}	**Total**
Concentration (mg/kg)	10,188	19,543	2,754	1,266	406	385	34,541

In this work, we used natural seawater from Ilsan beach, Ulsan, Republic of Korea (GPS 35.497005, 129.430996) after simple filtration. The cations and anions in the seawater were analyzed by ion chromatography and the result is shown above (Table 3).

2.3.3 Flow effect of seawater catholyte

For seawater batteries using natural seawater as the catholyte, it is important to continuously supply fresh reactants (water and oxygen) to the reaction sites (on the cathode current collector) to replace the reacted products (hydroxide ions) during cell operation. We examined the flow effect of the seawater catholyte on the cell performance by comparing the flow ON and OFF states. Figure 28 (a) presents the charge-discharge voltage profiles of the cell under the OFF and ON states at 0.025 mA/cm^2 for 5 h at each step. Under the OFF state, the cell showed slow saturation of the charge and discharge voltage; the charge and discharge terminal voltages were ~3.9 V and ~2.8 V, respectively, resulting in a large ΔV of 1.1 V. On the other hand, the seawater flow (ON state) clearly reduced ΔV (0.7 V); the charge and discharge voltages were ~3.7 V and ~3.0 V, respectively. It should be noted that the seawater flow was more effective in reducing the overpotential occurred during the discharging process compared to the charging process (Figure 29). We monitored the DO content in the seawater catholyte during discharging at a current rate of 0.1 mA cm^{-2} with and without the flow (Figure 28 (b)). The discharge voltage was initially ~2.8 V and was almost retained as the discharge process proceeded under the ON state, while the DO content decreased steadily from ~9.2 mg L^{-1} to ~8.2 mg L^{-1}. This reveals that the discharge process consumes the DO, due to ORR, as described above. Right after the flow is turned OFF, both the voltage and the DO content decreased to ~1.9 V and ~ 5.9 mg L^{-1}, respectively. However, after the turn-ON, the voltage and DO content recovered almost the same state as before the turn-OFF.

An additional experiment was conducted to check the voltage change during charge and discharge processes at a current rate of 0.025 mA cm^{-2} under the ON and OFF states (Figure 28 (c)). When the cell operates at the ON state, ΔV was ~0.7 V; when the cell was cycled at the OFF state, ΔV increased to ~1.1 V, then, decreased back to ~0.7 V after the system was restored to the ON state. These results confirm that the flow mode circulating the seawater catholyte allows the reactants to be continuously supplied to the active sites on the cathode current collector. In particular, ambient O_2 gas is continuously dissolved in seawater with the help of the artificial flow, providing sufficient amounts of the reactant (DO) toward the immersed cathode current collector during the discharging period. Consequently, this process mitigates the concentration polarization at the cathode side, reducing the overpotential arising from the OER/ORR during cell operation [86, 87]. Hereafter, all cell tests were carried out at the flow ON state.

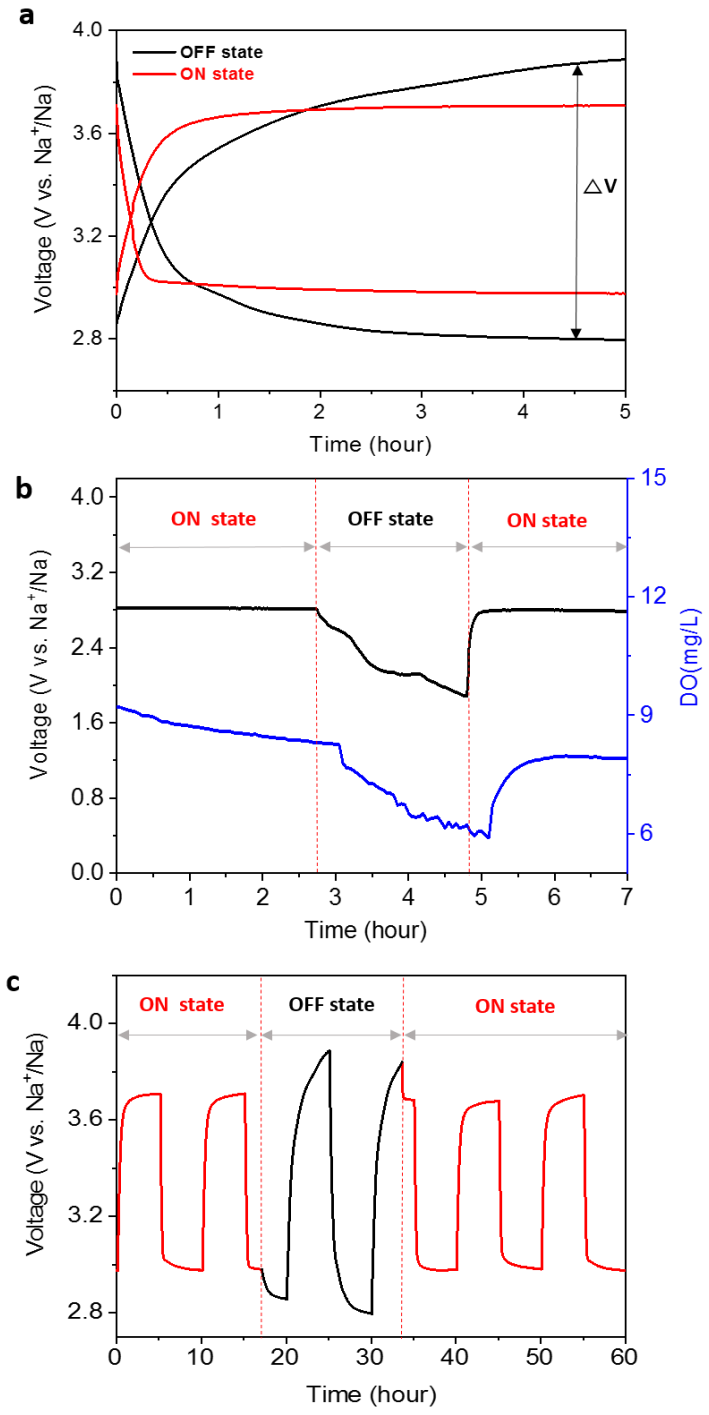

Figure 28. (a) Charge-discharge voltage profiles of the cell measured at a current rate of 0.025 mA cm^{-2} under the flow ON and OFF states, (b) discharge voltage profile of the cell measured at 0.1 mA cm^{-2} and the DO content in seawater catholyte under the flow ON/OFF states, and (c) cycling performance of the cell measured at 0.025 mA cm^{-2} for 5 h at each step under the flow ON/OFF states.

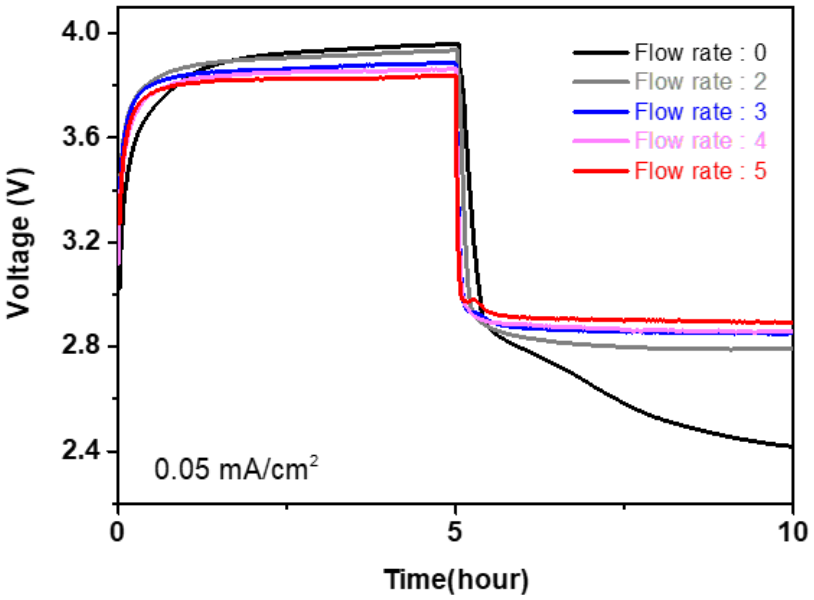

Figure 29. Flowing effect of the seawater catholyte on the charge-discharge voltage profiles of a seawater battery using a HCF current collector. The flow rate was varied by adjusting the analogue knob from 0 to 5 and the applied current density was 0.05 mA cm^{-2}

Figure 29 shows that flowing effect of the seawater batteries on the charge/discharge voltage profiles. If the flow of seawater in the flow-cell tester is not allowed, the voltage drops sharply during discharge (in flow rate:0). And although not a big difference, the higher the flow rate, the higher the discharge voltage. The discharging process of the seawater batteries is ORR, and it has been proved that it is important to supply enough oxygen through the seawater flow.

2.3.4 Exploration of the kinetic limitations

In order to investigate where the kinetic limitation mainly occurs during the operation of the seawater battery, cell tests were conducted at current rates of 0.005–0.05 mA cm^{-2}. Increasing the current density resulted in the increase of ΔV; ΔV was around 0.5 V, 0.8 V, and 1.1 V at 0.005 mA cm^{-2}, 0.025 mA cm^{-2}, and 0.05 mA cm^{-2}, respectively (Figure 30 (a)). Typically, solid electrolyte-based batteries have been recognized to show intrinsic kinetic limitations stemming from a relatively low ionic conductivity of the solid electrolyte, compared to the counterparts using liquid electrolytes [88]. We first calculated the overpotential (η) arising from the resistance of NASICON during the discharging period. Considering the ionic conductivity of ~1×10^{-3} S/cm and physical dimension of the used NASICON, the $\eta_{NASICON}$ was calculated as ~4.98×10^{-5} V, ~2.49×10^{-4} V, and ~4.98×10^{-4} V at 0.005 mA cm^{-2}, 0.025 mA cm^{-2}, and 0.05 mA cm^{-2}, respectively. The $\eta_{NASICON}$ was significantly small and hence, hardly contributed to the total η of the cell (derived from the difference between OCV and the discharge terminal voltage) that occurred during the discharging process (refer to the inset of Figure 30 (a)). This estimation implies that the main kinetic limitation (large η) is not due to the low ionic conductivity of the solid electrolyte, but rather to the sluggish kinetics of OER/ORR on the cathode current collector in seawater [43, 75].

In order to confirm this, we conducted a comparison test by replacing the HCF cathode current collector with a fast Na-ion-intercalating Ni hexacyanoferrate (NiHCF) nanoparticles-coated HCF in a seawater battery. The NiHCF is an analog of the Prussian blue coordination compound and its open framework structure allows fast kinetics of Na-ion-intercalation/deintercalation [77]. The charging and discharging processes were carried out at a current density of 0.005 mA cm^{-2}. As shown in Fig. 4b, the cell using the HCF cathode current collector had a ΔV of 0.5 V while the cell using NiHCF had a considerably small ΔV of 0.05 V. As the current rate increased up to 0.05 mA cm^{-2}, the ΔV of the HCF cell increased greatly, whereas the NiHCF cell showed relatively small ΔV values (Figure 30 (c)). From these experiments, it was found that the poor voltage efficiency of the seawater battery was mainly dominated by the slow OER/ORR on the cathode current collector rather than the ionic conductivity of the NASICON solid electrolyte. This underlines the significance of the role of the cathode current collector in seawater.

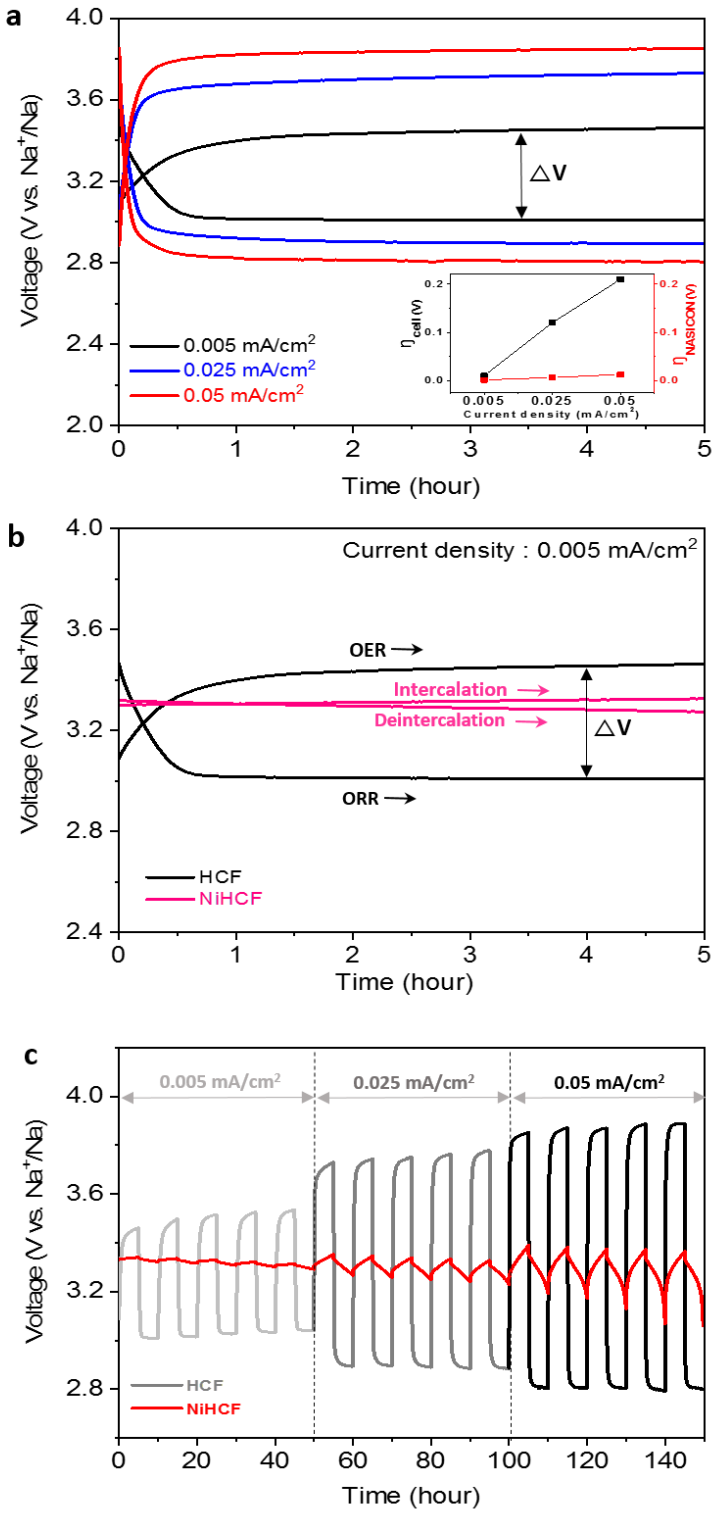

Figure 30. (a) Galvanostatic charge-discharge voltage profiles of the cell using the HCF cathode current collector at current densities of 0.005-0.05 $mAcm^{-2}$ for 5 h, (b) charge-discharge curves of the cell employing HCF and NiHCF at 0.005 $mAcm^{-2}$ for 5 h, and (c) cycle performance of the cell using HCF.

2.3.5 Effect of electrocatalysts on the cathode reaction

The OER/ORR at the cathode current collector is the dominant redox reaction determining the cell performance of seawater batteries, such as the voltage efficiency (ΔV) and rate capability. To enhance the kinetics of the cathode reactions in seawater, we employed several electrocatalysts, such as Pt/C (20 wt%), Vulcan XC-72R, cobalt-manganese oxide (CMO), and porous carbon (PC), toward the OER and/or ORR [34, 78, 89]. We prepared HCF cathode current collectors coated with the electrocatalysts and examined their effects on the cell performance. Figure 5a exhibits the SEM images of the bare HCF and catalyst-coated HCF cathode current collectors, showing the uniform distribution of catalyst particles through the carbon fibers of HCF. The electrochemical properties of the batteries were investigated by the galvanostatic charge-discharge process at a current rate of 0.025 mA cm^{-2} for 10 h at each step (Figure 31 (b)). The cells using electrocatalysts showed a small ΔV compared to the cells without any electrocatalysts (bare HCF); the average ΔV during repeated cycles was estimated at 0.86 V, 0.66 V, and 0.45 V for the bare HCF, Vulcan-coated, and Pt/C-coated cells, respectively. The Pt/C-loaded cell displayed the best cell performance among the three cells, although the high-cost issue still remains to be addressed for its practical implementation. Therefore, we employed low-cost electrocatalysts, such as PC and CMO nanoparticles, as recently reported by our group [34, 78]. The charge-discharge voltage profiles of the cells using the PC and CMO catalysts exhibited almost comparable ΔV (~0.6 V) values to those of the cell using the Pt/C (ΔV ~0.45 V) (Figure 31 (c)). The PC and CMO cells showed a good cycling performance at 0.025 mA cm^{-2} in four cycles (the inset in Figure 31 (c)). The comparison chart of the ΔV between the five cells is plotted in Figure 32. We examined total internal resistances of the five cells through the slope of polarization curves measured at a scan rate of 0.05 mV s^{-1} (refer to Figure 33and *Table 4*). The Pt/C-loaded cell and PC-loaded cell showed relatively small internal resistances of ~297 Ω and ~307 Ω, respectively, compared to those of other cells. These findings show that electrocatalysts for the OER/ORR in seawater play a significant role in enhancing the battery performance; however, further research is required to develop low-cost, high-performance electrocatalysts to ensure long-term cycling stability and high-current operation of the battery systems.

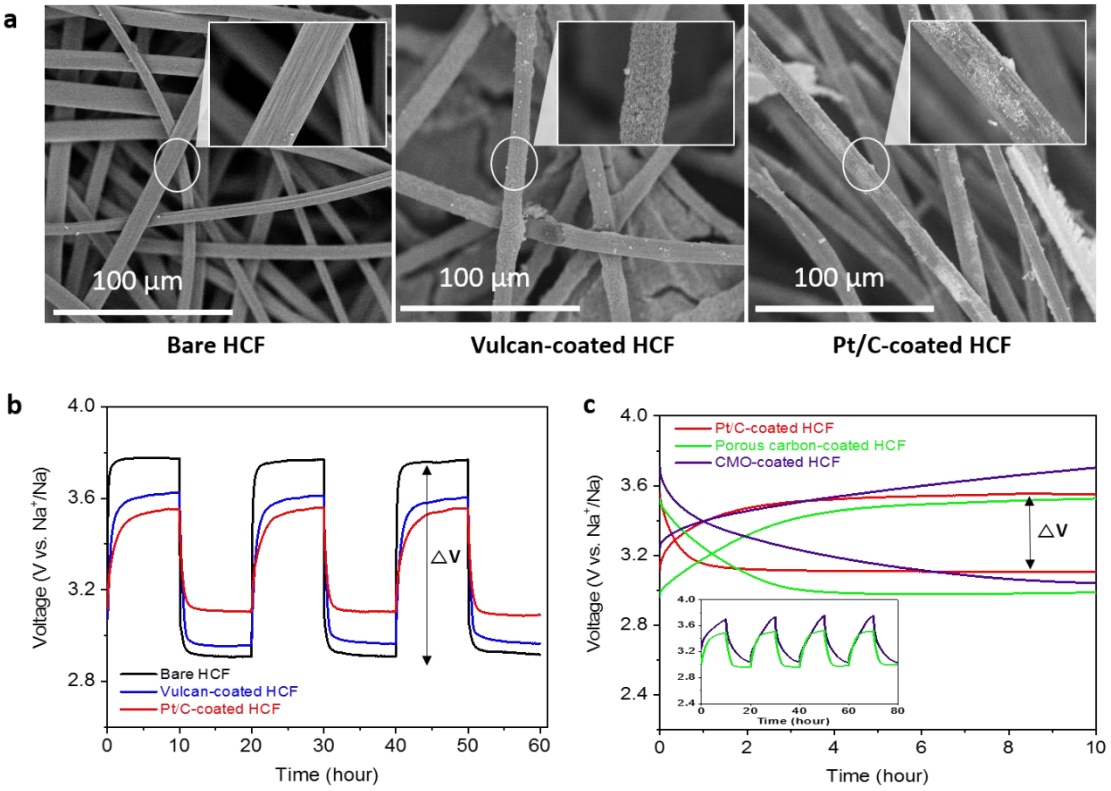

Figure 31. (a) SEM images of the bare HCF, Vulcan-coated HCF, and Pt/C-coated HCF, (b) charge/discharge curves of the cells using HCF, Vulcan-coated HCF, and Pt/C-coated HCF at 0.025 $mAcm^{-2}$ for 10 h at each step during three cycles, and (c) cycle performance of the cells with different electrocatalysts at 0.025 $mAcm^{-2}$ for 10 h at each step.

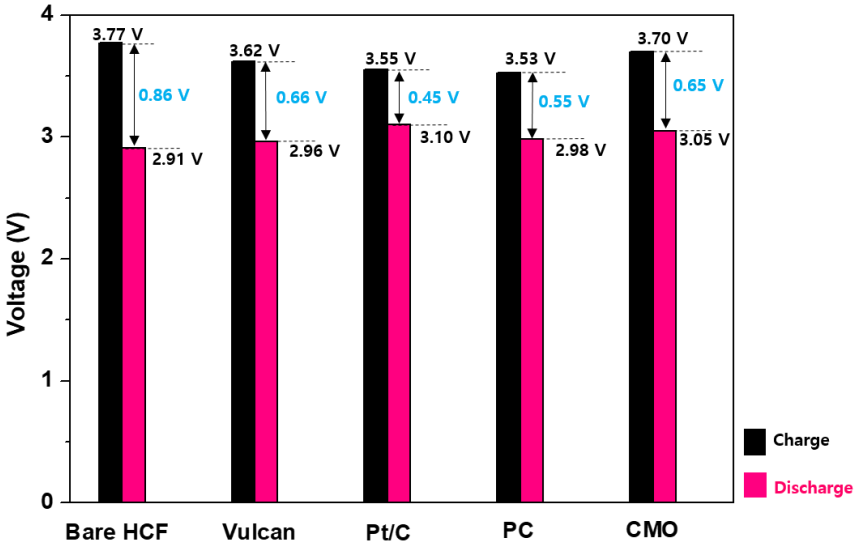

Figure 32. Comparison chart showing the charge and discharge voltages and their ΔV of the five cells with different current collectors.

To enhance the kinetics of the cathode reactions in seawater, we employed several electrocatalysts, such as Pt/C (20 wt%), Vulcan XC-72R, cobalt-manganese oxide (CMO), and porous carbon (PC), toward the OER and/or ORR [34, 78, 89]. We prepared HCF cathode current collectors coated with the electrocatalysts and examined their effects on the cell performance. Figure 32 shows that comparison chart showing the charge and discharge voltage and their voltage gap of the five cells with different cathode current collectors.

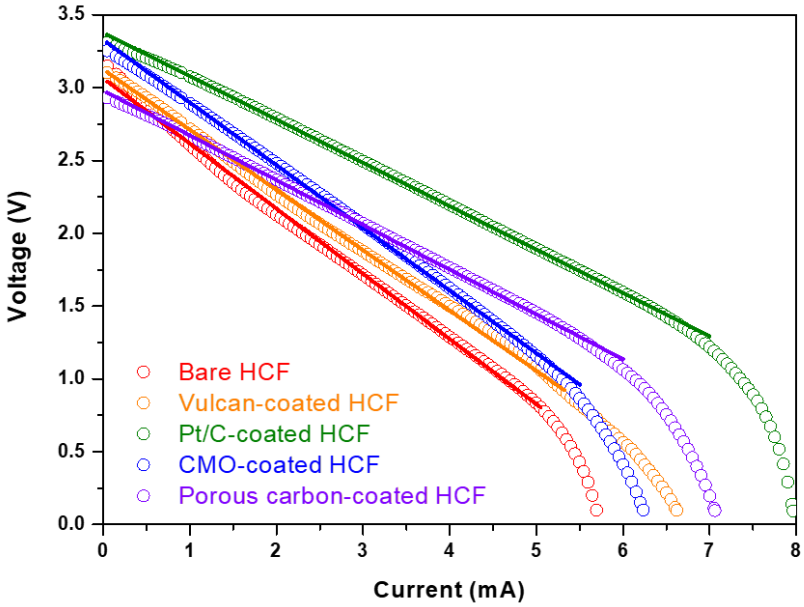

Figure 33. Polarization curves of the cells with various current collectors, measured at a scan rate of 0.05 mVs^{-1}. The resulting internal resistance was estimated from the slope of the I-V data and summarized in Table 4.

Table 4. The total internal resistance of the cells with various cathode current collectors

Sample	Bare HCF	Vulcan-coated HCF	Pt/C-coated HCF	Porous carbon-coated HCF	CMO-coated HCF
Resistance (Ω)	447	413	297	430	307

Table 5. The OCV of the cells with various cathode current collectors

Sample	Bare HCF	Vulcan-coated HCF	Pt/C-coated HCF	Porous carbon-coated HCF	CMO-coated HCF
OCV [V]	3.01	3.07	3.3	3.01	3.20

Table 6. The voltage efficiency of the cells with several kinds of cathode current collectors

Sample	Bare HCF	Vulcan-coated HCF	Pt/C-coated HCF	Porous carbon-coated HCF	CMO-coated HCF
Voltage efficiency [%]	77.5	83.2	90.0	89.1	89.9

2.4 Summary

In order to collect reliable data from the materials that are the key elements in seawater batteries, a coin-type cell, a flow-cell tester, and their key compartments were designed and fabricated by trial and error and the testing environment was also determined. We examined the wettability of seawater on the carbon felt cathode current collector and its effect on the charge-discharge cycling performance. The air-heating process of carbon felts made the surface hydrophilic, resulting in a reduced ΔV of the cell (~1.4 V) at a current rate of 0.025 mA cm^{-2}, compared to the cell using a PCF (~1.6 V). We also showed that the flow of the seawater catholyte reduced ΔV (~0.7 V) by 36% from ~1.1 V under no flow state, probably because of the facilitated diffusion of the reactants (water and DO) to the cathode current collector and thereby the decreased concentration polarization during the charge and discharge processes.

After normalizing the cell design and testing conditions, a comparative test was performed to identify the key elements for improving cell performance. The comparative study between the HCF cathode current collector and fast Na^+ ion-intercalating NiHCF electrode as the cathode showed that the OER/ORR in the seawater catholyte was the most probable rate-determining reaction of seawater batteries. The use of electrocatalyst materials in the cathode improved the battery performance, and each collected data was reliable and comparative. Therefore, further experiments on promising materials in seawater batteries can be conducted using the customized coin-type cell, which is an essential prerequisite for the practical implementation of seawater batteries as the next generation ESS.

Chapter 3

Hybrid photoelectrochemical-rechargeable seawater battery for efficient solar energy storage systems

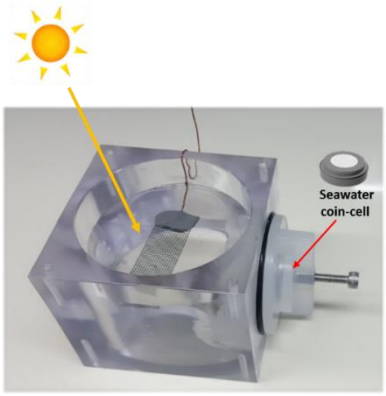

[Solar-seawater battery tester]

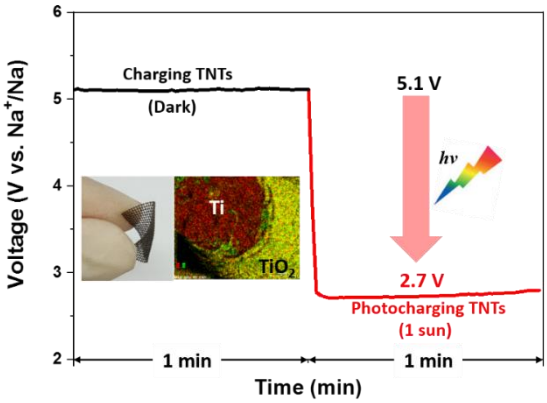

Eco-friendly harnessing of both ocean chemical energy and solar energy would represent a sustainable solution for future energy conversion/storage systems, but it has been challenging to enhance the energy efficiency of such systems for practical applications. Here, we demonstrate an efficient photoelectrochemical-assisted rechargeable seawater battery. By integrating TiO_2 nanostructure-based photoelectrodes with the seawater battery, we achieved significant enhancement of the voltaic efficiency during the charging/discharging processes; effective photocharging with the TiO_2 photoanode reduced the charging voltage to ~2.65 V, while the heated carbon felt (HCF) cathode in the seawater battery exhibited charging/discharging voltages of ~3.8 V and ~2.9 V, respectively. Such a charging voltage reduction led to a voltaic efficiency of ~109%. Moreover, interestingly, we found that TiO_2 nanostructures showed excellent photoelectrochemical performances in seawater in association with the efficient photocharging. As a result, the utilization of TiO_2 nanostructures as photocharging/discharging electrodes provides a feasible strategy to optimize the cell configuration for highly efficient solar seawater batteries.

This study was collaborate with Sangwoo Lee
(Sejong University in South Korea, Advisor : Prof. Taekjib Choi)

3.1 Introduction

In view of global climate change, the urgent need to develop efficient ways to harness and store power from sustainable energy resources has stimulated extensive research into new energy materials and novel energy conversion/storage devices. Solar rechargeable batteries based on a combination of photoelectrochemical electrodes and electrochemical cells have been emerging as novel energy conversion/storage systems, which can simultaneously obtain solar energy and store chemical energy.[90-92] However, to realize practical hybrid systems, the optimization of the cell design and configuration needs to be carried out to achieve efficient photocharging and discharging for the batteries. Especially, during photocharging, highly efficient photoelectrochemical water oxidation would be beneficial for achieving charging voltage reductions. In the case of discharging, the oxygen reduction reaction is critical for producing a high discharge voltage. Therefore, a photoelectrode with high photoelectrochemical performance would be valuable for highly efficient rechargeable batteries. The transition metal oxide-based semiconductors, such as TiO_2, Fe_2O_3, and WO_3, have been widely used as photocatalysts for photoelectrochemical (PEC) water splitting.[93-109] In practice, their highly ordered nanostructures can provide an effective route for enhancing PEC performances due to the substantial dimensional reduction of the photocatalyst in association with the larger specific surface area. These materials allow for more photogenerated charge transfers to the interfaces by reducing the charge carrier diffusion length, which can enhance water oxidation at the semiconductor/electrolyte interface.

Here, we report on a novel, low-cost, and eco-friendly solar seawater battery that uses earth-abundant natural seawater and solar energy. The most remarkable feature of this device is the simultaneous availability of both electrochemical storage and chemical fuel conversion of solar energy in one device. Figure 34 illustrates the schematic of the basic structure and the components of the solar seawater battery. The cell is composed of two compartments, a charge storage anode (sodium metal anode) in a non-aqueous liquid electrolyte and a photoelectrode in seawater, which are separated by a Na superionic conducting ceramic electrolyte (NASICON, $Na_3Zr_2Si_2PO_{12}$).[37] Considering the pH of seawater (~8), Na^+ ion content in seawater (~0.47 M), and oxygen partial pressure at 100% saturation from ambient air (~0.2 atm), the overall reactions during the charge/discharge processes and the theoretical cell voltage (E_{cell}) can be described as shown below.[110]

$$4Na(s) + O_2(aq) + 4H^+(aq) \leftrightarrow 4Na^+(aq) + 2H_2O(l);\ E_{cell} = 3.48\ V\ vs.\ Na/Na^+ \quad (1)$$

During discharging, the Na metal anode is oxidized to Na^+ and transported into the seawater catholyte through the NASICON ceramic membrane. Simultaneously, the oxygen reduction reaction

(ORR) occurs, with the formation of water soluble NaOH at the cathode side. During charging, the Na^+ in the seawater catholyte is extracted and transported into the anode, while the oxygen evolution reaction (OER) occurs at the cathode side. By the way, the solar seawater battery can be charged by using the PEC electrode, unlike the existing seawater battery charging process, and the charging voltage can be significantly reduced. The photocharging process is shown in Figure 34**.** Upon charging under illumination, the photoexcited electrons (e^-) in the conduction band (CB) of the photoelectrode transfer into the anode part by outside circuit, thus resulting in the reduction of Na^+ into Na. At the same time, the photoexcited holes (h^+) left in the valence band oxidize seawater into O_2. Thus, the theoretical photocharging voltage of the cell was estimated to be ~2.05 V on the basis of the potential difference between the redox potential of the Na^+/Na couple and CB of the semiconducting anatase-TiO_2 (Figure 35).

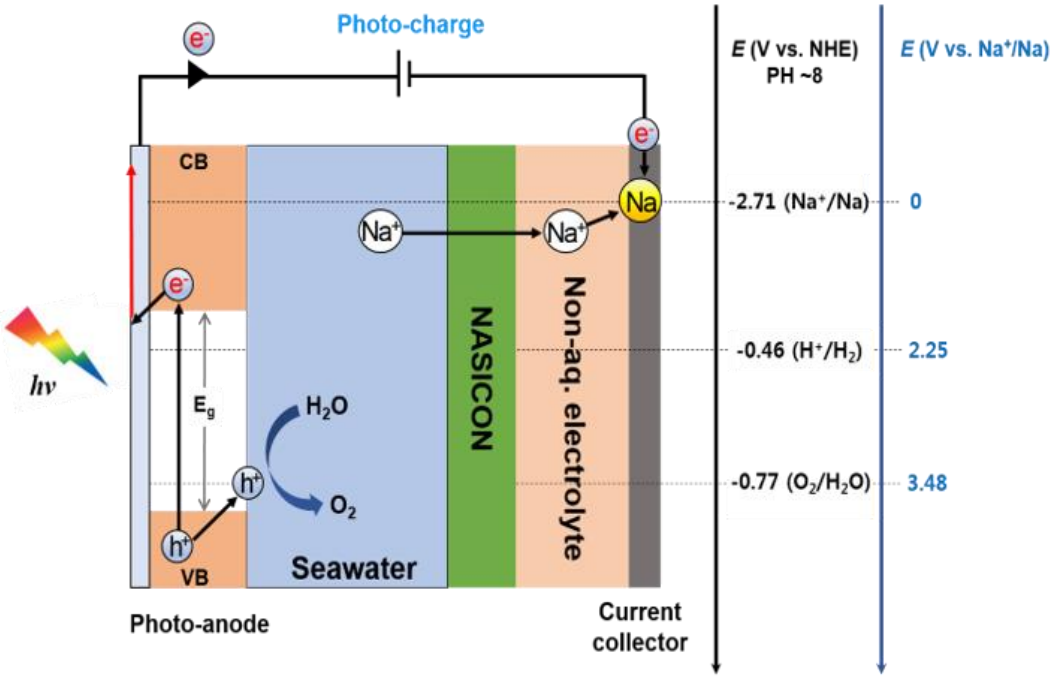

Figure 34. Energy diagram and schematic illustration of the photo-charging process.

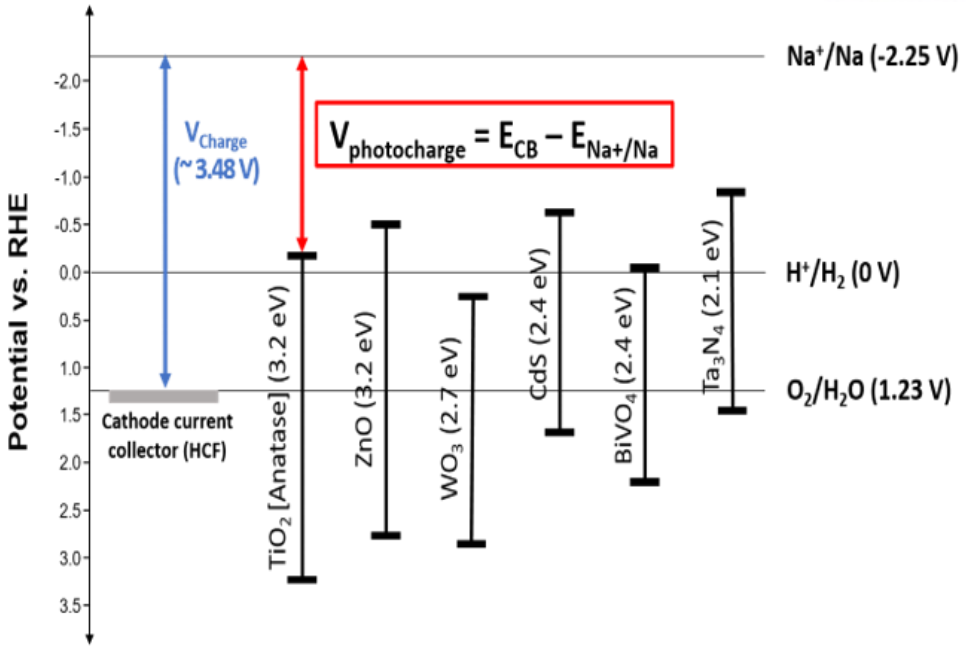

Figure 35. Candidates for solar seawater battery photo-anodes and energy diagram for theoretically needed photocharging potential compared with Heat treatment Carbon felt (HCF) as a cathode current collector.

Figure 35 shows several candidates that can be used as photoanode. Existing seawater battery cell uses HCF current collector as a cathode, the theoretical charging voltage is ~ 3.48 V. When TNTs photoanode is used, the theoretical photocharging voltage is ~ 2.05 V (Vphotocharge = ECB – ENa+/Na). In this experimental, TNTs was used as photoanode, but various photoelectrodes such as ZnO, WO3, and CdS could be applied to solar seawater battery system.[111-130]

In this work, we designed an optimized single device to test the solar seawater battery system with a photoelectrochemical cell by a using anatase-TiO_2 nanotube arrays (TNTs) photoelectrode. Compared to heated carbon felt (HCF), which is used as a cathode current collector in seawater batteries,[40] the use of TNTs photoanode resulted in a ~29% reduction in the charging voltage. Also, it was found that charging/discharging was possible through only TNTs photoanode and the voltage efficiency could be increased by dividing the photocharge part and discharge part. In the future, various photoelectrodes in addition to TNTs photoanode can be applied to such a solar seawater battery system.

3.2 Experimental detail

3.2.1 Preparation of the cell components

NASICON ceramic membrane ($Na_3Zr_2Si_2PO_{12}$) was used as a solid electrolyte to separate the seawater cathode from the anode. The NASICON solid electrolytes were fabricated by a solid-state reaction based on our previous study (Figure 36, Figure 37).[38, 75, 76] The ionic conductivity of the NASICON ceramic membrane was measured as ~5×10^{-4} S cm^{-1} and the density was measured as ~3.16 g cm^{-3} (~95% of the theoretical value) at room temperature (Figure 38). Carbon felts (XP-30A, Toyobo Co., Ltd) with an electrical resistance of 0.15–0.20 Ωcm^2 were used as the cathode current collector. Prior to use, carbon felts were heat-treated to improve the hydrophilicity of the surface at 500°C (at a ramping rate of 2°C min^{-1}) for 2 h in ambient air.

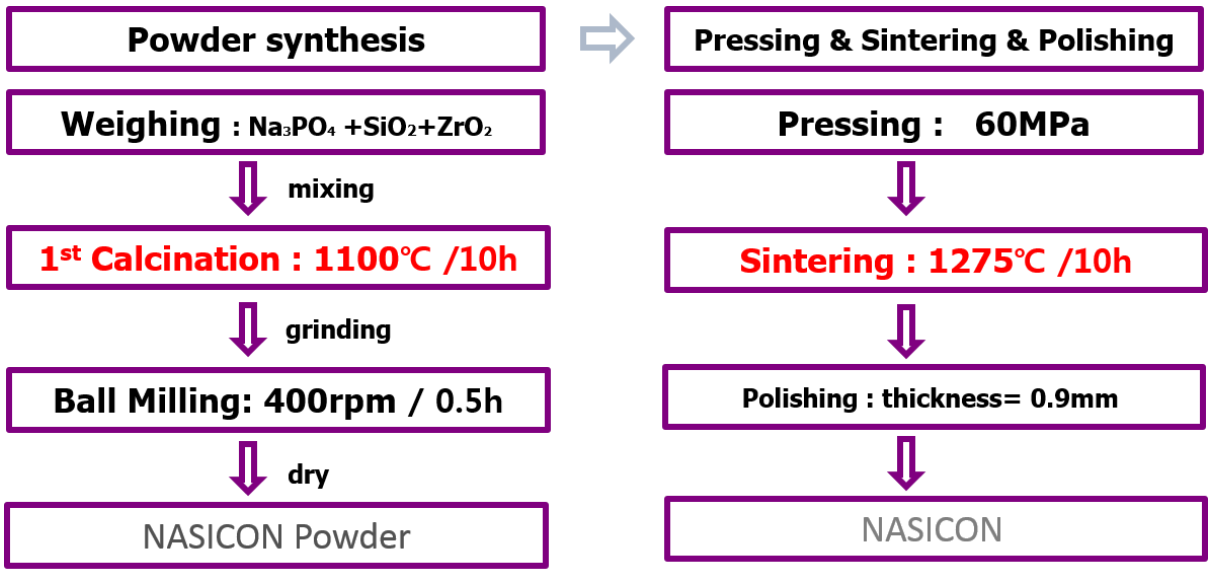

Figure 36. Synthesis and fabrication process of NASICON membrane. [13, 26, 27]

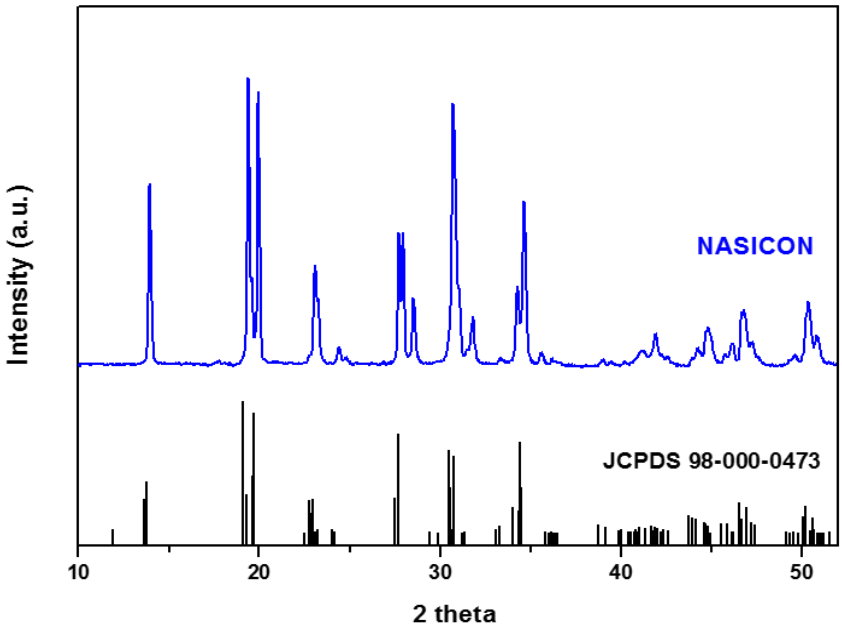

Figure 37. XRD patterns of the synthesized NASICON pellet.

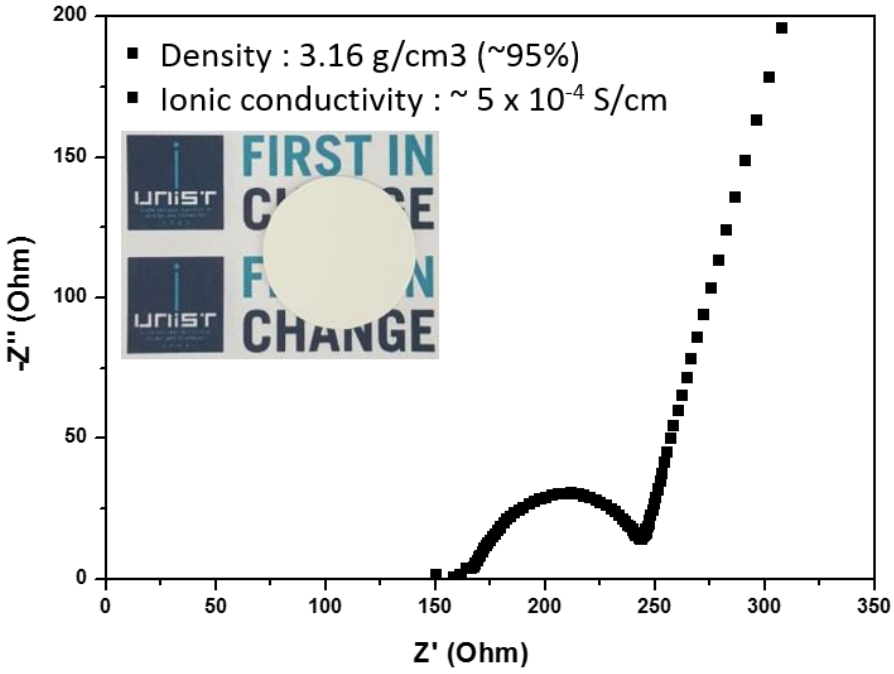

Figure 38. Nyquist plot of the NASICON ($Na_3Zr_2Si_2PO_{12}$). The inset shows a digital image of the NASICON.

3.2.2 Preparation of the anatase-TiO_2 nanotube array photoelectrodes

The highly ordered and hierarchical nano-porous TNTs consisting of a nano-porous top layer with ~100 nm pore size and smooth underlying nanotubes were fabricated by a two-step anodization process. Prior to anodization, the Ti mesh (nominal aperture of 0.6 mm and wire diameter of 0.3 mm) were prepared by sonicating the material in ethanol followed by electro-polishing. The anodization was performed by using a conventional two-electrode system with the Ti mesh as a working electrode and a Pt counter electrode in aqueous electrolytes consisting of 0.3 wt% NH_4F (ammonium fluoride ACS reagent, 98.0%, Sigma Aldrich) and H_2O at a concentration of 2% in ethylene glycol (99.5%, Samchun). For the first step of anodization, Ti mesh was anodized at 60 V and 15°C for 12 h, and then, the as-grown nanotube layer was completely removed in aqueous hydrogen peroxide for 15 min ultrasonically. The second anodization step was carried out for 1 h under the same conditions as the first anodization step. After the second anodization, amorphous TNTs were rinsed with deionized (DI) water and annaled to yield the anatase phase at 500°C for 1 h in air.

3.2.3 Cell assembly and electrochemical testing

Coin-type solar seawater batteries were assembled by the following procedure. For the Na metal anode compartment, the NASICON membrane was attached to the open-structured top part of the anode. Sodium metal (99.9%, Sigma Aldrich) was attached to the surface of a spacer and the non-aqueous electrolyte consisting of 1 M $NaCF_3SO_3$ in tetraethylene glycol dimethylether was injected. The cell assembly was performed in a glove box under a high purity argon atmosphere (oxygen and water < 1.0 ppm). The assembled anode compartment was put into the special apparatus with an open-structured cathode (4TOONE Energy Co., Ltd), where the photoanode and cathode current collector were immersed in natural seawater form Ilsan beach, Ulsan, Republic of Korea (GPS 35.497005, 129.430996).[35] The electrochemical properties of the cells were evaluated by using a potentiostat (VSP-300, Biologic) at room temperature. The charge/discharge characteristics of the cells were tested at current rates of 0.015/0.025 mA cm^{-2} for 1 h. The PEC properties were evaluated by using a potentiostat (VSP-300, Biologic) with a three-electrode configuration. The TNTs electrode, a Pt electrode, and a saturated Ag/AgCl (3M KCl) electrode were used as the working, counter, and reference electrodes, respectively. The current density–voltage (J-V) curve of the scan rate was 20 mV s^{-1}. The light source was a 150 W Xenon lamp, which was used to simulate the 1 Sun irradiation condition (AM 1.5G, 100 mW cm^{-2}) by using a solar simulator (Oriel 94021A). The applied bias photoconversion (photo-to-current, η_{APE}) was obtained from the photocurrent density–potential curves through calculations with the following equation: $\eta_{APE} = J_{ph}(1.23 - V_{RHE})/P$, where J_{ph} is the photocurrent density, V_{RHE} is the

applied bias potential versus reversible hydrogen electrode (RHE), and P is the power density of incident light (100 mW cm^{-2}).

3.2.4 Characterizations

X-ray diffraction (XRD) was performed with a D/Max, Rigaku apparatus equipped with a Cu-Kα X-ray source (λ =1.5406 Å). The chemical bonding states of the TNTs were analyzed by X-ray photoelectron spectroscopy (XPS, PHI 5000 VersaProbe) with an Al Kα X-ray source. The surface morphology was observed by scanning electron microscopy (SEM, FEI Verios 460), and the composition was determined by energy dispersive X-ray spectroscopy (EDX, Bruker Xflash 6130).

3.3 Results and discussion

The basic structure and components of the solar seawater battery cell are schematically depicted in Figure 39. A photograph of the solar seawater battery tester is shown in Figure 40. First, we designed and optimized the solar seawater battery tester. The whole part of the tester was made polypropylene material to prevent rust from forming when exposed to corrosive seawater, and the tester was designed to be transparent to maximize sunlight utilization. Also, stirring was carried out at 600 rpm in order to supply the reaction site (on the photoelectrode) with sufficient amounts of reactant (water and oxygen), and the inside was made round to smooth the flow of the seawater catholyte. The seawater coin-cell was assembled into the cell tester by turning, and the photoelectrode was laid horizontally in the middle of the tester so that it could absorb sufficient amounts of sunlight.

As a photoelectrode for the photoelectrochemical cell, we used anatase-TNTs because of their excellent chemical stability and strong surface catalytic activity. In particular, the TNTs were prepared on titanium (Ti) mesh, which can serve as a precursor for TNTs directly and form three-dimensional (3D) vertical nanostructures. Moreover, the unique open area of the Ti mesh benefits the flow of electrolyte and the mesh structure provides extra lateral surfaces and flexibility (inset of Figure 42 (a)). Figure 42 (a) shows an SEM image of the photoanode composed of 3D vertical TNTs on Ti mesh. We controlled the morphology of TNTs for the hierarchical top-nanopore/bottom-nanotube structures by optimizing the parameters during the two-step anodization process, as shown in Figure 42 (b). The hierarchical TNTs allowed for enhanced photoelectrochemical performances because of the high specific surface areas in contact with the electrolyte, the high light harvesting efficiency made possible by superior light scattering, and the high electron mobility provided through one-dimensional (1D) nanostructures.[131] Cross-sectional SEM (Figure 42 (c)) and EDX (Figure 42 (d)) views of the anodized Ti wire clearly demonstrate that TiO_2 grew radially in an outward direction around the wire uniformly. Meanwhile, zoomed-in SEM and EDX images (see insets of Figure 42 (c) and (d)) of the TNTs/Ti wire show that that the TiO_2 formed highly ordered tubular structures with lengths of ~800 nm. The XRD profile of the TNTs/Ti mesh is presented in Figure 41 (a). We observed the main diffraction peak of the (101) plane at $2\Theta = 25.4°$, which was indicative of the highly crystalline anatase phase of TiO_2. The surface chemical bonding of TNTs was characterized by XPS (Figure 41 (b)). The high-resolution spectrum of the Ti 2p core level presented a typical Ti^{4+} valence state in TiO_2 with $2p_{3/2}$ and $2p_{1/2}$ peaks centered at 458.7 eV and 464.3 eV, respectively.

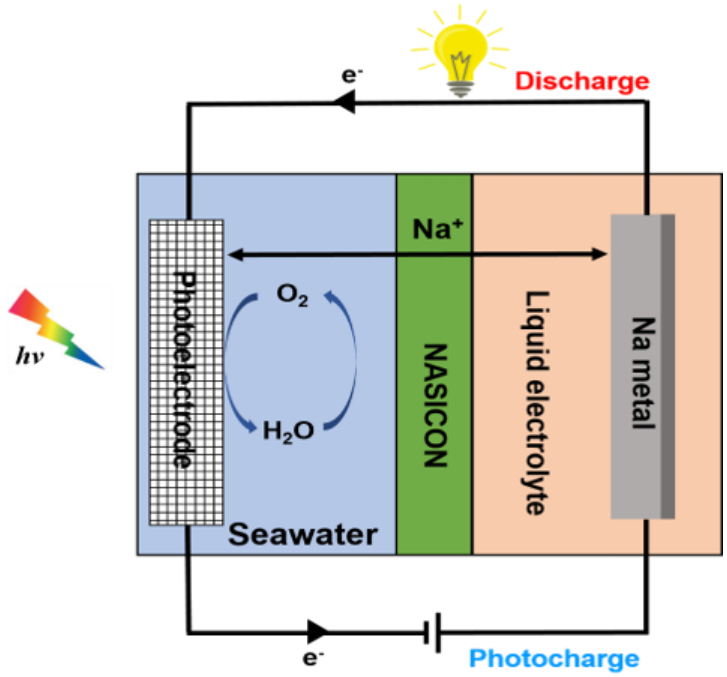

Figure 39. Schematic diagram of the cell configuration of a solar seawater battery.

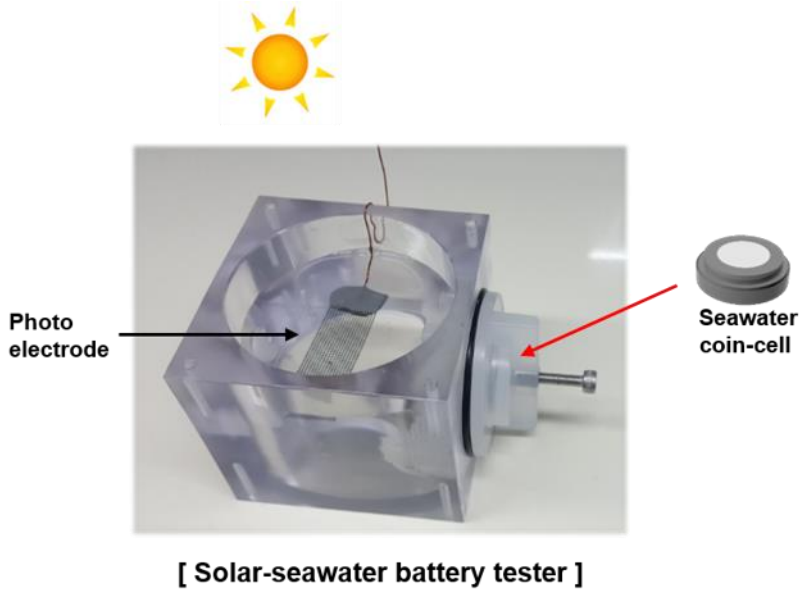

Figure 40. Digital image of a used solar seawater cell tester.

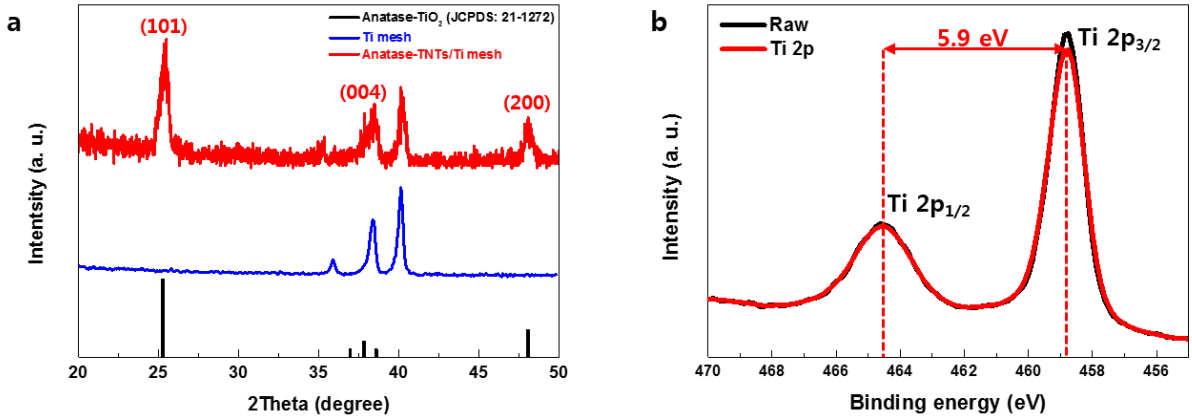

Figure 41. (a) XRD patterns of anatase-TNTs/Ti mesh and (b) The high-resolution XPS spectra of Ti 2p for anatase-TNTs

Figure 41 (a) shows XRD patterns of anatase-TNTs/Ti mesh that prepared by anodization and annealing at 500 ℃. All XRD patterns were attributed to the diffraction of anatase TiO_2 (JCPDS 21-1272) and Ti metal mesh. We observed the main diffraction peaks at 2Θ = 25.4˚, 37.8 ˚, and 48.02 ˚ corresponding to the (101), (004), and (200) planes of anatase-TNTs, respectively, indicating of high crystallinity. The other peaks are assigned to diffraction from the Ti metal mesh. Figure 41 (b) presents the high-resolution spectrum of Ti 2p core level. The Ti 2p doublet was well deconvoluted into $2p_{3/2}$ (458.7 eV) and $2p_{1/2}$ (464.6 eV) peaks, respectively, with separation of 5.9 eV, which are consistent with typical Ti^{4+} valence state in TiO_2 tetragonal structure.[132, 133]

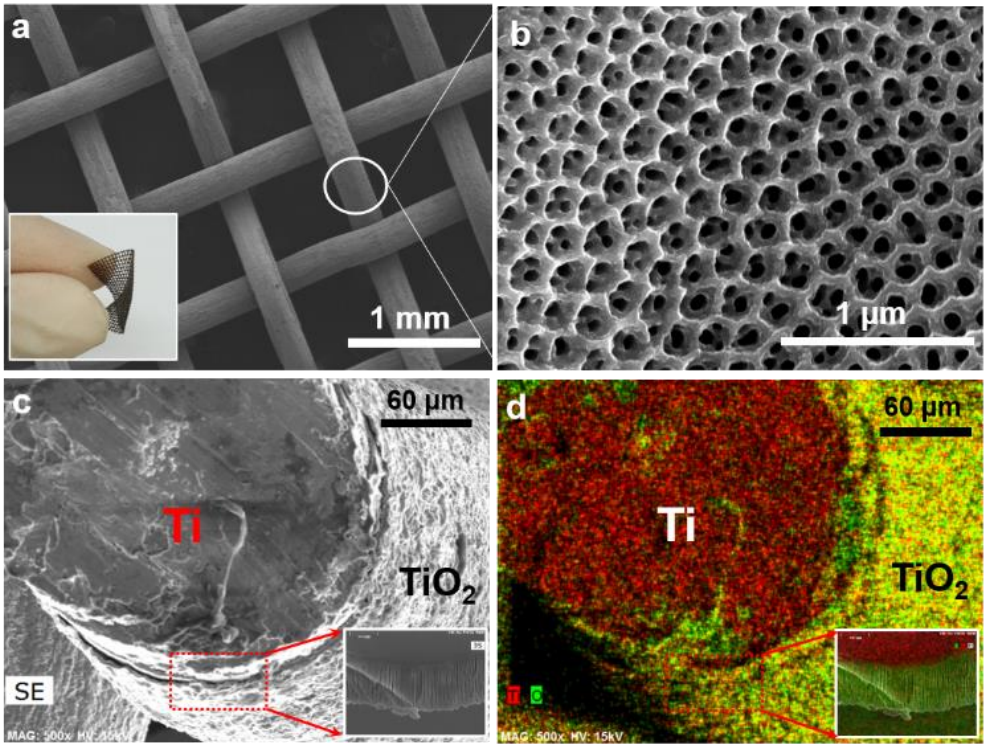

Figure 42. (a, b) SEM images of the surface morphologies of the anatase-TNTs photoanode (the inset in (a) shows pictures of the TNTs photoanode). (c), (d) Cross section of SEM-EDX images of the TNTs photoanode.

To evaluate the photoelectrochemical performances of TNTs for seawater splitting, linear sweep voltammetry (LSV) measurements were carried out in seawater (pH ~8) electrolyte under simulated solar light illumination (AM 1.5G, 100 mW cm^{-2}). As shown in Figure 46 (a), the LSV curve exhibited no observable dark current even up to a high potential of 1.6 V_{RHE}, and a significant photocurrent density as high as ~1.42 mA/cm^2 at 1.23 V_{RHE} was observed under light illumination as well as low onset potential of 0.2 V_{RHE}. The photoconversion efficiency (η_{APE}) of the TNTs photoanode was calculated. Figure 43 shows the change of photoconversion efficiency as a function of applied bias potential (V_{RHE}). The maximum value of η_{APE} reached 0.5% at 0.68 V_{RHE}, which is comparable to the reported value for pristine TiO_2 nanostructures.[134] The transient photocurrent response of TNTs was measured at 0.7 V_{RHE} with on and off cycles of light illumination (Figure 46 (b)). When the light was switched on, the photocurrent increased suddenly to a transient maximum, and then, it gradually decayed to a relatively steady-state. The current returned to nearly zero immediately once the illumination was switched off. Such photocurrent responses were fast and reproducible during repeated light on/off cycles, thus demonstrating the stability and reproducibility of a TNTs under successive cycles. On the other hand, we observed photocurrent decay in transients, which could have been attributed to the redistribution of the interfacial potential through the charge carrier accumulation at the electrode–electrolyte interface or trapping of electrons or holes in intermediate surface states. For further understanding of the photocharge carrier transport and recombination properties, the open-circuit potential response was measured under light on and off cycles, which were accompanied by photovoltage relaxation from a quasi-equilibrium state (i.e., pseudo Fermi level for photogenerated holes) under illumination to the equilibrium (Fermi level of TNTs for electrons) at darkness. In other words, as shown in Figure 44 (a), when switching the light on from a steady-state in the dark, the TNTs exhibited a negative shift of photovoltage due to photogenerated electron accumulation, thus resulting in rapid shifts of the Fermi level to cathodic potentials. Meanwhile, when switching the light off, subsequently, gradual photovoltage decay was observed until the Fermi level returned to an original level due to the charge recombination. The corresponding response time clearly increased with photovoltage decay, thus indicating a long electron lifetime (Figure 44 (b)). In addition, we measured the electrochemical impedance spectroscopy (EIS) at 0.7 V_{RHE} with an AC frequency range from 0.01 Hz to 700 kHz under simulated sunlight. Figure 45 presents the comparison of Nyquist (Figure 45 (a)) and Bode plots (Figure 45 (b)) of EIS data in different 1 M KOH (pH = ~14) and seawater (pH = ~8) electrolytes. Interestingly, we observed one single semicircle and one broad peak in the Nyquist and Bode phase at the low frequency range irrespective of electrolytes, thus demonstrating evidence of a single lifetime or relaxation time of charge carriers. The electron lifetime (τ_e) in the TNTs can be obtained from the characteristic angular frequency (ω) of the middle frequency (f) peak in the Bode phase plots by using the relation of $\tau_e = 1/\omega = 1/2\pi f$. The characteristic frequency for the TNTs was 1.21 Hz and 2.17 Hz,

which correspond to the electron lifetimes of 131 ms and 73 ms in seawater and 1 M KOH, respectively. It is noteworthy that the electron lifetime in seawater was 1.8 times that in 1 M KOH and a smaller semicircle radius was obtained in seawater. Therefore, it was obvious that the TNTs in seawater exhibited low recombination rates as well as effective charge carrier separation, thus leading to easier water oxidation. According to previous work by Zhang *et al.*,[135] significant enhancement of the photocurrent density in NaCl-containing electrolyte can be attributed to the adsorbed Cl^-. That is, the modified chloride on the TiO_2 surface can effectively trap the photogenerated holes and thus promote charge carrier separation, as demonstrated by our EIS analysis for TNTs in seawater electrolyte. As a result, such effective water oxidation can be expected for efficient photocharging in the seawater battery. Beyond the PEC water oxidation, an oxygen reduction peak was clearly observed in TNTs under 1 Sun illumination, as can be seen in the cyclic voltammetry tests of TNTs (Figure 46 (c)). This indicates that TNTs have suitable photoelectrochemical activity during the discharging process in the seawater battery.

The TNTs photoanode was employed in the seawater cell for the photocharging process (Figure 46 (d)). The solar seawater battery showed 0.18 mA cm^{-2} of photocurrent at 3.48 $V_{Na+/Na}$, and the onset potential was 2.48 $V_{Na+/Na}$ in the two-electrode configuration. In the dark state, there was no photocurrent. We also performed chronoamperometric measurements at 3.48 $V_{Na+/Na}$ of applied bias for 5 h, which yielded an average ~0.17 mA cm^{-2} of photocurrent (Figure 47). These results confirmed that the TNTs photoanode can stably produce a photocurrent in seawater for a long time under solar irradiation. We also confirmed that it is possible to charge the seawater cell by using the TNTs photoanode. Thus, we integrated the photoanode into the actual seawater cell to investigate how much the charging voltage can be lowered.

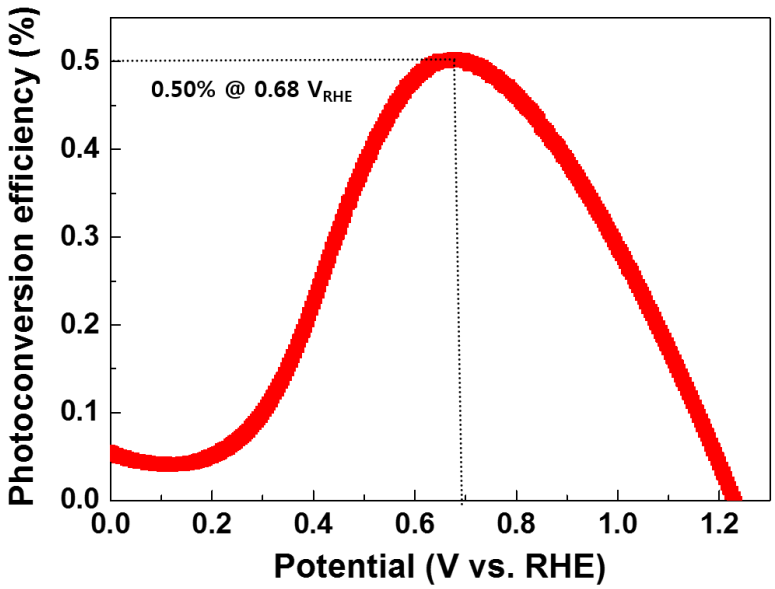

Figure 43. The applied bias photon-to-current efficiency (η_{APE}) of anatase-TNTs in seawater.

Figure 43 represents the change of photoconversion efficiency as a function of applied bias potential (V_{RHE}). The applied bias photo-to-current efficiency (η_{APE}) was calculated from J-V curves, assuming 100% Faradaic efficiency through the following Equation:

$$\eta_{APE}(\%) = J_{ph}(V_{rev} - V_{RHE})/P_{light}$$

where η_{APE} is the photoconversion efficiency, J_{ph} is the photocurrent density (mA/cm^2), V*rev* is the standard reversible potential which is 1.23 V vs. RHE, V_{RHE} is the applied bias potential versus reversible hydrogen electrode, and P_{light} is the power density of the incident light irradiance (100mW/cm^2). The potentials were measured versus the Ag/AgCl reference electrode and converted to the reversible hydrogen electrode (RHE) scale using the Nernst function:

$$E_{RHE} = E_{Ag/AgCl} + E^{\circ}_{Ag/AgCl\ vs.\ SHE} + 0.059 \times pH$$

where E_{RHE} is the converted potential versus RHE, $E^{\circ}_{Ag/AgCl\ vs.\ SHE}$ is the potential of the Ag/AgCl reference electrode with respect to the standard hydrogen potential (SHE) and $E_{Ag/AgCl}$ is the external potential measured against the Ag/AgCl reference electrode. $E^{\circ}_{Ag/AgCl\ vs.\ SHE}$ is 0.1976 V $_{vs\ SHE}$ at 25℃.

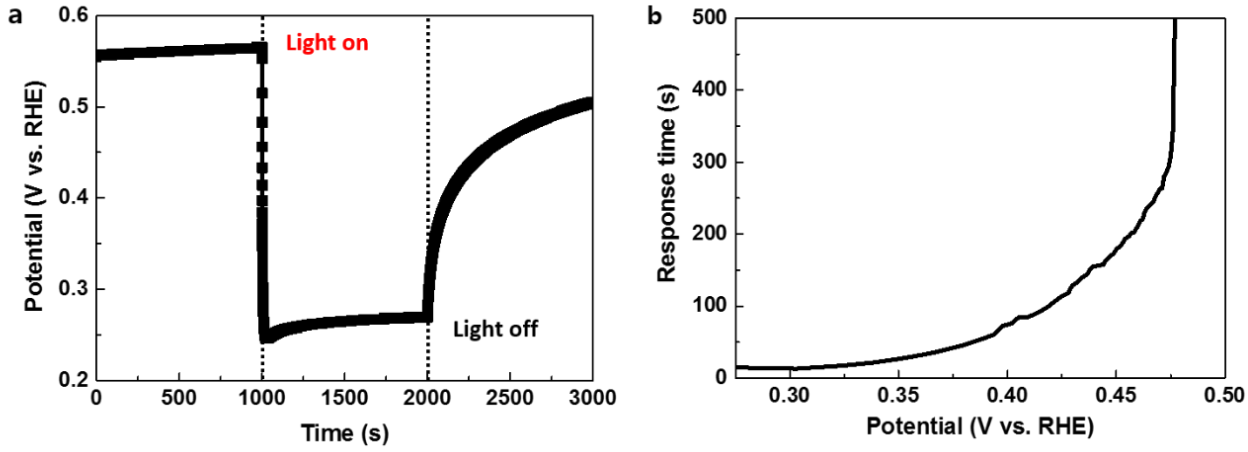

Figure 44. (a) The open-circuit photovoltage response of anatase-TNTs in seawater. (b) Response time versus open circuit potential.

The open-circuit photovoltage (V_{oc}) response measurement was conducted to estimate the photogenerated electron lifetime and thus to evaluate the recombination rate of the photogenerated electrons and holes. Lifetime of photogenerated electrons is related to the photovoltage decay rate by the following equation:

$$\tau_n = \left[-\frac{K_B T}{e}\right]\left[\frac{dVoc}{dt}\right]^{-1}$$

where τ_n is the potential dependent electron lifetime, K_B is Boltzmann constant, T is the Kelvin temperature, e is the charge of a single electron, and Voc is the open circuit potential at time t.
As shown in Figure 44, TNTs photoelectrode exhibits a prolonged electron lifetime.

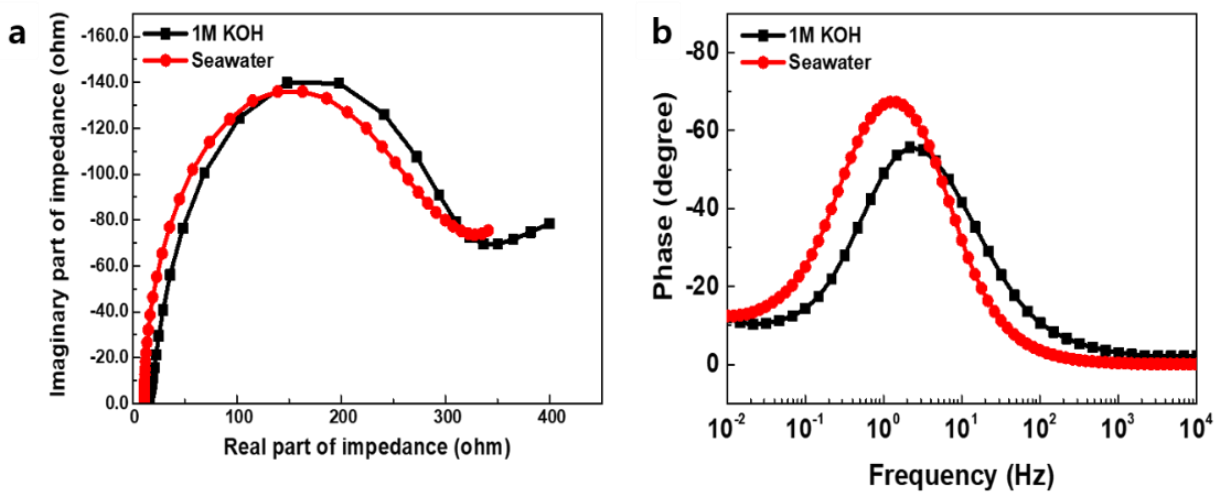

Figure 45. Electrochemical impedance spectroscopy (EIS) for anatase-TNTs at different 1M KOH (pH = ~14) and seawater (pH = ~8) electrolytes under irradiation at 0.7 V vs. $_{RHE}$: (a) Nyquist plots and (b) the Bode plots.

We used electrochemical impedance spectroscopy to study the charge transfer characteristics of the TNTs photoelectrodes. We compared Nyquist plots and Bode phase plots for TNTs in 1M KOH and seawater electrolytes under 1 sun illumination. The charge transfer resistance at the photoelectrode/electrolyte interface can be estimated from the semicircle diameters in Nyquist plots. TNTs exhibit small charge transfer resistance, demonstrating excellent PEC performances in seawater and 1M KOH.

Typically, two characteristic frequency peaks can be observed in the Bode phase plots of the impedance spectra. The low-frequency peak in the range of 1 ~ 100 Hz reflects the electron transfer in the photoelectrode and charge reaction at the photoelectrode/electrolyte interface, and the high-frequency peak (in the kHz range) corresponds to the charge-transfer at the counter electrode.

As confirmed in Figure 44, TNTs show only single peak in low frequency region, indicating a remarkable electron lifetime. Interestingly, TNTs in seawater has longer electron lifetime than that in 1M KOH.

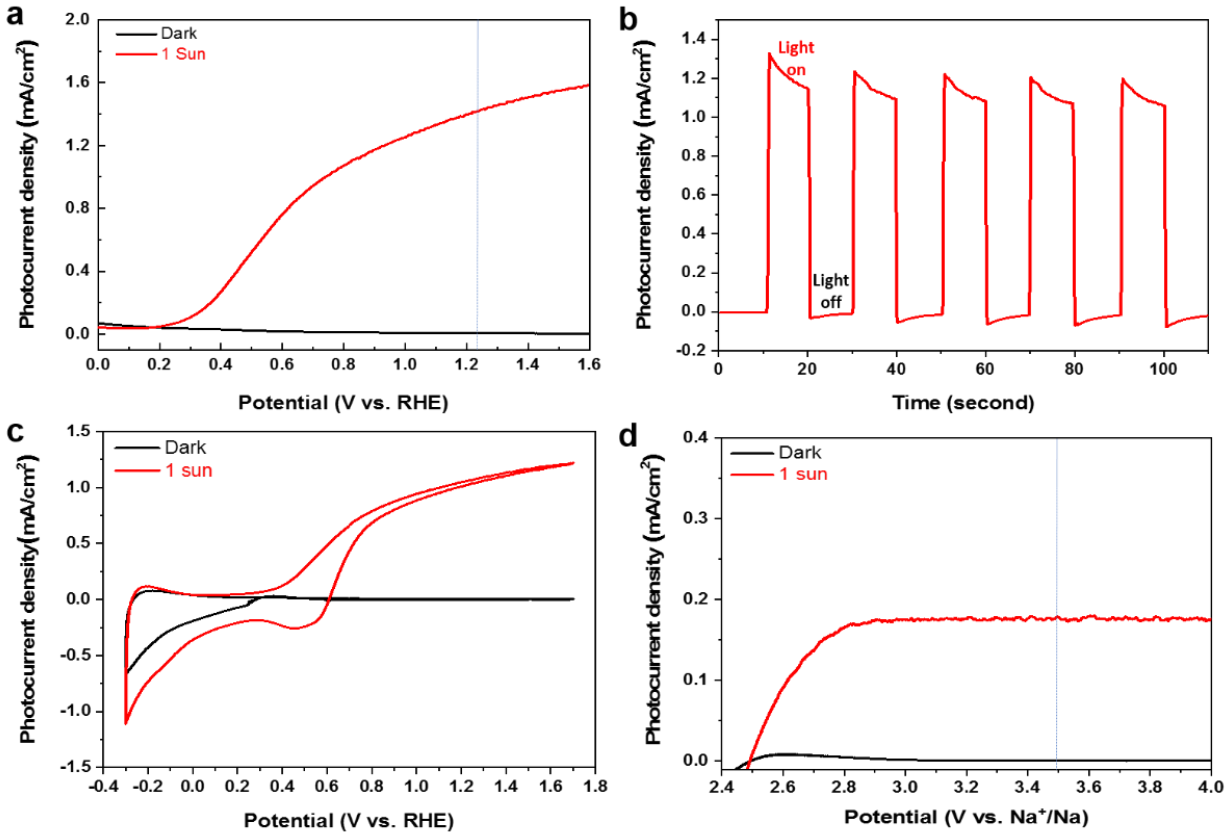

Figure 46. (a) J-V curve of the TNTs photoanode in a three-electrode configuration with a Pt wire rod counter electrode, (b) transient photocurrent density versus time plots at an applied potential of 0.7 VRHE with light on/off cycles, and (c) cyclic voltammetry curves collected with a scan rate of 20 mV/s under simulated solar light (AM 1.5G). (d) The two-electrode system (seawater coin-cell) with a Na counter electrode, for which the photoelectrochemical properties of the anatase-TNTs photoanode are given.

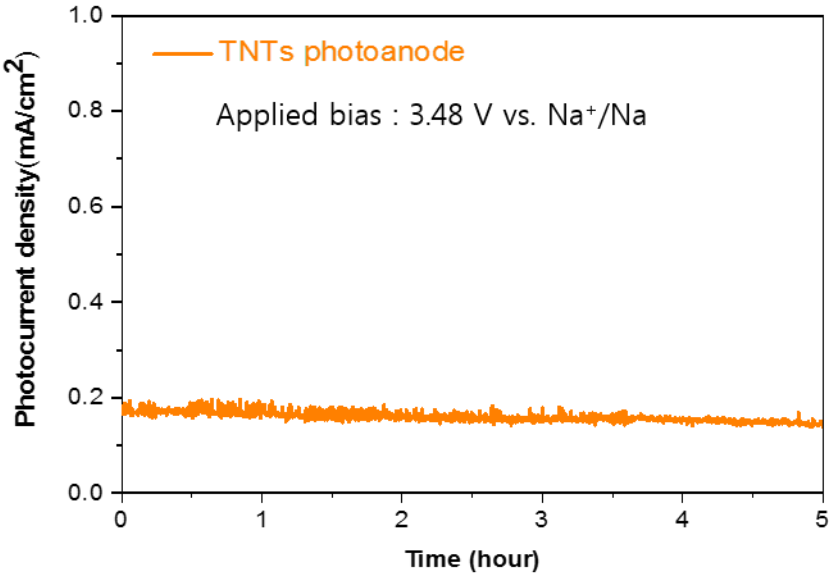

Figure 47. Photocurrent generation at constant potential of 3.48 V vs. Na^+/Na in two electrode system

Figure 47 shows that TNTs photoanode can stably produce photocurrent in seawater for a long time (5 h) under 1 sun irradiation. We performed chronoamperometric measurement at 3.48 $V_{Na+/Na}$ of applied bias for 5 h, which shows average ~ 0.17 mA cm^{-2} of photocurrent.

In order to confirm the feasibility of reducing the charging voltage of the solar seawater battery integrated with the photoelectrochemical electrode (TNTs/Ti), we compared the photocharging effects of TNTs as the photoanode and HCF as the cathode current collector for the existing seawater battery. The theoretical charging voltage of the seawater battery was ~3.48 V in seawater (pH ~8). The test was carried out under 1 Sun illumination and in the dark for 1 min each (Figure 48 (a)). When we charged the seawater battery with the HCF cathode current collector, the charging was performed consistently at ~3.8 V at 0.015 mA cm^{-2} regardless of the presence of sunlight. In contrast to HCF, for the TNTs photoanode, the charging was performed at a high voltage of ~5.1 V in the dark because of sluggish OER reactions. Meanwhile, the charging voltage was reduced to ~2.7 V under illumination (theoretical photocharging voltage of ~2.05 V, $V_{photocharge} = E_{CB} - E_{Na+/Na}$), which corresponds to a charging voltage reduction of ~29%. As a result, we concluded that the charging voltage of the seawater battery can be effectively lowered through photoelectrochemical water oxidation, thus leading to enhancement of the voltaic efficiency.

The TNTs photoanode was employed not only for the charging process, but also for the discharging process (Figure 48 (b)). When charging and discharging were carried out under the condition of 0.015 mA cm^{-2}, the existing seawater cell with the HCF cathode was charged at ~3.8 V and discharged at ~2.9 V. On the other hand, under solar illumination on the TNTs photoanode, the charge and discharge proceeded at ~2.65 V and ~2.50 V, respectively. In the case of the HCF cathode, the voltage efficiency was ~76%, while the TNTs showed a relatively higher voltage efficiency of ~94%. This confirmed that an efficient high voltage battery can be obtained by using TNTs photoanode. Also, as shown in Figure 48 (b), two voltage regions were identified in the charging/discharging process of the HCF cathode current collector. During the charging/discharging processes, the initial slope regions between ~2.9 V and ~3.6 V were formed by non-faradaic reactions through anion (Cl^-, SO_4^{2-}, etc) adsorption/desorption, and then, this was followed by OER after ~3.6 V and ORR after ~2.9 V corresponding to plateau regions.[136, 137] On the other hand, the TNTs photoanode showed only a single plateau region arising from mainly OER/ORR throughout the photocharging/discharging processes. Consequently, the high performance bifunctional (photo)electrocatalytic activity of TNTs in photocharging/discharging processes was found to be beneficial for obtaining high energy efficiency in the solar seawater battery. The discharge process of a solar seawater battery proceeds via the ORR on the photoelectrode. Because TNTs/Ti mesh is chemically stable in seawater, it is very useful as a photoanode not only for charging, but also for discharging in a solar seawater battery. We found that TNTs photoanode exhibited very stable cycling performance during the charging and discharging cycles (Figure 48 (c)). Moreover, we observed no significant structural and morphological change of TNTs photoanode from SEM images before (Figure 49 (a)) and after (Figure 49 (b)) the cycles. The discharging voltage was higher when using the HCF cathode (~2.9 V) than when using the TNTs photoanode (~2.5 V) during the discharging

process. In the case of the HCF cathode, the hydrophilicity was increased by changing the ratio of functional groups on the surface through the heat treatment at 500°C,[40, 83] so that ORR activity was improved.[84] In the case of the TNTs photoanode, in order to improve ORR activity, light was irradiated during the discharging process. The cyclic voltammetry (CV) data (Figure 46 (c)) shows that the ORR activity of TNTs was improved under light illumination. In addition, it was confirmed that the discharging voltage was slightly increased under light illumination (~2.50 V) in comparison to the dark state (~2.49 V) (Figure 50). While it is easy and simple to carry out both charging and discharging with one TNTs photoanode in a two-electrode system, there is a limit to improvements in the ORR activity; however, it may be possible to overcome the disadvantages by dividing the charge/discharge part instead of using a conventional two-electrode system.

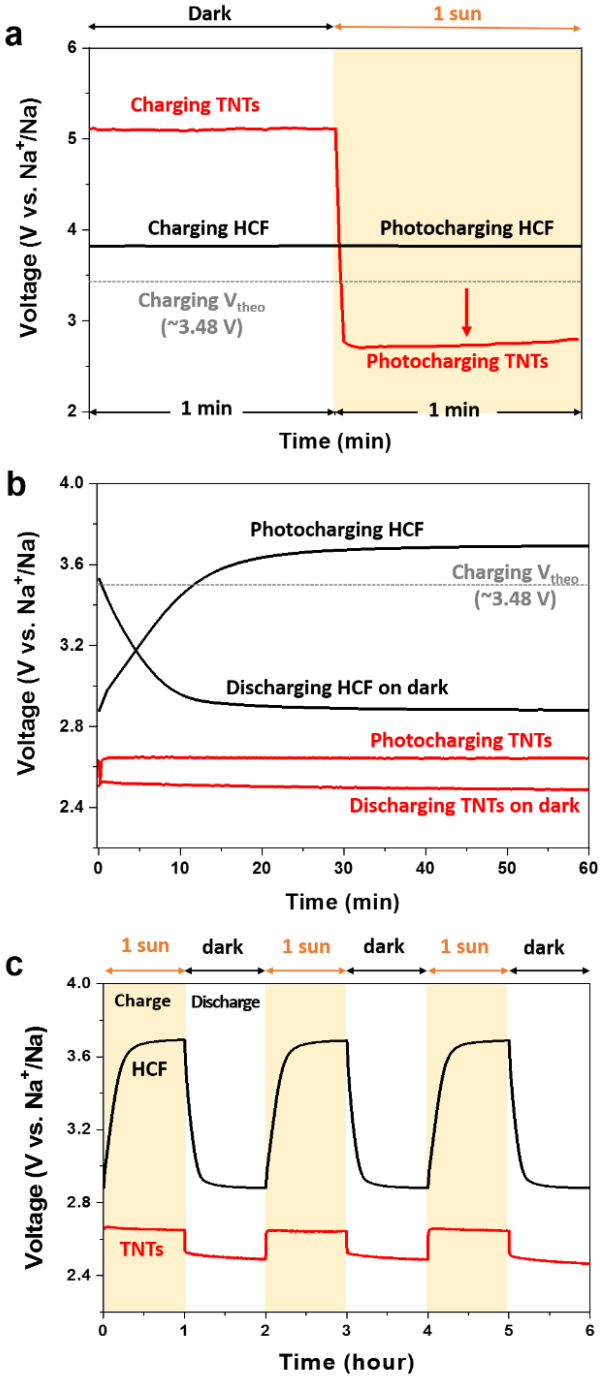

Figure 48. (a) Galvanostatic charging (dark and 1 Sun irradiation) at 0.015 mAcm^{-2} for the TNTs photoanode and HCF cathode, and (b) initial charge and discharge curves for the TNTs photoanode and HCF cathode at 0.015 mAcm^{-2}. (c) Cycle performance of the solar seawater battery with the TNTs photoanode and HCF cathode at a current of 0.015 mAcm^{-2}.

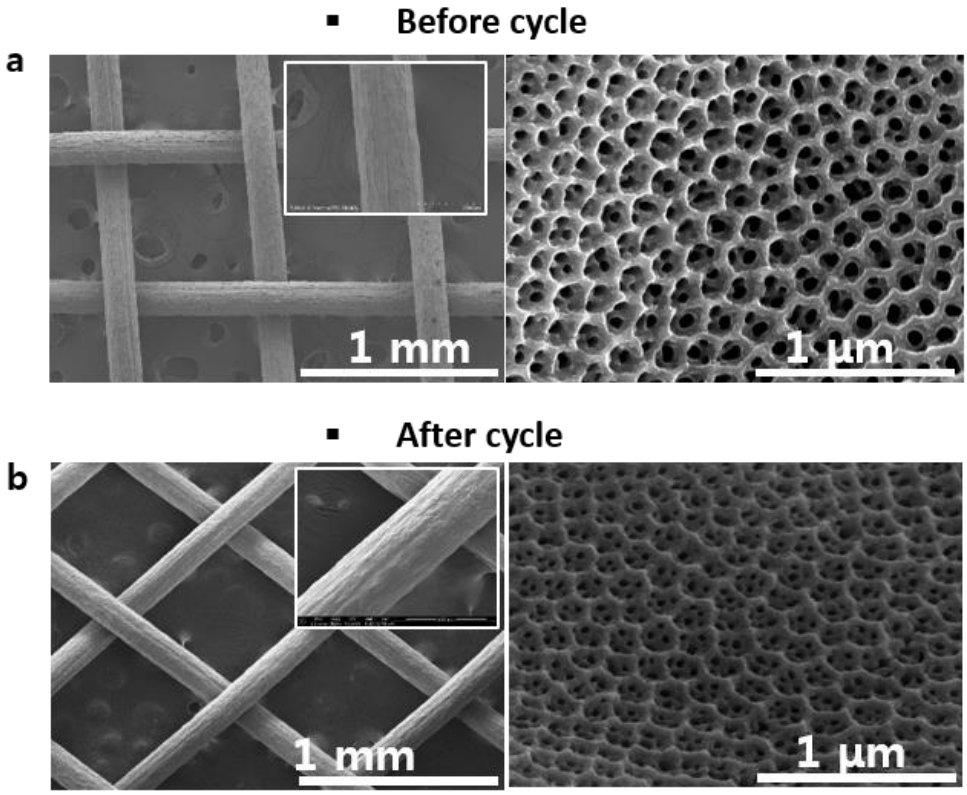

Figure 49. SEM images of TNTs photoanode compared (a) before and (b) after cycles.

Three cycles of photocharging and discharging were performed using TNTs photoanode for 1h at a current density of 0.015 mAcm-2. Figure 49 shows that there is no significant structural and morphological change of TNTs from SEM images before (Figure 49 (a)) and after (Figure 49 (b)) cycles. We confirmed that TNTs photoanode was stable in seawater condition during photocharging and discharging.

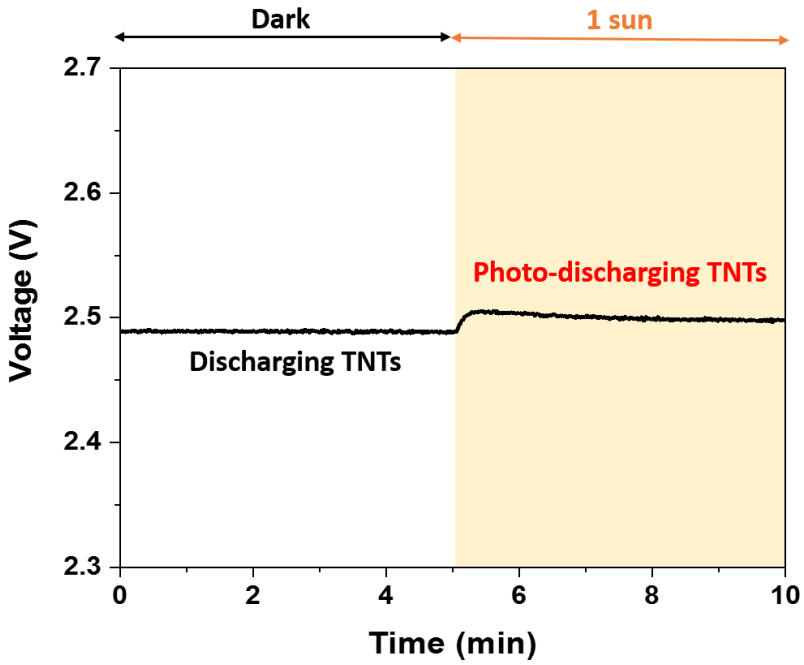

Figure 50. Galvanostatic discharging (dark and 1 sun irradiation) at 0.015 $mAcm^{-2}$ for the TNTs

There was no difference in ORR activity depending on presence or absence of 1 sun irradiation when discharging using HCF cathode current collector. To increase the ORR activity, electrocatalysts such as Pt/C, metal oxide based catalysts should be used.[34] One the other hand, in the case of TNTs, we confirmed that the ORR activity increased during discharge with sun light irradiation (Figure 50). Discharging voltage was ~2.49V in the absence of 1 sun irradiation, but slightly increased to ~ 2 .50 V in the presence of 1 sun irradiation. And also, the CV data in Figure 46 (c) shows the ORR activity of TNTs was increased under light illumination.

Newly designed three-electrode systems can be used to further increase the voltage efficiency dramatically. Figure 51 shows a schematic illustration of a solar seawater battery with a three-electrode system. Charging is performed by using the TNTs photoanode and discharging is performed by using the HCF cathode. In this way, the cell efficiency can be further increased by designing the solar seawater cell by dividing the charge/discharge part (Figure 51). In general, bifunctional catalysts that simultaneously improve the OER and ORR performances are rare. Therefore, it is more efficient to use a photoanode that can lower the charging voltage only in the charging process, and for the discharge process, a material with high ORR activity can be used. If the solar seawater cell is designed by separating the charge/discharge part, various photoanodes beyond TNTs photoanode can be applied. Catalysts such as Pt/C and transition metal oxide-based ones are well known as materials with good ORR characteristics applicable to seawater cells.[34] When the charging part and discharging part were distinguished from each other, the voltage efficiency exceeded 100%. In the case of under illumination, charging was performed at ~2.65 V when using the photoanode, and the discharge voltage was ~2.9 V when using the HCF in the dark state at 0.015 mA cm^{-2} for 1 h (Figure 52). Therefore, the voltage efficiency was ~109%. A charge/discharge cycle test was performed to confirm the cycle stability. When we compared the first cycle and the tenth cycle, we were able to confirm that it operates stably without any significant difference.

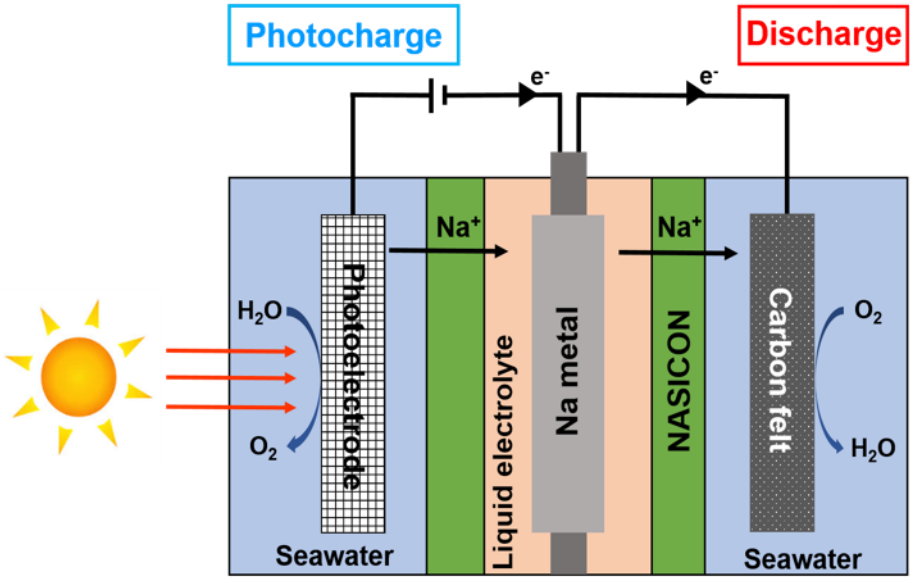

Figure 51. Schematic illustration of the solar seawater battery, in which the information is divided into the photocharge part and discharge part.

Figure 51 shows a schematic illustration of a solar seawater battery with a three-electrode system. Charging is performed by using the TNTs photoanode and discharging is performed by using the HCF cathode. In this way, the cell efficiency can be further increased by designing the solar seawater cell by dividing the charge/discharge part. ~109% voltage efficiency was obtained.

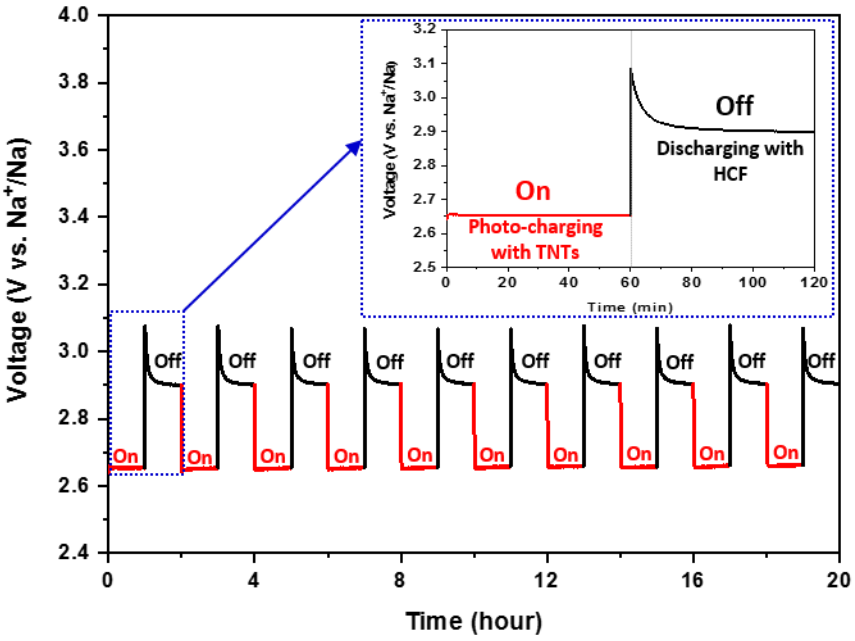

Figure 52. Cycle performance at a current of 0.015 mAcm^{-2}, where the inset shows the galvanostatic initial photocharge and discharge curves; photocharging involved the TNTs photoanode and discharging involved the HCF cathode current collector.

Charging was performed at ~2.65 V when using the photoanode, and the discharge voltage was ~2.9 V when using the HCF in the dark state at 0.015 mA cm^{-2} for 1 h (Figure 52). Figure 52 exhibited higher voltage efficiency (~109%) than the two electrode system. Figure 1 shows a very stable charge and discharge process during 10 cycles at a current of 0.015 mAcm^{-2}.

3.4 Summary

Cell design was implemented by considering the factors affecting the solar seawater battery system. Then, an anatase-TNTs photoanode, which has various advantages among photoelectrodes, was selected as one sample. We performed cell tests by using optimized a solar seawater cell and TNTs photoanode. The results showed that the charging voltage was reduced by ~29% compared to that of the existing HCF cathode. Charging/discharging is possible only with a TNTs photoanode. When the charge/discharge parts are operated separately, the voltage efficiency increased further to ~109%. We also developed a single device that could test the performances of the photoanode and applied it to the solar seawater battery, and subsequently, we were able to significantly reduce the operating voltage of the solar seawater battery by using photoelectrode and solar energy. Further experiments on various candidates for photoelectrodes should be conducted by using the optimized solar seawater cell with other than TNTs photoanode.

Chapter 4

Pb-based composite anodes for sodium-ion and seawater batteries

Anode materials that undergo alloying and conversion type electrochemical reactions are studied as alternative electrodes to graphite and hard carbon with the promise of higher capacities, and potentially higher energy densities. Little studied however are lead (Pb) and lead oxides (PbO, Pb_3O_4) that have advantages of low cost and high volumetric energy density.[138-150] In fact when the Argonne BatPaC model is used with Pb as anode, and layered sodium transition metal oxide cathode are coupled together the energy density for a sodium-ion pouch cell design is 549 Wh/L, and the cost is projected quite low at 63.5 USD/kWh. These metrics are certainly competitive with many grid storage battery systems. However, lead toxicity is a concern. But, Pb has always been one of the most recycled materials in the world, with a high recycling rate close to 99 % in the United States.[71] Certainly, with the rapid in-line progress of lithium- and sodium-ion battery recycling technologies, lead-based materials could become a viable contender for high-energy, low-cost anodes in the future if the performance can be improved and validated.

In this study, we report novel Pb-O-C composite anodes synthesized by simple high energy ball milling process. The electrochemical test data from sodium cells show higher reversible capacity and improved cycle stability when compared to previously reported data of lead and lead oxides materials.[148, 149] The reaction mechanism and effect of composite structure with improved performance are discussed in detail.

4.1 Introduction

The ever-growing demand for electrical energy storage in portable electric devices, electric vehicles (EVs) and large scale energy storage systems (ESSs) necessitates the development of new high-performance and low-cost electrode materials. Compared to the continuing deployments of new generations of cathodes such as $LiCoO_2$, $LiMn_2O_4$, $LiFePO_4$, and $Li(Ni_{1-x-y}Mn_xCo_y)O_2$, carbon-based materials have still been the standard choice of anode since the first commercialization of lithium-ion batteries.[151-166] Recent developments of room-temperature sodium-ion batteries also provide more material options for cathode than for anode. Therefore, exploration of new anode materials is of critical importance for the advancement of lithium- and sodium-ion batteries.

Among many alloying and conversion type materials studied for anode, lead and lead oxides have advantages of low cost and high volumetric energy density. Despite their potential for new anode for lithium- and sodium-ion batteries, the lead-based materials have received little attention mainly because of their toxicity issue. And another problem is poor cyclablility due to large volume change. Large volume change of Pb-based anodes during alloying/dealloying process significantly limits their practical application. The fully sodiated (discharging) phase of Pb, $Na_{15}Pb_4$, has a theoretical capacity fo 485 mAh/g and volumetric capacity is 4365 mAh/cm^3, corresponding to a 365% volume expansion.

However, lead has been one of the most recycled materials with a high global recycling rate close to 99 % in the United States (Figure 53).[147] As such, with the progress of lithium- and sodium-ion battery recycling technologies and by using carbon as a buffer to prevent volume expansion, lead-based materials could become a viable contender for high-energy, low-cost anodes.

In this work, we show novel Pb-O-C composite anodes synthesized by simple high energy ball milling process. The electrochemical data tested in sodium cells show higher reversible capacity and improved cycle stability when compared to previously reported data of lead and lead oxides materials.[139, 149] The reaction mechanism and effect of composite structure in the improved performance were investigated.

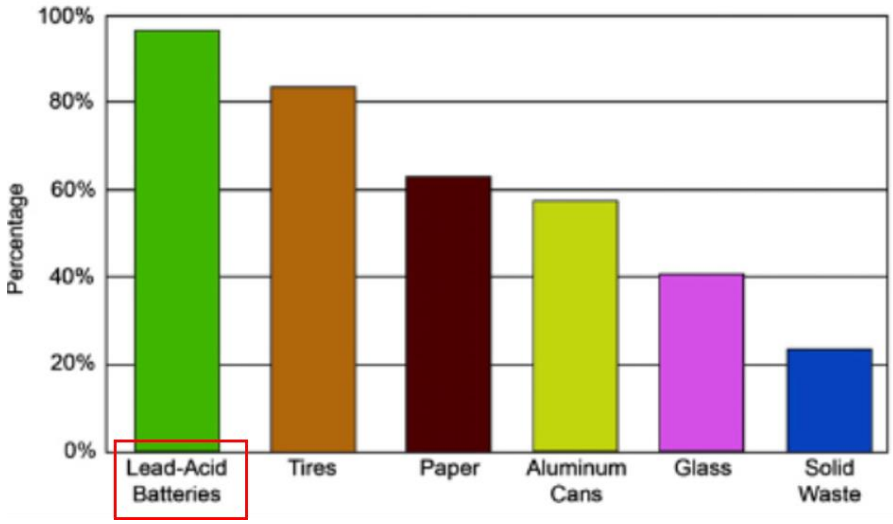

Figure 53. Recycling rate by type of waste.[148]

Figure 53 shows that about 99% of lead-acid batteries are recycled in the United States. Lead-acid batteries have the highest recycling rate than any other recycled product. And Lead-acid battery recycling is also working well in Europe and Japan.

4.2 Experimental detail

4.2.1 Preparation of Pb-based anode

Pb-O-C composites were prepared by high-energy mechanical milling. Lead oxide/super –P carbon (7:3 in weight ratio) was added to a stainless jar and sealed in glove box. PbO and Pb_3O_4 lead oxide (Sigma aldrich) were used (Table 7). The sealed jar was shaken in SPEX 8000M MILL GRINDER for 6 h to completely pulverize the particle and make composites. The Pb-O-C composites electrode consisted of 80 wt% of obtained powder, 10 wt% carbon black, and 10 wt% NMP-soluble binder (polyvinylidene fluoride PVDF, Solvay Solef 5130) laminated on a copper foil current collector and dried 75˚C under vacumme oven for 12 h.

4.2.2 Cell assembly and electrochemical tests

Electrical testing was carried out using coin cell (2032 type) with 1.0 M $NaPF_6$ in PC + 2 wt% FEC (Sigma aldrich) was used as electrolyte at the negative electrode, sodium metal (Sigma aldrich) anode and glass fiber (Whatman) as separator. The cells were assembled in a glove box under a high purity Ar atmosphere (oxygen and water < 1.0 ppm). Electrochemical performance tests were performed using an automatic galvanostatic charge/discharge unit, Maccor battery cycler, in the voltage range of 0.005 – 2 V Na at room temperature at a current density of 100 mA/g.

4.2.3 Characterizations

X-ray diffraction (XRD) was performed with a D/Max, Rigaku apparatus equipped with a Cu-Kα X-ray source (λ =1.5406 Å) and operando high energy x-ray diffraction (HEXRD) was performed in Advanced Photon Center (APS) at Argonne National Laboratory (wave length at 0.108 Å). The surface morphology was observed by scanning electron microscopy (SEM, JEOL JCM-6000 PLUS).

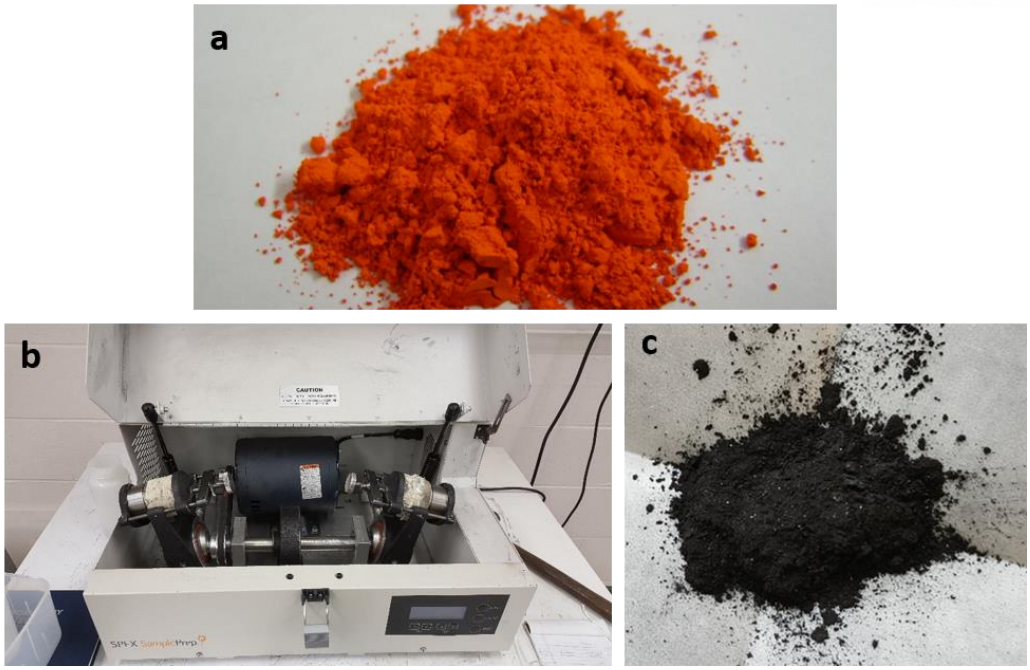

Figure 54. (a) Commercial Pb_3O_4 powder and (b) high energy mechanical milling machine (SPEXMILL) and (c) Pb-O-C composites.

Pb-O-C composites were prepared by high-energy mechanical milling. Lead oxide/super –P carbon was added to a stainless jar and sealed in glove box. PbO and Pb_3O_4 lead oxide (Sigma aldrich) were used. The sealed jar was shaken in SPEX MILL for 6 h to completely pulverize the particle and make composites. The first powder of Pb_3O_4 was orange, but after the high energy ballmill the color changed to black.

Table 7. Sample list of lead and carbon based materials

#	Methode	Compound	Electrode laminate
1	Spexmill	Pb-O-C composite #1 (from PbO)	Active : Carbon : PVDF = 8 : 1 :1
2	Spexmil	Pb-O-C composite #2 (from Pb_3O_4)	Active : Carbon : PVDF = 8 : 1 :1
3	-	Commercial PbO	Active : Carbon : PVDF = 7 : 2 :1
4	-	Commercial Pb_3O_4	Active : Carbon : PVDF = 7 : 2 :1

4.3 Results and discussion

As shown in table xx, we synthesized four samples of lead-based anode materials. Interestingly, XRD patterns of Pb-O-C composite #1 and Pb-O-C composite #2 are shown in Figure 55 and Figure 56, which are consistent with standard values of Pb metal (Fm-3m) except a small peak located at 2Θ = 28 degree. By carful comparison of the small peak with PbO patterns, it is originated from lead oxide (Figure 55). However, after high energy ball mill, both XRD patterns of Pb-O-C composite #1 and Pb-O-C composite #2 closer to the Pb metal (Fm-3m) patterns (Figure 55 and Figure 56). But, the intensity of oxide peaks are different. It is assumed that lead oxide and carbon react with each other at high temperature through the high energy ball milling process and are eventually reduced to Pb metal ($2PbO + C \rightarrow 2Pb\ metal + CO_2\uparrow$). And the broad peaks around 2Θ = 25-30 degree are regarded as peaks by the carbon.

Figure 57 (a) and (b) are SEM images of the commercial PbO pristine and as-synthesized Pb-O-C composite #1 from PbO. It can be seen that the high energy ball mill process has a significant effect on the particle size and morphologies. It can be seen from Figure 57 (b) that the surface of the Pb-O-C composite #1 with large size are rough. The particle size is in a range of several thirties of micrometers. And also, it can be seen from Figure 57 (d) that the surface of the Pb-O-C composite #2 with large size are rough. The particle size is in a range of several tens of micrometers. Totally, the size of Pb-O-C composite #1 particles from five randomly selected regions in digital SEM images was measured, and the size of Pb-O-C composite #1 and Pb-O-C composite #2 are 36μm and 16μm, respectively.

To further investigate microstructure of the Pb-O-C composite particles, TEM and EDS were performed. Figure 58 (a) is EDS images of the microsized Pb-O-C composite #1 particles. It is confirmed that Pb and carbon are evenly distributed through the qualitative EDS analysis. It is assumed that Fe and Co signals possibly from column contamination (Figure 58 (b)). Figure 59 (a-d) are TEM images of the Pb-O-C composite #1 particles. It can be seen Figure 59 (c, d) that the Pb/PbO cluster. Annular Dark Field (ADF) image shows Pb-O-C composite #1 particles on the carbon and it is confirmed that Pb-O-C composite #1 particles (~5 nm) embedded in the carbon (Figure 60 (a, b)). And further high resolution electron energy loss spectroscopy (EELS) analysis can be performed to identify particle composition. Figure 62(a) is EDS images of the microsized Pb-O-C composite #2 particles and qualitative EDS maps show even distribution of Pb and carbon. Pb_3O_4 and Pb cluster also observed in Figure 62 (c, d). The uniform contrast implies that the micro-sized Pb-O-C composite particles are in solid structure.

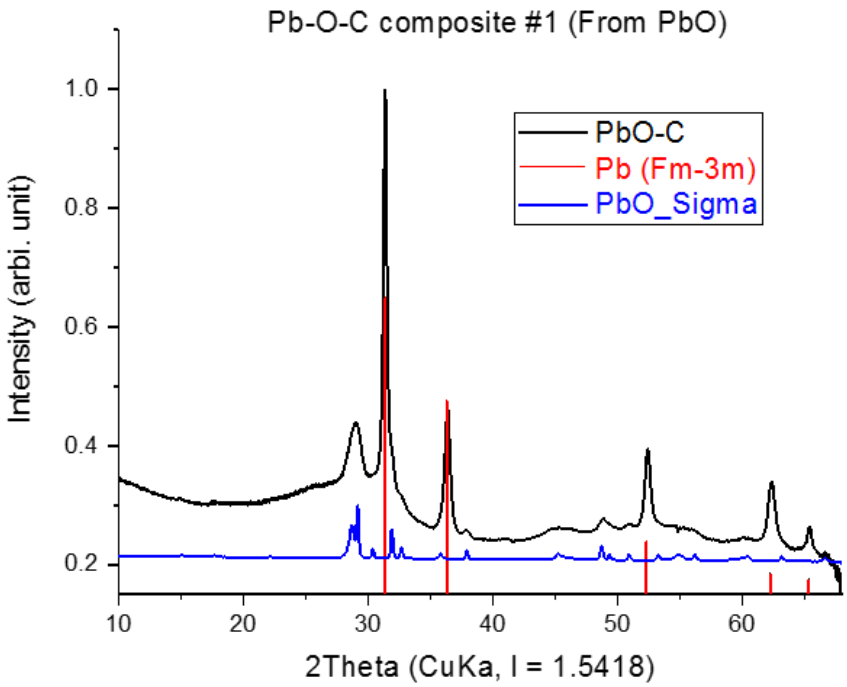

Figure 55. XRD patterns of Pb-O-C composite #1, Pb metal and commercial PbO.

Figure 55 shows that XRD patterns of commercial PbO, Pb metal and Pb-O-C composite #1. Pristine PbO represents a common patterns of lead-oxide. Interestingly, after mixing with PbO with Super-P carbon, it was confirmed that the Pb-O-C composite #1 sample was closer to Pb metal peaks than the lead oxide peaks. However, a little of the lead-oxide peak around 2Θ = 28 degree remains.

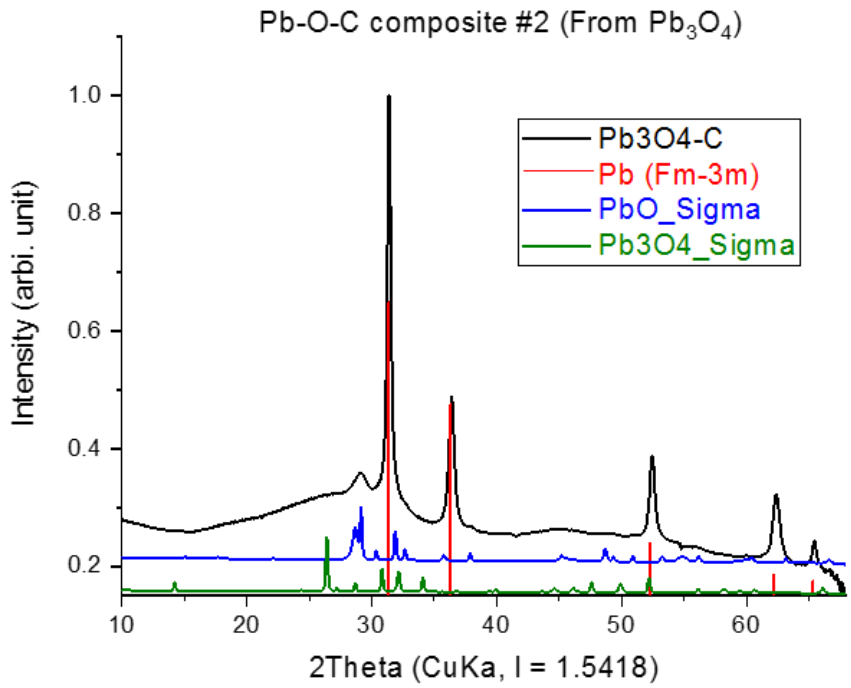

Figure 56. XRD patterns of Pb-O-C composite #2, Pb metal, commercial PbO and Pb_3O_4.

Figure 56 shows that XRD patterns of commercial PbO, Pb_3O_4, Pb metal and Pb-O-C composite #2. Pristine PbO, Pb_3O_4 represent a common patterns of lead-oxide. Similar to the previous XRD patterns in Figure 55, after mixing with Pb_3O_4 with Super-P carbon, it was confirmed that the Pb-O-C composite #2 sample was closer to Pb metal peaks than the Pristine PbO, Pb_3O_4 peaks. There is still an lead oxide peak around $2\Theta = 28$ degrees and the intensity differs from the previous XRD patterns in Figure 55.

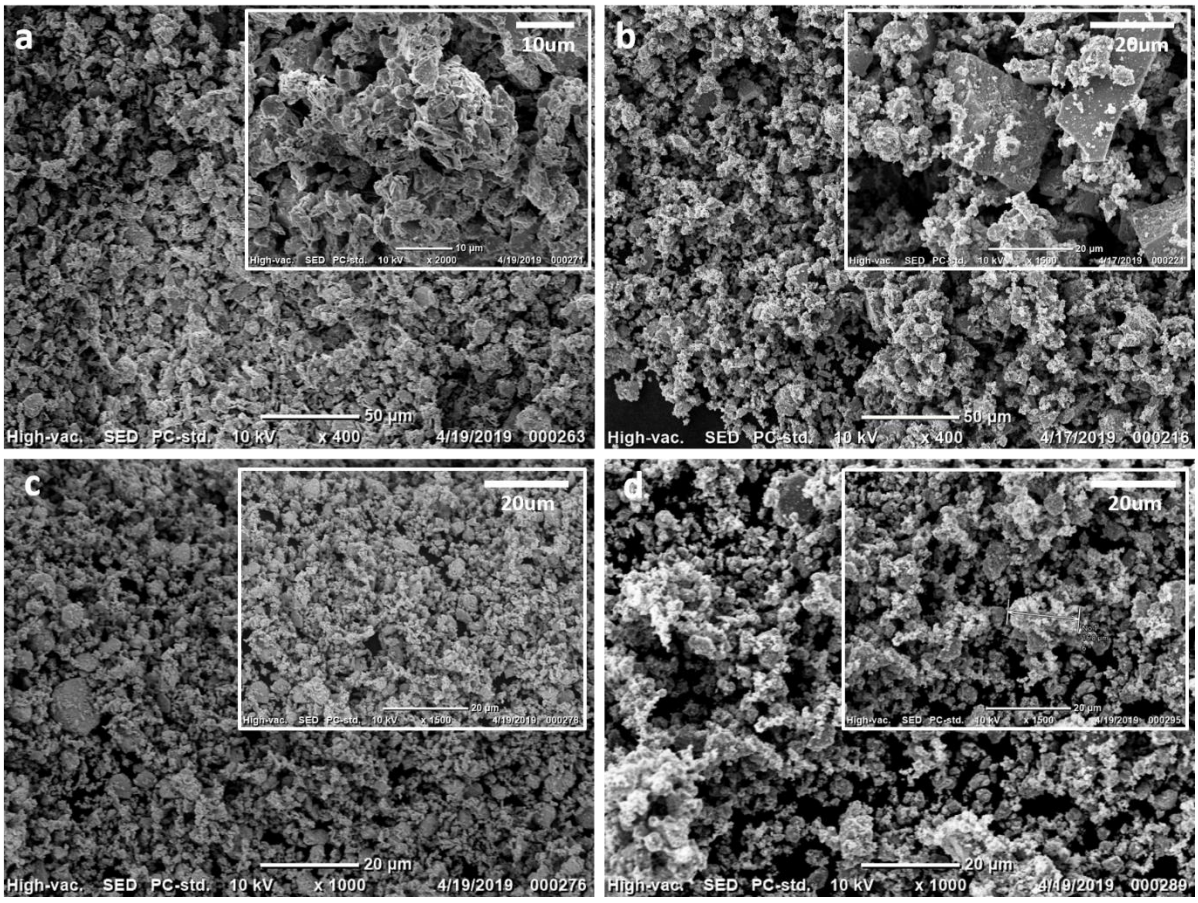

Figure 57. SEM images of commercial PbO (a) and Pb-O-C composite #1 (b).
And SEM images of commercial Pb_3O_4 (c) and Pb-O-C composite #2 (d).

Figure 57 shows SEM images of the commercial PbO (a), Pb_3O_4 (c) pristine and as-synthesized Pb-O-C composite #1 (b) and Pb-O-C composite #2 (d). In both samples in Pb-O-C composite #1 and Pb-O-C composite #2, the morphology and particle size were changed after high-energy ball mill.

In Figure 57 (b) inset in particular, there are rectangular particles, which are assumed to be Pb metal.

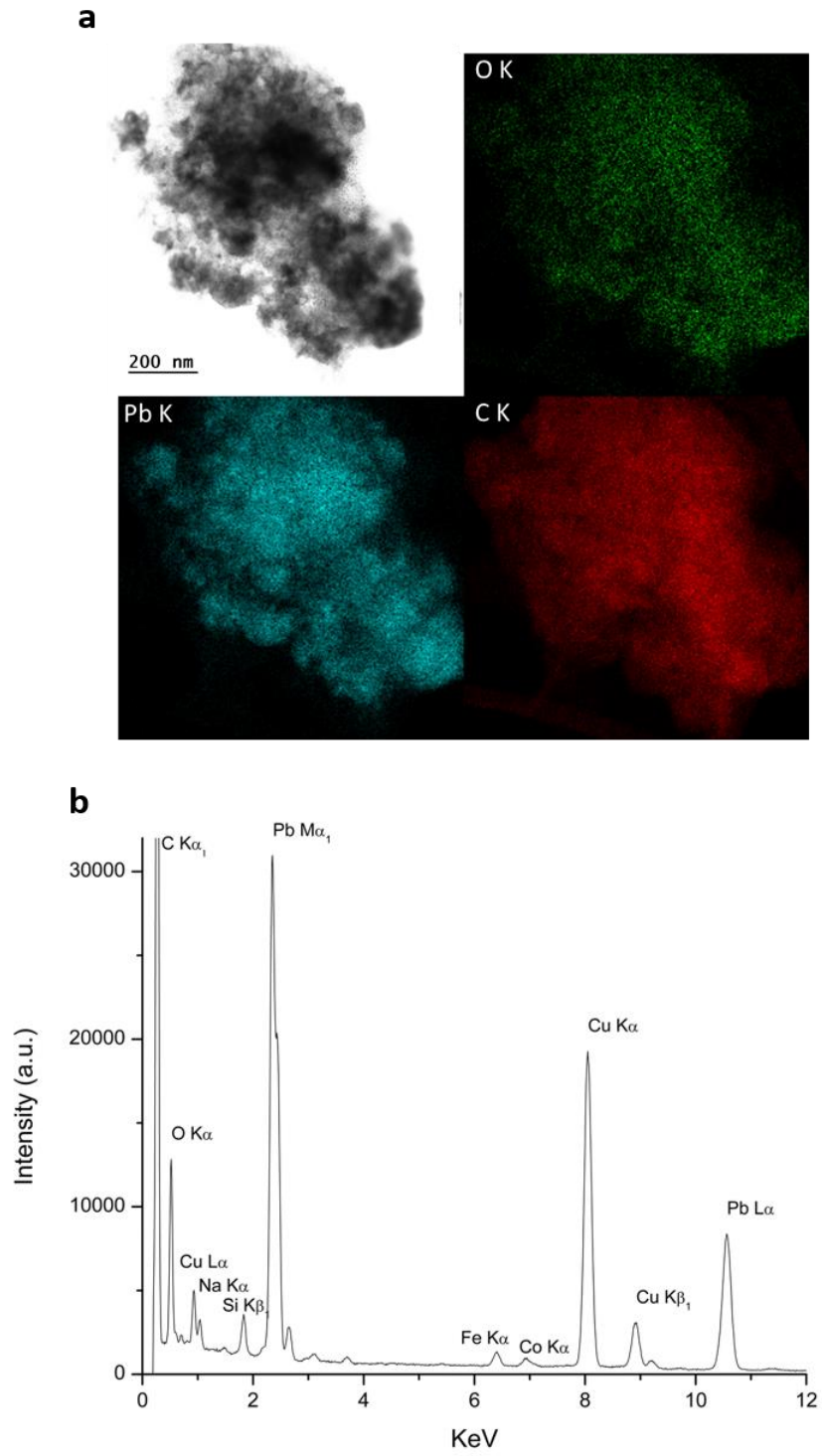

Figure 58. Qulaitative EDS images of Pb-O-C composite #1 (a, b); measured at North Western University.

It can be seen Figure 58 through TEM EDS images, we confirmed that lead (cyan) and carbon (red) are evenly distributed after high-energy ball mill process. Figure 58 (b) shows that lead and carbon are the main components, and Fe/Co signals are expected to be come from column contamination.

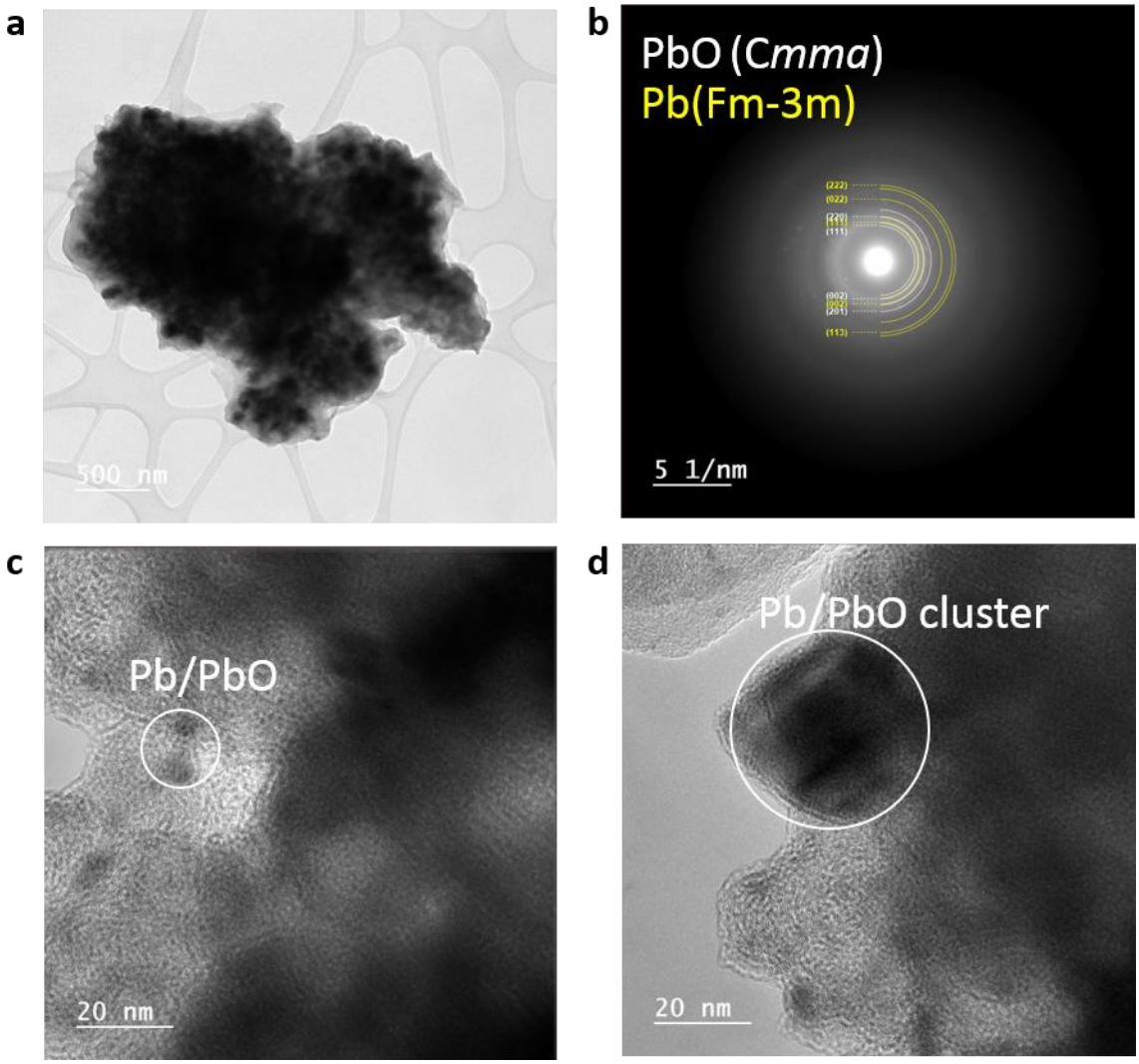

Figure 59. TEM images of Pb-O-C composite #1 particles (a-d). Magnified TEM images of Pb-O-C composite #1 particles showing Pb/PbO clusters (c, d); measured at North Western University.

In Figure 59 (b), TEM SAED ring patterns show that lead oxide and lead metal are in polycrystalline structure. Figure 59 (c) and (d) are the HRTEM images. It can be seen that Pb and PbO are contained in the carbon matrix, and Pb and PbO make cluster.

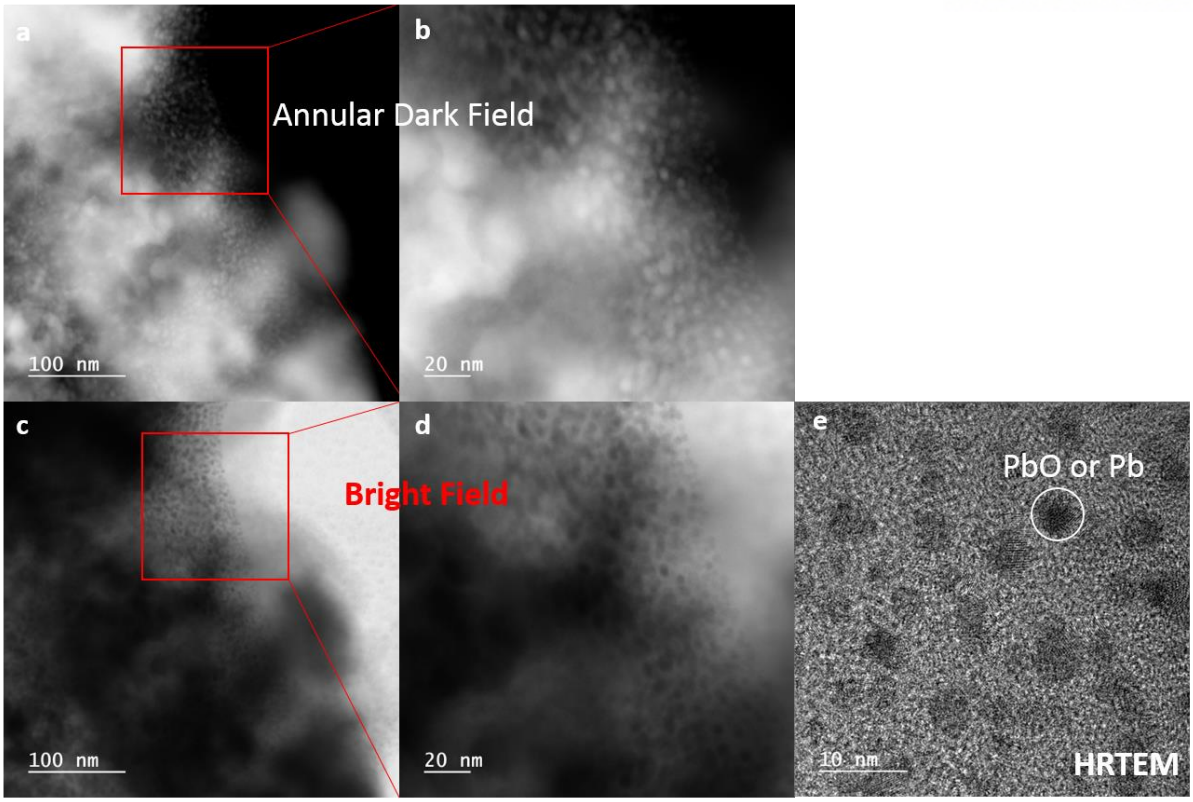

Figure 60. Annular Dark Field (ADF) images show Pb-O-C composite #1 particles on the carbon (a, b). Annular Bright Field (ABF) images show Pb-O-C composite #1 particles on the carbon (c, d). High resolution TEM images show Pb-O-C composite #1 particles on the carbon (e); measured at North Western University.

TEM images of Pb-O-C composite #1 particles have been observed by the annular bright field (ABF) and annular dark field (ADF) imaging using an aberration-corrected scanning transmission electron microscope. PbO or Pb particles of ~5nm embedded in the carbon and further EELS analysis is needed to identify particle composition.

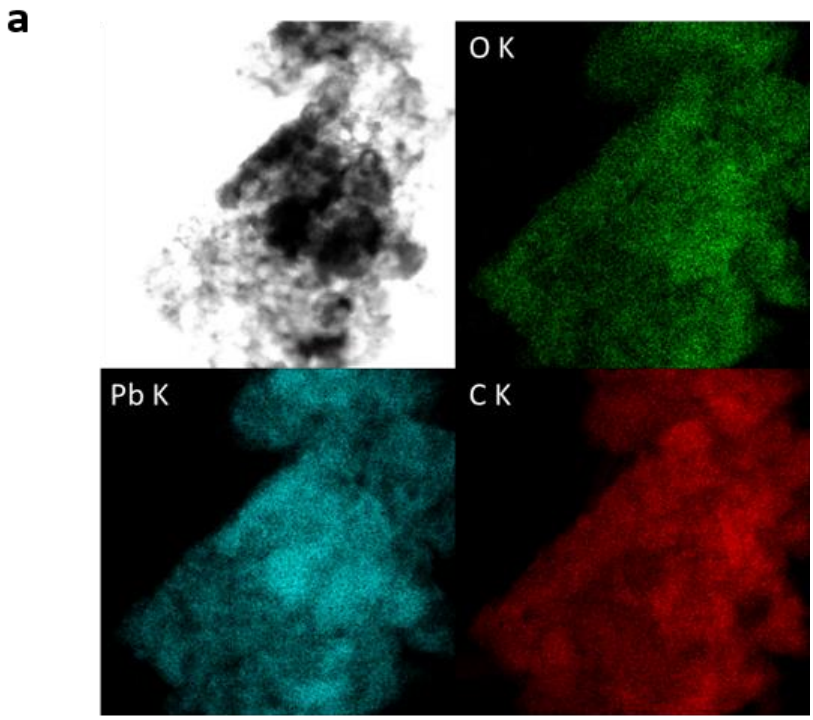

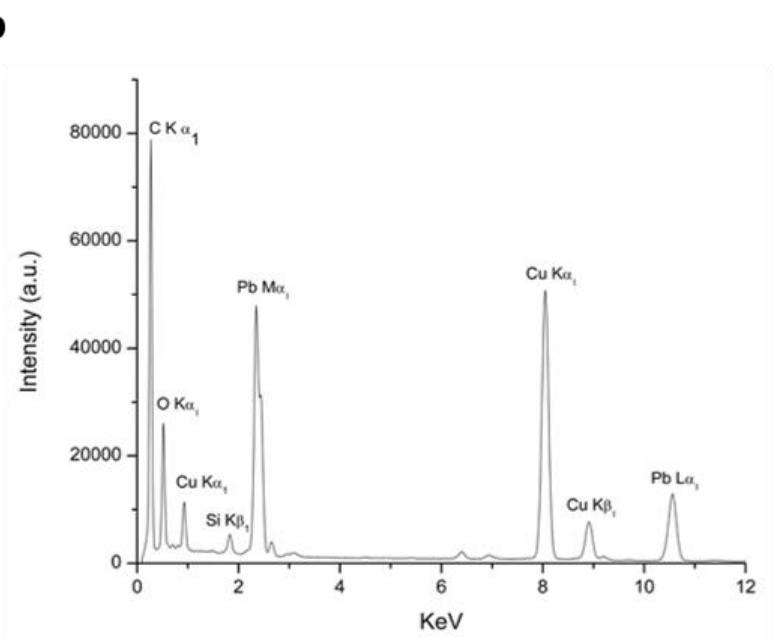

Figure 61. Qulaitative EDS images of Pb-O-C composite #2 (a, b) ; measured at North Western University.

It can be seen Figure 61 through TEM EDS images, we confirmed that lead (cyan) and carbon (red) are evenly distributed after high-energy ball mill process. Figure 61 (b) shows that lead and carbon are the main components.

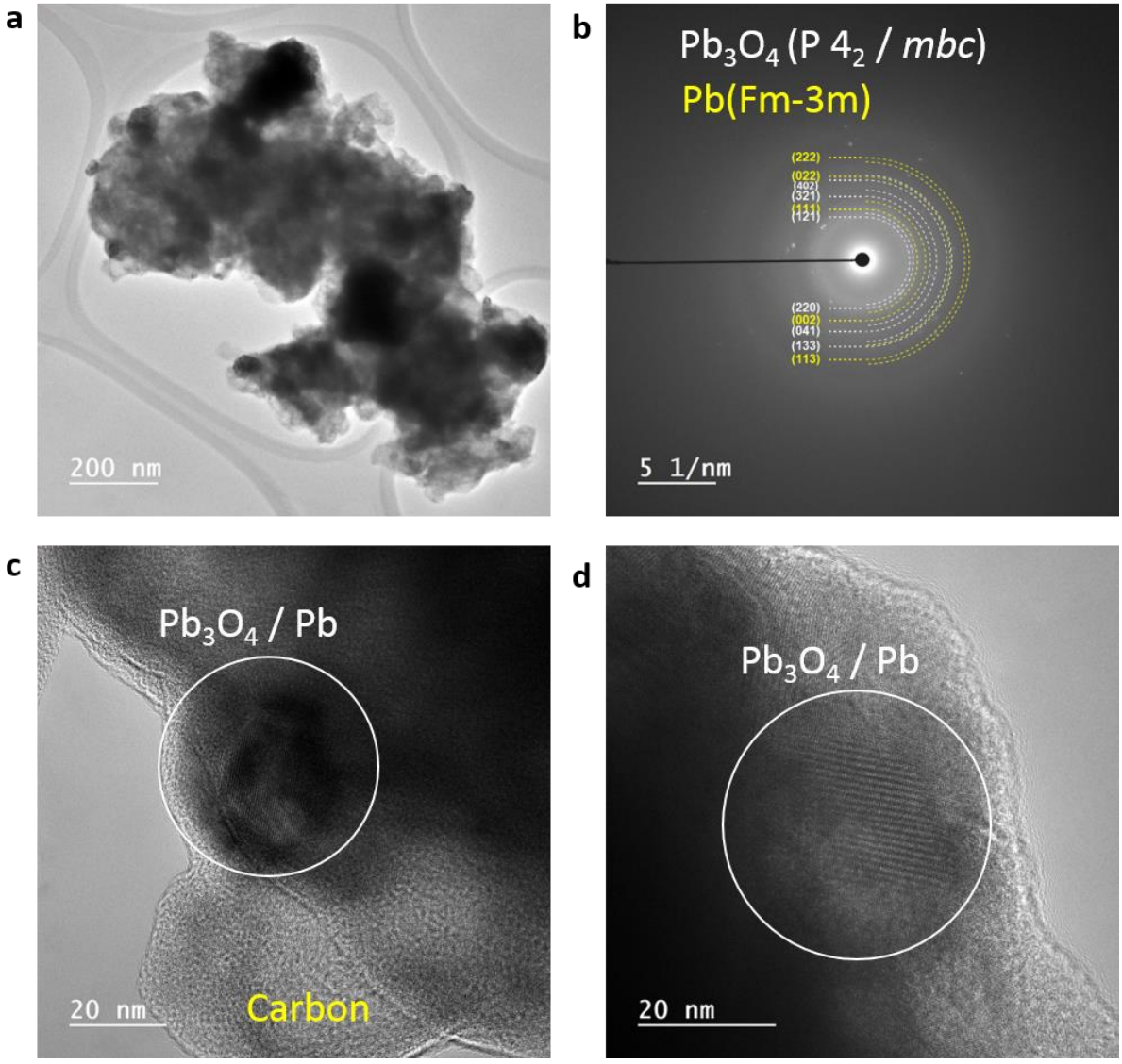

Figure 62. TEM images of Pb-O-C composite #2 particles (a-d). Magnified TEM images of Pb-O-C composite #2 particles showing Pb or Pb_3O_4 (c, d); measured at North Western University.

Figure 62 (b), TEM SAED ring patterns show that Pb_3O_4 and Pb metal are in polycrystalline structure. Figure 62 (c) and (d) are the HRTEM images. It confirmed that the crystallinity of Pb_3O_4 /Pb and carbon envelops Pb/Pb_3O_4 particles well and can be attributed to the good cycle stability.

Figure 63 (a) and (b) exhibit voltage profiles of the first and second cycles of the commercial PbO and Pb_3O_4, respectively. Both samples show similar voltage profiles and Differential capacity plots (dQ/dV). The cycling performance at a rate of 100 mA/g for 100 cycles. During the first discharge of the commercial PbO particles, as shown in Figure 63, the voltage decrease sharply to 0.5 V, and then followed by a small slope. When the voltage continues to decrease to 0.2 V, obvious plateau appears, which delivers ~350 mAh/g of specific capacity and then followed by a gradual voltage decrease to the cut-off value. Both the commercial PbO and Pb_3O_4 showed poor cycle stability during 100 cycles (Figure 65).

On the other hand, interestingly, the Pb-O-C composite #1 and Pb-O-C composite #2 exhibited very stable cyclability (Figure 64). In addition, there is a distinct initial voltage profiles differences between lead oxide particles and Pb-O-C composite particles (Figure 64). One big difference is that there is no long voltage plateau in the first discharge curve of the Pb-O-C composite particles, which indicates that lead oxide is reduced Pb metal during high energy ball mill process. The initial voltage profiles of Pb-O-C composite particles are consistent with that of the Pb metal anode. There are five peaks in the dQ/dV plots. The peaks of 1.1 V, 0.5 V, 0.33 V, 0.15 V and 0.1 V can be found in order of dQ/dV curves. During discharging, electrolyte decomposition occurs at the metal surface in ~1.1 V. When we compared with voltage profile and Na-Pb binary phase diagram, the second plateau during sodiation terminates at a composition that roughly corresponds to $NaPb_3$. Third plateau occurs with the end composition corresponding to NaPb. The next plateau is roughly correlated with Na_9Pb_4. Final plateau with the end composition close to $Na_{15}Pb_4$. During charging (desodiation), the reverse reaction occurs. In summary, the process for the discharge (sodiation) of Pb-O-C composite mechanism is as follows;

$$Pb \rightarrow NaPb_3 \rightarrow NaPb \rightarrow Na_9Pb_4 \rightarrow Na_{15}Pb_4$$

This process is completely reversible during the subsequent charging (desodiation) as the same phases are observed to reform.

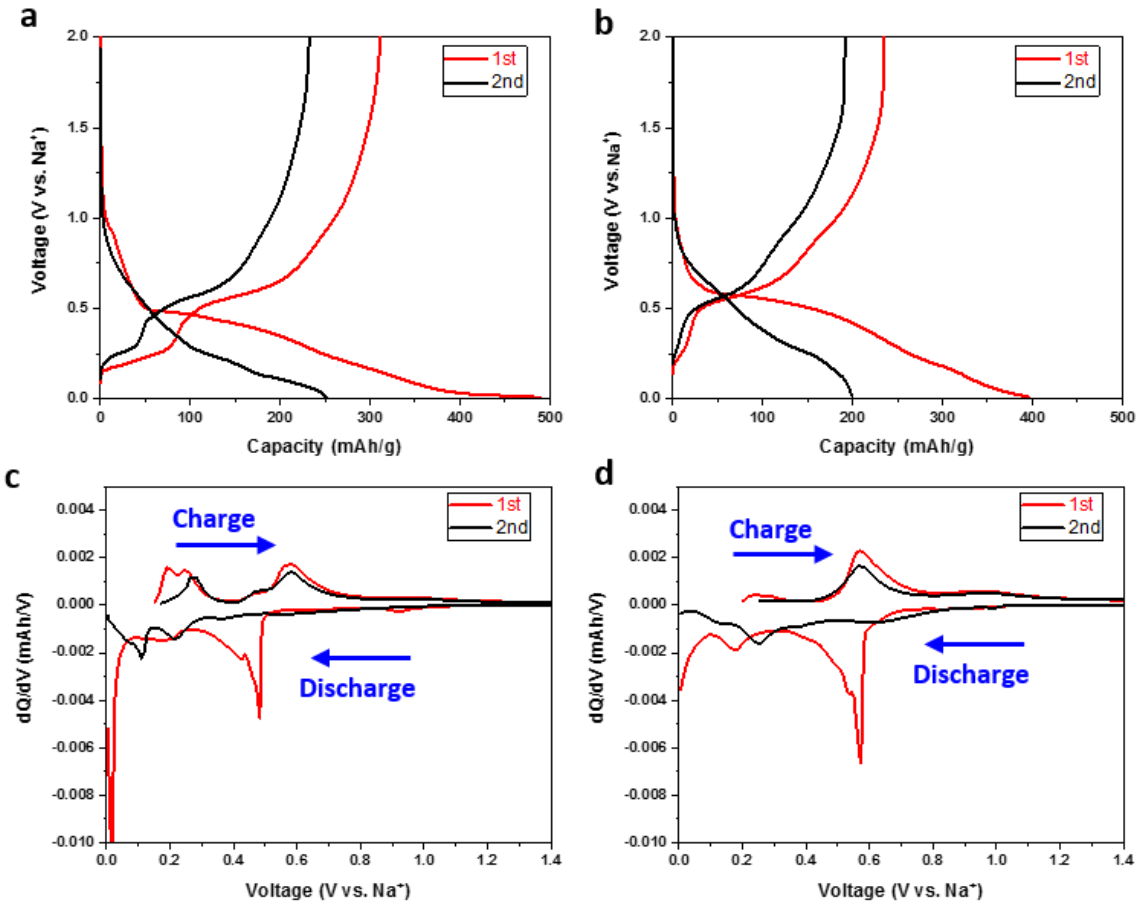

Figure 63. Initial and second voltage profiles of commercial PbO (a) and Pb_3O_4 (b). Differential capacity plots (dQ/dV) of the commercial PbO (c) and Pb_3O_4 (d).

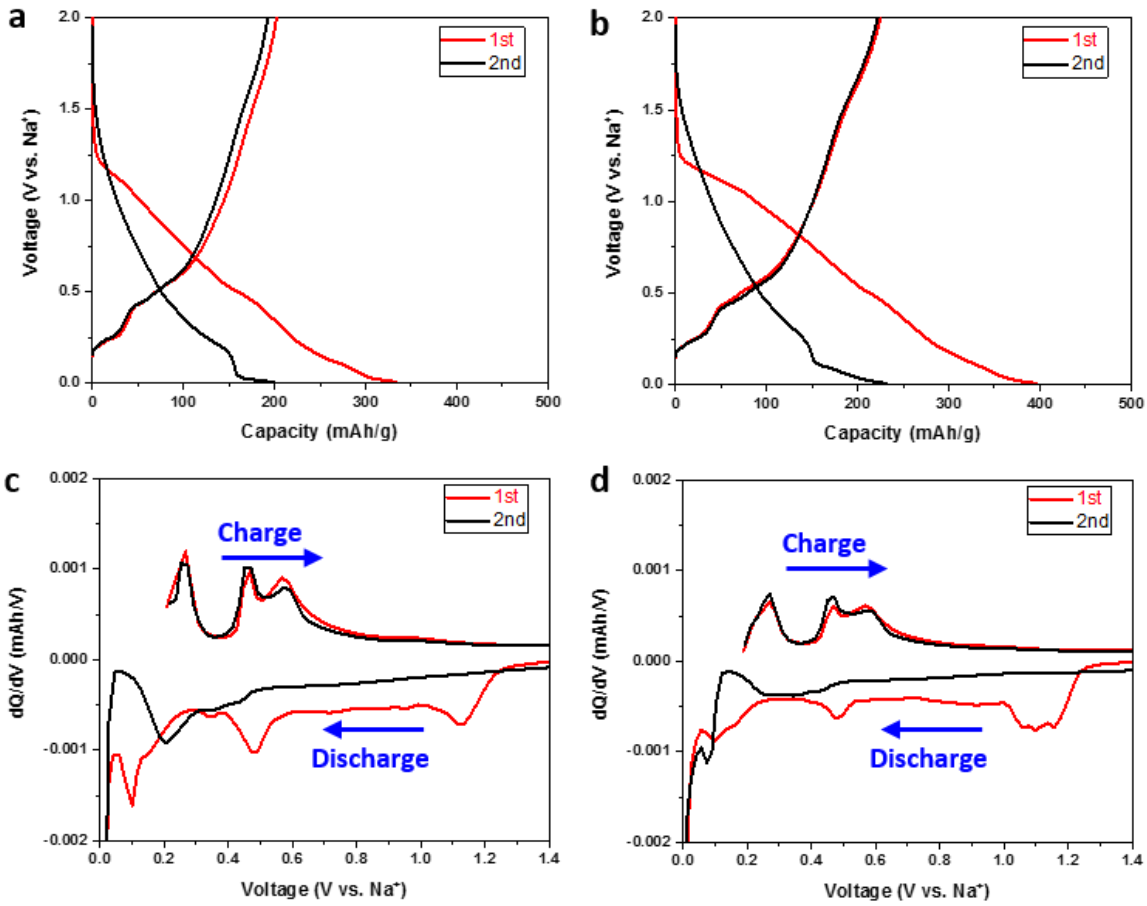

Figure 64. Initial and second voltage profiles of Pb-O-C composite #1 (a) and Pb-O-C composite #2 (b). Differential capacity plots (dQ/dV) of the Pb-O-C composite #1 (c) and Pb-O-C composite #2 (d).

The discharge capacity cycling performance of the commercial lead oxides and Pb-O-C composites is compared and presented in Figure 65. It can be seen that the discharge capacity of the commercial lead oxide (PbO, Pb_3O_4) particles decrease sharply from initial discharge capacity of ~400 mAh/g to the 40th cycle of ~ 0 mAh/g. Interestingly, Pb-O-C composites particles exhibit very stable capacity-cycling behavior especially in Pb-O-C composites #2 during 100 cycles. The initial discharge capacity is 425 mAh/g and capacity can be maintained over 50 cycles at current rate of 100 mA/g. The initial coulombic efficiencies of the Pb-O-C composites #1 and #2 are 97% and 98%, respectively. It is believed that the good reversible capacity retention and coulombic efficiencies of the Pb-O-C composites #1 and #2 are due to the carbon effect. Typically, the problem of lead based materials is volume expansion. The fully sodiated phase of Pb, $Na_{15}Pb_4$, has a theoretical volumetric capacity is 4365 mAh/cm3, corresponding to a 365% volume expansion. Therefore, due to the volume expansion problem during sodiation and desodiation, anode materials are detached from the current collector and finally shows poor cycle stability.

However, Pb-O-C composites anodes exhibited improved cycle stability compared to previously reported data [Table 8]. It is believed that carbon plays a role in preventing large volume changes and helps enhance capacity retention.

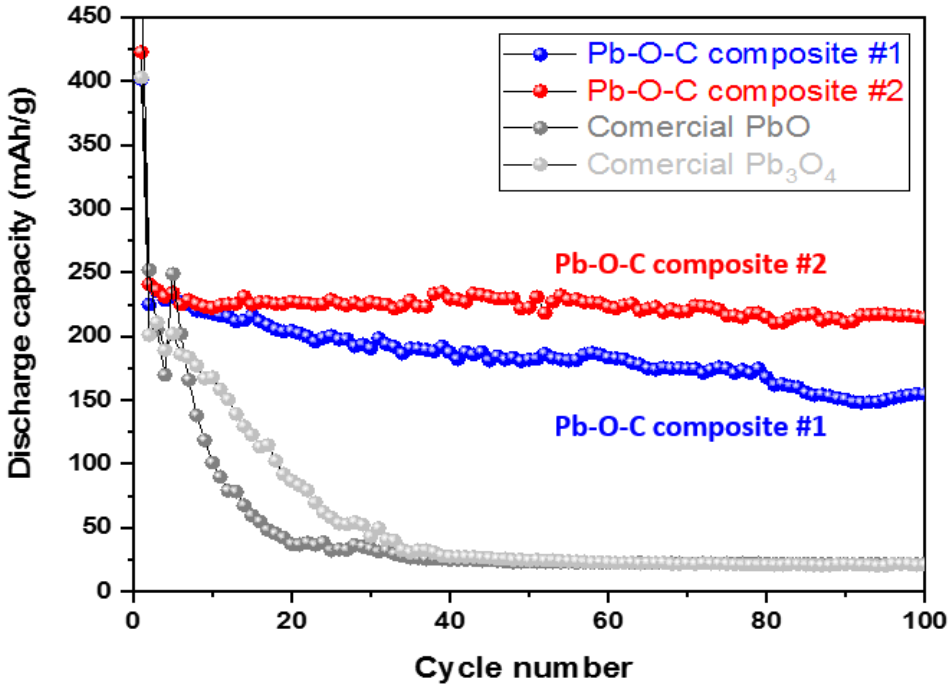

Figure 65. Discharge capacity vs. cycle number for Pb-O-C composite #1 (a) and Pb-O-C composite #2 (b) electrodes in half-cells at a current rate of 100 mA/g.

Table 8. Literature survey of lead-based anodes for SIBs

#	Title	Year	Author	Main points	Performance
1	The role of conductive polymers in Alkali-metal secondary electrodes (JES)	1987	T. R. Jow and D. Vernick	1) Discharging mechanism 2) Potentials of Na/Pb cell	3 cycles
2	Challenges for Na-ion negative electrodes (JES)	2011	Ceder	1) Volume expansion 2) Volumetric energy density	N/A
3	In Situ XRD study of Silicon, Lead and Bismuth Negative Electrodes in Nonaqueous Sodium Cells (ECS)	2014	M. N. Obrovac	1) Initial voltage curve of Na/Pb cell 2) In-situ XRD measurement	20 cycles ~150 mAh/g

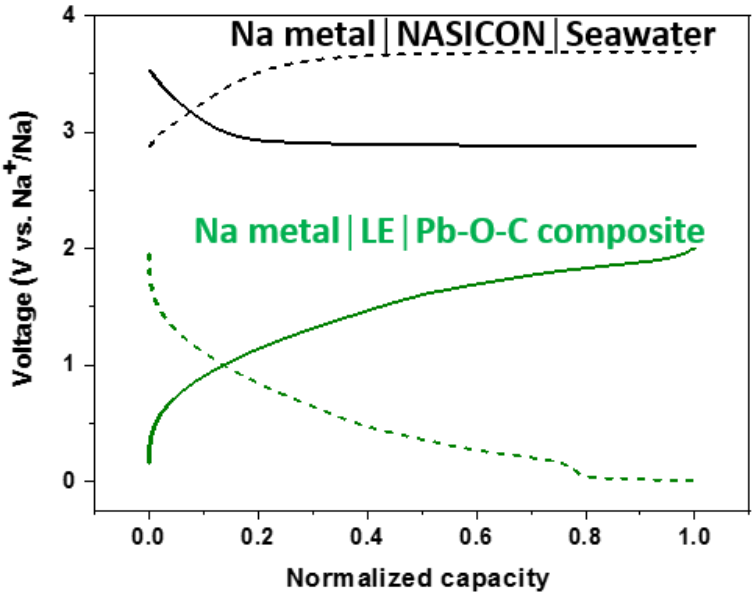

Figure 66. Charge-discharge profiles of the seawater cell (cathode half-cell; top) and Na-ion half-cell (anode half-cell; bottom) with respect to normalized capacity.

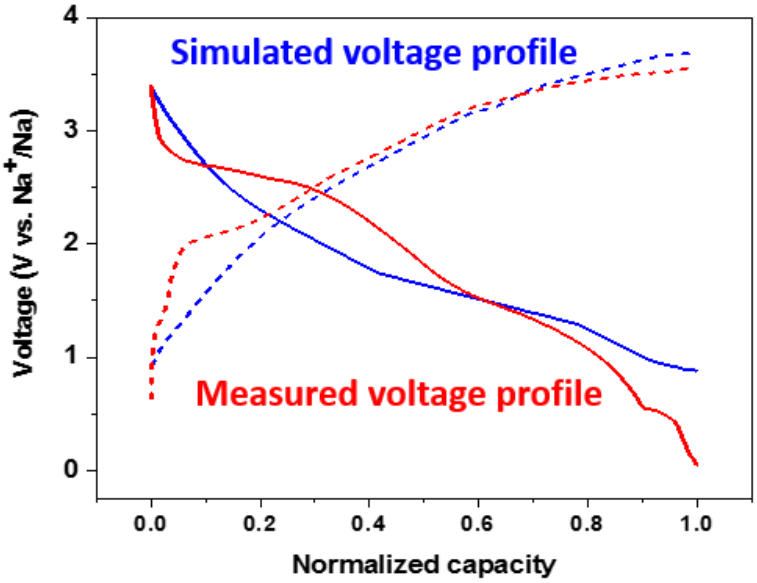

Figure 67. Simulated and measured second charge-discharge voltage profiles of the seawater cell using Pb-O-C composite anode.

Figure 66 shows that the charge-discharge voltage profiles of the seawater cell with a Na metal anode (cathode half-cell; top) and the 2032 half-cell with the Pb-O-C composite electrode (anode half-cell; bottom) at the second cycle. In the case of the cathode half-cell (Na meal | seawater), charging was done at a rate of ~ 3.8 V vs Na^+/Na while discharging was performed at ~ 2.9 V vs Na^+/Na at a current rate density of 0.025 mA/cm^2. The anode half-cell (Na meal | Pb-O-C composite #1) exhibited a sodiation potential of ~ 0.5 V vs. Na^+/Na and a desodiation potential of ~ 1.5 V vs. Na^+/Na. Based on the voltage profiles of both half-cells, a simulated voltage profile for the seawater full-cell with the Pb-O-C composite #1 anode is plotted in Figure 67. The average charge and discharge voltages for the full-cell were estimated to be ~2.7 V and ~1.7 V, respectively at the second cycle.

Figure 68 shows that the voltage profiles of the full-cell, cycled with a capacity cut-off at 300 $mAh/g_{composite}$ at charging and a voltage cut-off at 0.005 V at discharging. The discharge capacity in the first cycle was about 180 $mAh/g_{composite}$, while the discharge capacity increased to over 225 $mAh/g_{composite}$. Although the cycle stability to date are good, the cycle stability of the full-cell should be further observed.

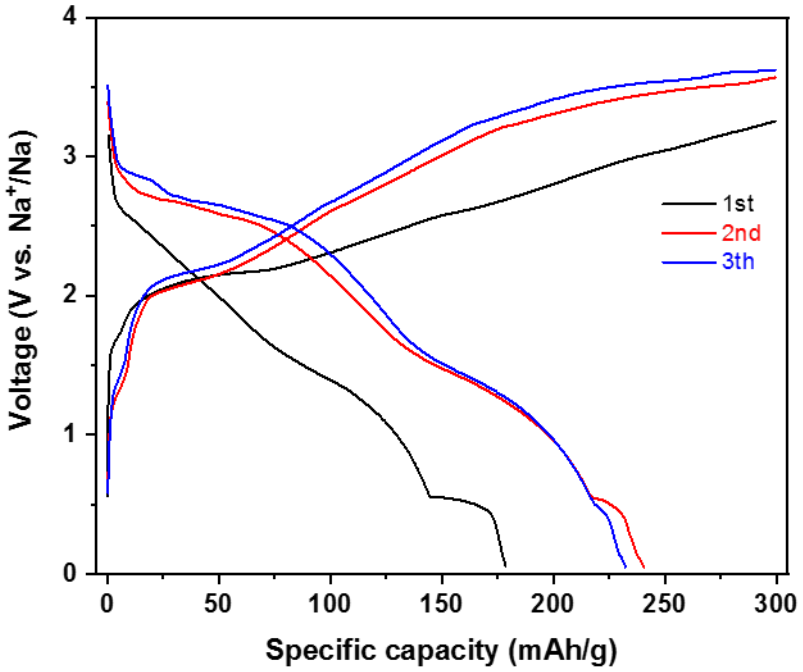

Figure 68. Charge-discharge voltage profiles of the seawater full-cell with the Pb-O-C composite #1 anode.

4.4 Summary

New Pb-O-C composite anodes were synthesized by simple high energy ball milling process. HEXRD analysis indicated that the Pb-O-C composites were reduced Pb metal during high energy ball mill. The PbO and Pb_3O_4 particles exhibited gradual capacity fading with initial discharge capacity of ~ 400 mAh/g. On the other hand, the Pb-O-C composites particles displayed very stable discharge capacity-cycling behavior with discharge capacity of ~220 mAh/g at the 100^{th} cycle in sodium ion battery. The capacity retention was as high as 99% over 100 cycles. The good cycling performance and high capacity retention of the Pb-O-C composites are due to carbon effect. Carbon is an effective method to enhance the capacity retention of Pb-based anodes by role as a buffer. Also, when the Pb-O-C composite #1 anode of the seawater full-cell was applied, the discharge capacity was over 225 $mAh/g_{composite}$. It is hoped that the knowledge gained from such fundamental studies will aid in the future design of practical sodium-ion and seawater batteries anodes.

5. Overall summary

As increasing demands for renewable energy sources, the developments of large-scale energy storage systems (ESSs) are essential for load leveling and peak shaving. Among the various ESSs, lithium-ion batteries are considered as one of the mature technologies. However, their long-term sustainable use may be limited because of the steeply rising prices of Li, Co-containing raw materials and anode materials due to the increasing demand for LIBs in electric vehicles and large-scale ESSs.

In chapter 2, we introduced a new battery system that does not affected by the price of cathode materials. The key elements in seawater batteries, a coin-type cell, a flow-cell tester, and their key compartments were designed and fabricated by trial and error and the testing environment was also determined. We examined the wettability of seawater on the carbon felt cathode current collector and its effect on the charge-discharge cycling performance. We also showed that the flow of the seawater catholyte reduced ΔV (~0.7 V) by 36% from ~1.1 V under no flow state. After normalizing the cell design and testing conditions, a comparative test was performed to identify the key elements for improving cell performance. Finally, the battery performance was improved by using electrocatalysts materials in cathode. Through this process, we were able to optimize the coin-type seawater batteries.

The problem of seawater batteries is the low voltage efficiency due to the sluggish kinetic of oxygen evolution reactions (OER) and oxygen reduction reactions (ORR). In Chapter 3, we demonstrated an efficient photoelectrochemical-assisted rechargeable seawater battery. Cell design was implemented by considering the factors affecting the solar seawater battery system. Then, an anatase-TNTs photoanode, which has various advantages among photoelectrodes, was selected as one sample. We performed cell tests by using optimized a solar seawater cell and TNTs photoanode. The results showed that the charging voltage was reduced by ~29% compared to that of the existing HCF cathode. Charging/discharging is possible only with a TNTs photoanode. When the charge/discharge parts are operated separately, the voltage efficiency increased further to ~109%. We also developed a single device that could test the performances of the photoanode and applied it to the solar seawater battery, and subsequently, we were able to significantly reduce the operating voltage of the solar seawater battery by using photoelectrode and solar energy. Further experiments on various candidates for photoelectrodes should be conducted by using the optimized solar seawater cell with other than TNTs photoanode.

In chapter 4, new Pb-O-C composite anodes were synthesized for SIBs and seawater batteries by simple high energy ball milling process. HEXRD analysis indicated that the Pb-O-C composites were reduced Pb metal during high energy ball mill. The Pb-O-C composites particles displayed very stable discharge capacity-cycling behavior with discharge capacity of ~220 mAh/g at the 100^{th} cycle. The capacity retention was as high as 99% over 100 cycles. The good cycling performance and high capacity

retention of the Pb-O-C composites are due to carbon effect. Carbon is an effective method to enhance the capacity retention of Pb-based anodes by role as a buffer. Furthermore, when the Pb-O-C composite #1 anode of the seawater full-cell was applied, the discharge capacity was over 225 $mAh/g_{composite}$. As a result, we were able to obtain anode materials with low-cost and high performance.

In the thesis, I designed coin-type seawater battery, solar seawater battery system and developed new Pb-based anode materials. I hope that this thesis will provide clear guidance in the new cell design and understanding of seawater batteries. Studies of this novel solar seawater battery are in the early stage and further design and performance improvements are under development. However, I expect it to have global application for large-scale energy storage systems (ESSs) in the near future.

References

1. Panwar, N. L.; Kaushik, S. C.; Kothari, S., Role of renewable energy sources in environmental protection: A review. *Renew. Sustain. Energy Rev* **2011,** *15* (3), 1513-1524.

2. Liu, Z.; Guan, D.; Wei, W.; Davis, S. J.; Ciais, P.; Bai, J.; Peng, S.; Zhang, Q.; Hubacek, K.; Marland, G., Reduced carbon emission estimates from fossil fuel combustion and cement production in China. *Nat.* **2015,** *524* (7565), 335.

3. Sims, R. E.; Rogner, H.-H.; Gregory, K., Carbon emission and mitigation cost comparisons between fossil fuel, nuclear and renewable energy resources for electricity generation. *Energy policy* **2003,** *31* (13), 1315-1326.

4. Zhang, N.; Zhou, P.; Choi, Y., Energy efficiency, CO_2 emission performance and technology gaps in fossil fuel electricity generation in Korea: A meta-frontier non-radial directional distance functionanalysis. *Energy Policy* **2013,** *56*, 653-662.

5. Boyle, G., Renewable energy. *Renewable Energy* **2004**, 456.

6. Nelson, V.; Starcher, K., *Wind energy: renewable energy and the environment*. CRC press: **2018**.

7. Teleke, S.; Baran, M. E.; Bhattacharya, S.; Huang, A. Q., Rule-based control of battery energy storage for dispatching intermittent renewable sources. *IEEE Transactions on Sustainable Energy* **2010,** *1* (3), 117-124.

8. Bull, S. R., Renewable energy today and tomorrow. *Proceedings of the IEEE* **2001,** *89* (8), 1216-1226.

9. Şen, Z., *Solar energy fundamentals and modeling techniques: atmosphere, environment, climate change and renewable energy*. Springer: **2008**.

10. Divya, K.; Østergaard, J., Battery energy storage technology for power systems—An overview. *Electric power systems research* **2009,** *79* (4), 511-520.

11. Dunn, B.; Kamath, H.; Tarascon, J.-M., Electrical energy storage for the grid: a battery of choices. *Science* **2011,** *334* (6058), 928-935.

12. Larcher, D.; Tarascon, J.-M., Towards greener and more sustainable batteries for electrical energy

storage. *Nat. Chem.* **2015,** *7* (1), 19.

13. Scrosati, B.; Hassoun, J.; Sun, Y.-K., Lithium-ion batteries. A look into the future. *Energy Environ. Sci.* **2011,** *4* (9), 3287-3295.

14. Diouf, B.; Pode, R., Potential of lithium-ion batteries in renewable energy. *Renewable Energy* **2015,** *76*, 375-380.

15. Nair, N.-K. C.; Garimella, N. J. E., Battery energy storage systems: Assessment for small-scale renewable energy integration. *Energy Buildings* **2010,** *42* (11), 2124-2130.

16. Goodenough, J. B.; Park, K. S., The Li-ion rechargeable battery: a perspective. *J. Am. Chem. Soc.* **2013,** *135* (4), 1167-76.

17. Nishi, Y., Lithium ion secondary batteries; past 10 years and the future. *J. Power Sources* **2001,** *100* (1-2), 101-106.

18. Etacheri, V.; Marom, R.; Elazari, R.; Salitra, G.; Aurbach, D., Challenges in the development of advanced Li-ion batteries: a review. *Energy Environ. Sci.* **2011,** *4* (9).

19. Armand, M.; Tarascon, J.-M., Building better batteries. *Nat.* **2008,** *451* (7179), 652.

20. Wu, Y.-P.; Rahm, E.; Holze, R., Carbon anode materials for lithium ion batteries. *J. Power Sources* **2003,** *114* (2), 228-236.

21. Ozawa, K., Lithium-ion rechargeable batteries with $LiCoO_2$ and carbon electrodes: the $LiCoO_2$/C system. *Solid State Ion.* **1994,** *69* (3-4), 212-221.

22. Kannan, A. M.; Rabenberg, L.; Manthiram, A., High capacity surface-modified $LiCoO_2$ cathodes for lithium-ion batteries. *Electrochem. Solid-State Lett.* **2003,** *6* (1), A16-A18.

23. Blurton, K. F.; Sammells, A. F., Metal/air batteries: their status and potential—a review. *J. Power Sources* **1979,** *4* (4), 263-279.

24. Rahman, M. A.; Wang, X.; Wen, C., High energy density metal-air batteries: a review. *J. Electrochem. Soc.* **2013,** *160* (10), A1759-A1771.

25. Weber, A. Z.; Mench, M. M.; Meyers, J. P.; Ross, P. N.; Gostick, J. T.; Liu, Q. J. J. o. A. E., Redox flow batteries: a review. *J. Appl. Electrochem.* **2011,** *41* (10), 1137.

26. Parasuraman, A.; Lim, T. M.; Menictas, C.; Skyllas-Kazacos, M., Review of material research

and development for vanadium redox flow battery applications. *Electrochim. Acta* **2013,** *101*, 27-40.

27. Kear, G.; Shah, A. A.; Walsh, F. C., Development of the all-vanadium redox flow battery for energy storage: a review of technological, financial and policy aspects. *International journal of energy research* **2012,** *36* (11), 1105-1120.

28. McCloskey, B. D., Expanding the Ragone Plot: Pushing the Limits of Energy Storage. *J. Phys. Chem. Lett.* **2015,** *6* (18), 3592-3593.

29. Thackeray, M. M.; Wolverton, C.; Isaacs, E. D., Electrical energy storage for transportation—approaching the limits of, and going beyond, lithium-ion batteries. *Energy Environ. Sci.* **2012,** *5* (7), 7854-7863.

30. Xiao, J.; Chernova, N. A.; Whittingham, M. S., Layered mixed transition metal oxide cathodes with reduced cobalt content for lithium ion batteries. *Chem. Mater.* **2008,** *20* (24), 7454-7464.

31. Sun, Y.-K.; Lee, D.-J.; Lee, Y. J.; Chen, Z.; Myung, S.-T., Cobalt-free nickel rich layered oxide cathodes for lithium-ion batteries. *ACS Appl. Mater. Interfaces* **2013,** *5* (21), 11434-11440.

32. Karthikeyan, K.; Amaresh, S.; Lee, G.; Aravindan, V.; Kim, H.; Kang, K.; Kim, W.; Lee, Y., Electrochemical performance of cobalt free, $Li_{1.2}(Mn_{0.32}Ni_{0.32}Fe_{0.16})O_2$ cathodes for lithium batteries. *Electrochim. Acta* **2012,** *68*, 246-253.

33. Wu, F.; Zhang, X.; Zhao, T.; Li, L.; Xie, M.; Chen, R., Surface modification of a cobalt-free layered $Li[Li_{0.2}Fe_{0.1}Ni_{0.15}Mn_{0.55}]O_2$ oxide with the $FePO_4/Li_3PO_4$ composite as the cathode for lithium-ion batteries. *J. Mater. Chem. A* **2015,** *3* (18), 9528-9537.

34. Abirami, M.; Hwang, S. M.; Yang, J.; Senthilkumar, S. T.; Kim, J.; Go, W. S.; Senthilkumar, B.; Song, H. K.; Kim, Y., A Metal-Organic Framework Derived Porous Cobalt Manganese Oxide Bifunctional Electrocatalyst for Hybrid Na-Air/Seawater Batteries. *ACS Appl. Mater. Interfaces* **2016,** *8* (48), 32778-32787.

35. Hwang, S. M.; Kim, J.; Kim, Y.; Kim, Y., Na-ion storage performance of amorphous Sb_2S_3nanoparticles: anode for Na-ion batteries and seawater flow batteries. *J. Mater. Chem. A* **2016,** *4* (46), 17946-17951.

36. Kim, J.-K.; Lee, E.; Kim, H.; Johnson, C.; Cho, J.; Kim, Y., Rechargeable Seawater Battery

and Its Electrochemical Mechanism. *ChemElectroChem* **2015,** *2* (3), 328-332.

37. Kim, Y.; Kim, H.; Park, S.; Seo, I.; Kim, Y., Na ion- Conducting Ceramic as Solid Electrolyte for Rechargeable Seawater Batteries. *Electrochim. Acta* **2016,** *191*, 1-7.

38. Sahgong, S. H.; Senthilkumar, S. T.; Kim, K.; Hwang, S. M.; Kim, Y., Rechargeable aqueous Na–air batteries: Highly improved voltage efficiency by use of catalysts. *Electrochem. Commun.* **2015,** *61*, 53-56.

39. Senthilkumar, S. T.; Park, S. O.; Kim, J.; Hwang, S. M.; Kwak, S. K.; Kim, Y., Seawater battery performance enhancement enabled by a defect/edge-rich, oxygen self-doped porous carbon electrocatalyst. *J. Mater. Chem. A* **2017,** *5* (27), 14174-14181.

40. Han, J.; Hwang, S. M.; Go, W.; Senthilkumar, S. T.; Jeon, D.; Kim, Y., Development of coin-type cell and engineering of its compartments for rechargeable seawater batteries. *J. Power Sources* **2018,** *374*, 24-30.

41. Hwang, S. M.; Go, W.; Yu, H.; Kim, Y., Hybrid Na–air flow batteries using an acidic catholyte: effect of the catholyte pH on the cell performance. *J. Mater. Chem. A* **2017,** *5* (23), 11592-11600.

42. Jeoung, S.; Sahgong, S. H.; Kim, J. H.; Hwang, S. M.; Kim, Y.; Moon, H. R., Upcycling of nonporous coordination polymers: controllable-conversion toward porosity-tuned N-doped carbons and their electrocatalytic activity in seawater batteries. *J. Mater. Chem. A* **2016,** *4* (35), 13468-13475.

43. Kim, J. K.; Mueller, F.; Kim, H.; Jeong, S.; Park, J. S.; Passerini, S.; Kim, Y., Eco-friendly Energy Storage System: Seawater and Ionic Liquid Electrolyte. *ChemSusChem* **2016,** *9* (1), 42-9.

44. Kim, J.-K.; Mueller, F.; Kim, H.; Bresser, D.; Park, J.-S.; Lim, D.-H.; Kim, G.-T.; Passerini, S.; Kim, Y., Rechargeable-hybrid-seawater fuel cell. *NPG Asia Materials* **2014,** *6* (11), e144-e144.

45. Kim, K.; Hwang, S. M.; Park, J.-S.; Han, J.; Kim, J.; Kim, Y., Highly improved voltage efficiency of seawater battery by use of chloride ion capturing electrode. *J. Power Sources* **2016,** *313*, 46-50.

46. Kim, Y.; Hwang, S. M.; Yu, H.; Kim, Y., High energy density rechargeable metal-free seawater batteries: a phosphorus/carbon composite as a promising anode material. *J. Mater. Chem. A* **2018,** *6* (7),

3046-3054.

47. Kim, Y.; Kim, J.-K.; Vaalma, C.; Bae, G. H.; Kim, G.-T.; Passerini, S.; Kim, Y., Optimized hard carbon derived from starch for rechargeable seawater batteries. *Carbon* **2018,** *129*, 564-571.

48. Manikandan, P.; Kishor, K.; Han, J.; Kim, Y., Advanced perspective on the synchronized bifunctional activities of P2-type materials to implement an interconnected voltage profile for seawater batteries. *J. Mater. Chem. A* **2018,** *6* (23), 11012-11021.

49. Park, S.; SenthilKumar, B.; Kim, K.; Hwang, S. M.; Kim, Y., Saltwater as the energy source for low-cost, safe rechargeable batteries. *J. Mater. Chem. A* **2016,** *4* (19), 7207-7213.

50. Zhang, Y.; Senthilkumar, S. T.; Park, J.; Park, J.; Kim, Y., A New Rechargeable Seawater Desalination Battery System. *Batteries Supercaps* **2018,** *1* (1), 6-10.

51. Bae, H.; Park, J.-S.; Senthilkumar, S. T.; Hwang, S. M.; Kim, Y., Hybrid seawater desalination-carbon capture using modified seawater battery system. *J. Power Sources* **2019,** *410-411*, 99-105.

52. Khan, Z.; Park, S. O.; Yang, J.; Park, S.; Shanker, R.; Song, H.-K.; Kim, Y.; Kwak, S. K.; Ko, H., Binary N,S-doped carbon nanospheres from bio-inspired artificial melanosomes: A route to efficient air electrodes for seawater batteries. *J. Mater. Chem. A* **2018,** *6* (47), 24459-24467.

53. Kim, D. H.; Choi, H.; Hwang, D. Y.; Park, J.; Kim, K. S.; Ahn, S.; Kim, Y.; Kwak, S. K.; Yu, Y.-J.; Kang, S. J., Reliable seawater battery anode: controlled sodium nucleation via deactivation of the current collector surface. *J. Mater. Chem. A* **2018,** *6* (40), 19672-19680.

54. Kim, Y.; Kim, G.-T.; Jeong, S.; Dou, X.; Geng, C.; Kim, Y.; Passerini, S., Large-scale stationary energy storage: Seawater batteries with high rate and reversible performance. *Energy Storage Mater.* **2019,** *16*, 56-64.

55. Shin, K. H.; Park, J.; Park, S. K.; Nakhanivej, P.; Hwang, S. M.; Kim, Y.; Park, H. S., Cobalt vanadate nanoparticles as bifunctional oxygen electrocatalysts for rechargeable seawater batteries. *Journal of Industrial and Engineering Chemistry* **2019,** *72*, 250-254.

56. Zhang, Y.; Park, J.-S.; Senthilkumar, S. T.; Kim, Y., A novel rechargeable hybrid Na-seawater flow battery using bifunctional electrocatalytic carbon sponge as cathode current collector. *J. Power*

Sources **2018,** *400*, 478-484.

57. Senthilkumar, S.; Abirami, M.; Kim, J.; Go, W.; Hwang, S. M.; Kim, Y., Sodium-ion hybrid electrolyte battery for sustainable energy storage applications. *J. Power Sources* **2017,** *341*, 404-410.

58. Senthilkumar, B.; Khan, Z.; Park, S.; Seo, I.; Ko, H.; Kim, Y., Exploration of cobalt phosphate as a potential catalyst for rechargeable aqueous sodium-air battery. *J. Power Sources* **2016,** *311*, 29-34.

59. Suh, D. H.; Park, S. K.; Nakhanivej, P.; Kim, Y.; Hwang, S. M.; Park, H. S., Hierarchically structured graphene-carbon nanotube-cobalt hybrid electrocatalyst for seawater battery. *J. Power Sources* **2017,** *372*, 31-37.

60. Hwang, S. M.; Park, J. S.; Kim, Y.; Go, W.; Han, J.; Kim, Y.; Kim, Y., Rechargeable Seawater Batteries—From Concept to Applications. *Adv. Mater.* **2018**, 1804936.

61. Wang, X. R.; Liu, J. Y.; Liu, Z. W.; Wang, W. C.; Luo, J.; Han, X. P.; Du, X. W.; Qiao, S. Z.; Yang, J., Identifying the Key Role of Pyridinic-N–Co Bonding in Synergistic Electrocatalysis for Reversible ORR/OER. *Adv. Mater.* **2018,** *30* (23), 1800005.

62. Jiao, Y.; Zheng, Y.; Jaroniec, M.; Qiao, S. Z., Design of electrocatalysts for oxygen-and hydrogen-involving energy conversion reactions. *Chem. Soc. Rev.* **2015,** *44* (8), 2060-2086.

63. Li, Z.; Luo, W.; Zhang, M.; Feng, J.; Zou, Z., Photoelectrochemical cells for solar hydrogen production: current state of promising photoelectrodes, methods to improve their properties, and outlook. *Energy Environ. Sci.* **2013,** *6* (2), 347-370.

64. Lee, Y.-L.; Chi, C.-F.; Liau, S.-Y., CdS/CdSe co-sensitized TiO_2 photoelectrode for efficient hydrogen generation in a photoelectrochemical cell. *Chem. Mater.* **2009,** *22* (3), 922-927.

65. Aroutiounian, V.; Arakelyan, V.; Shahnazaryan, G., Metal oxide photoelectrodes for hydrogen generation using solar radiation-driven water splitting. *Solar Energy* **2005,** *78* (5), 581-592.

66. Van de Krol, R.; Grätzel, M., *Photoelectrochemical hydrogen production*. Springer: **2012**; Vol. 90.

67. Minggu, L. J.; Daud, W. R. W.; Kassim, M. B., An overview of photocells and photoreactors for photoelectrochemical water splitting. *Int. J. Hydrogen Energy* **2010,** *35* (11), 5233-5244.

68. Sivula, K.; Van De Krol, R., Semiconducting materials for photoelectrochemical energy conversion.

Nat. Rev. Mater. **2016,** *1* (2), 15010.

69. Hwang, J.-Y.; Myung, S.-T.; Sun, Y.-K., Sodium-ion batteries: present and future. *Chem. Soc. Rev.* **2017,** *46* (12), 3529-3614.

70. Obrovac, M.; Chevrier, V., Alloy negative electrodes for Li-ion batteries. *Chem. Rev. (Washington, DC, U. S.)* **2014,** *114* (23), 11444-11502.

71. Gaines, L., The future of automotive lithium-ion battery recycling: Charting a sustainable course. *Sustainable Materials Technologies* **2014,** *1*, 2-7.

72. Qi, T.; Zhang, X.; Karplus, V. J., The energy and CO_2 emissions impact of renewable energy development in China. *Energy Policy* **2014,** *68*, 60-69.

73. Chen, H.; Cong, T. N.; Yang, W.; Tan, C.; Li, Y.; Ding, Y., Progress in electrical energy storage system: A critical review. *Progress in Natural Science* **2009,** *19* (3), 291-312.

74. Thackeray, M. M.; Wolverton, C.; Isaacs, E. D., Electrical energy storage for transportation—approaching the limits of, and going beyond, lithium-ion batteries. *Energy Environ. Sci.* **2012,** *5* (7), 7854.

75. Kim, J.-K.; Mueller, F.; Kim, H.; Bresser, D.; Park, J.-S.; Lim, D.-H.; Kim, G.-T.; Passerini, S.; Kim, Y., Rechargeable-hybrid-seawater fuel cell. *NPG Asia Materials* **2014,** *6* (11), e144.

76. Kim, H.; Park, J.-S.; Sahgong, S. H.; Park, S.; Kim, J.-K.; Kim, Y., Metal-free hybrid seawater fuel cell with an ether-based electrolyte. *J. Mater. Chem. A* **2014,** *2* (46), 19584-19588.

77. Senthilkumar, S. T.; Abirami, M.; Kim, J.; Go, W.; Hwang, S. M.; Kim, Y., Sodium-ion hybrid electrolyte battery for sustainable energy storage applications. *J. Power Sources* **2017,** *341*, 404-410.

78. Senthilkumar, S. T.; Park, S. O.; Kim, J.; Hwang, S. M.; Kwak, S. K.; Kim, Y., Seawater battery performance enhancement enabled by a defect/edge-rich, oxygen self-doped porous carbon electrocatalyst. *J. Mater. Chem. A* **2017**.

79. Hwang, S. M.; Kim, J.; Kim, Y.; Kim, Y., Na-ion storage performance of amorphous Sb2S3 nanoparticles: anode for Na-ion batteries and seawater flow batteries. *J. Mater. Chem. A* **2016,** *4* (46), 17946-17951.

80. Jeoung, S.; Sahgong, S. H.; Kim, J. H.; Hwang, S. M.; Kim, Y.; Moon, H. R., Upcycling of nonporous coordination polymers: controllable-conversion toward porosity-tuned N-doped carbons and their electrocatalytic activity in seawater batteries. *J. Mater. Chem. A* **2016,** *4* (35), 13468-13475.

81. Wang, W. H.; Wang, X. D., Investigation of Ir-modified carbon felt as the positive electrode of an all-vanadium redox flow battery. *Electrochimica Acta* **2007,** *52* (24), 6755-6762.

82. Chakrabarti, M. H.; Brandon, N. P.; Hajimolana, S. A.; Tariq, F.; Yufit, V.; Hashim, M. A.; Hussain, M. A.; Low, C. T. J.; Aravind, P. V., Application of carbon materials in redox flow batteries. *J. Power Sources* **2014,** *253*, 150-166.

83. Kim, K. J.; Kim, Y.-J.; Kim, J.-H.; Park, M.-S., The effects of surface modification on carbon felt electrodes for use in vanadium redox flow batteries. *Mater. Chem. Phys.* **2011,** *131* (1-2), 547-553.

84. Tao, L.; Wang, Q.; Dou, S.; Ma, Z.; Huo, J.; Wang, S.; Dai, L., Edge-rich and dopant-free graphene as a highly efficient metal-free electrocatalyst for the oxygen reduction reaction. *Chem. Commun.* **2016,** *52* (13), 2764-7.

85. Yoo, E.; Zhou, H., Li− air rechargeable battery based on metal-free graphene nanosheet catalysts. *ACS nano* **2011,** *5* (4), 3020-3026.

86. Hwang, S. M.; Go, W.; Yu, H.; Kim, Y., Hybrid Na–air flow batteries using an acidic catholyte: effect of the catholyte pH on the cell performance. *J. Mater. Chem. A* **2017,** *5* (23), 11592-11600.

87. Neburchilov, V.; Wang, H.; Martin, J. J.; Qu, W., A review on air cathodes for zinc–air fuel cells. *J. Power Sources* **2010,** *195* (5), 1271-1291.

88. Lu, Y.; Goodenough, J. B.; Kim, Y., Aqueous Cathode for Next-Generation Alkali-Ion Batteries. *J. Am. Chem. Soc.* **2011,** *133* (15), 5756-5759.

89. Nie, Y.; Li, L.; Wei, Z., Recent advancements in Pt and Pt-free catalysts for oxygen reduction reaction. *Chem Soc Rev* **2015,** *44* (8), 2168-201.

90. Azevedo, J.; Seipp, T.; Burfeind, J.; Sousa, C.; Bentien, A.; Araújo, J. P.; Mendes, A., Unbiased solar energy storage: Photoelectrochemical redox flow battery. *Nano Energy* **2016,** *22*, 396-405.

91. Li, Q.; Li, N.; Liu, Y.; Wang, Y.; Zhou, H., High-Safety and Low-Cost Photoassisted

Chargeable Aqueous Sodium-Ion Batteries with 90% Input Electric Energy Savings. *Adv. Energy Mater.* **2016,** *6* (18), 1600632.

92. Liu, Y.; Li, N.; Liao, K.; Li, Q.; Ishida, M.; Zhou, H., Lowering the charge voltage of Li–O2 batteries via an unmediated photoelectrochemical oxidation approach. *J. Mater. Chem. A* **2016,** *4* (32), 12411-12415.

93. Nakata, K.; Fujishima, A., TiO_2 photocatalysis: Design and applications. *Journal of Photochemistry and Photobiology C: Photochemistry Reviews* **2012,** *13* (3), 169-189.

94. Mishra, M.; Chun, D.-M., α-Fe $_2$ O $_3$ as a photocatalytic material: A review. *Applied Catalysis A: General* **2015,** *498*, 126-141.

95. Szilágyi, I. M.; Fórizs, B.; Rosseler, O.; Szegedi, Á.; Németh, P.; Király, P.; Tárkányi, G.; Vajna, B.; Varga-Josepovits, K.; László, K.; Tóth, A. L.; Baranyai, P.; Leskelä, M., WO_3 photocatalysts: Influence of structure and composition. *J. Catal.* **2012,** *294*, 119-127.

96. Kang, D.; Kim, T. W.; Kubota, S. R.; Cardiel, A. C.; Cha, H. G.; Choi, K. S., Electrochemical Synthesis of Photoelectrodes and Catalysts for Use in Solar Water Splitting. *Chem. Rev. (Washington, DC, U. S.)* **2015,** *115* (23), 12839-87.

97. Wang, G.; Wang, H.; Ling, Y.; Tang, Y.; Yang, X.; Fitzmorris, R. C.; Wang, C.; Zhang, J. Z.; Li, Y., Hydrogen-treated TiO_2 nanowire arrays for photoelectrochemical water splitting. *Nano Lett.* **2011,** *11* (7), 3026-3033.

98. Khan, S. U.; Al-Shahry, M.; Ingler, W. B., Efficient photochemical water splitting by a chemically modified n-TiO_2. *science* **2002,** *297* (5590), 2243-2245.

99. Yu, J.; Qi, L.; Jaroniec, M., Hydrogen production by photocatalytic water splitting over Pt/TiO_2 nanosheets with exposed (001) facets. *J. Phys. Chem. C* **2010,** *114* (30), 13118-13125.

100. Pu, Y.-C.; Wang, G.; Chang, K.-D.; Ling, Y.; Lin, Y.-K.; Fitzmorris, B. C.; Liu, C.-M.; Lu, X.; Tong, Y.; Zhang, J. Z., Au nanostructure-decorated TiO_2 nanowires exhibiting photoactivity across entire UV-visible region for photoelectrochemical water splitting. *Nano Lett.* **2013,** *13* (8), 3817-3823.

101. Galińska, A.; Walendziewski, J., Photocatalytic water splitting over Pt− TiO_2 in the presence of

sacrificial reagents. *Energy Fuels* **2005,** *19* (3), 1143-1147.

102. Sivula, K.; Le Formal, F.; Grätzel, M., Solar water splitting: progress using hematite (α-Fe_2O_3) photoelectrodes. *ChemSusChem* **2011,** *4* (4), 432-449.

103. Sivula, K.; Formal, F. L.; Gratzel, M., WO_3− Fe_2O_3 photoanodes for water splitting: A host scaffold, guest absorber approach. *Chem. Mater.* **2009,** *21* (13), 2862-2867.

104. Thimsen, E.; Le Formal, F.; Gratzel, M.; Warren, S. C., Influence of plasmonic Au nanoparticles on the photoactivity of Fe_2O_3 electrodes for water splitting. *Nano Lett.* **2010,** *11* (1), 35-43.

105. She, X.; Wu, J.; Xu, H.; Zhong, J.; Wang, Y.; Song, Y.; Nie, K.; Liu, Y.; Yang, Y.; Rodrigues, M. T. F., High Efficiency Photocatalytic Water Splitting Using 2D α-Fe_2O_3/g-C_3N_4 Z-Scheme Catalysts. *Adv. Energy Mater.* **2017,** *7* (17), 1700025.

106. Su, J.; Guo, L.; Bao, N.; Grimes, C. A., Nanostructured WO_3/$BiVO_4$ heterojunction films for efficient photoelectrochemical water splitting. *Nano Lett.* **2011,** *11* (5), 1928-1933.

107. Cristino, V.; Caramori, S.; Argazzi, R.; Meda, L.; Marra, G. L.; Bignozzi, C. A., Efficient photoelectrochemical water splitting by anodically grown WO3 electrodes. *Langmuir* **2011,** *27* (11), 7276-7284.

108. Tacca, A.; Meda, L.; Marra, G.; Savoini, A.; Caramori, S.; Cristino, V.; Bignozzi, C. A.; Pedro, V. G.; Boix, P. P.; Gimenez, S., Photoanodes based on nanostructured WO3 for water splitting. *ChemPhysChem* **2012,** *13* (12), 3025-3034.

109. Ni, M.; Leung, M. K.; Leung, D. Y.; Sumathy, K. J. R., A review and recent developments in photocatalytic water-splitting using TiO_2 for hydrogen production. *Renew. Sustain. Energy Rev* **2007,** *11* (3), 401-425.

110. Hwang, S. M.; Park, J. S.; Kim, Y.; Go, W.; Han, J.; Kim, Y.; Kim, Y., Rechargeable Seawater Batteries-From Concept to Applications. *Adv. Mater.* **2018**, e1804936.

111. Yang, X.; Wolcott, A.; Wang, G.; Sobo, A.; Fitzmorris, R. C.; Qian, F.; Zhang, J. Z.; Li, Y., Nitrogen-doped ZnO nanowire arrays for photoelectrochemical water splitting. *Nano Lett.* **2009,** *9* (6), 2331-2336.

112. Wolcott, A.; Smith, W. A.; Kuykendall, T. R.; Zhao, Y.; Zhang, J. Z., Photoelectrochemical study of nanostructured ZnO thin films for hydrogen generation from water splitting. *Adv. Funct. Mater.* **2009,** *19* (12), 1849-1856.

113. Chen, H. M.; Chen, C. K.; Chang, Y. C.; Tsai, C. W.; Liu, R. S.; Hu, S. F.; Chang, W. S.; Chen, K. H., Quantum dot monolayer sensitized ZnO nanowire-array photoelectrodes: true efficiency for water splitting. *Angew. Chem. Int. Ed.* **2010,** *49* (34), 5966-5969.

114. Momeni, M. M.; Ghayeb, Y., Visible light-driven photoelectrochemical water splitting on ZnO–TiO_2 heterogeneous nanotube photoanodes. *Journal of Applied Electrochemistry* **2015,** *45* (6), 557-566.

115. Sathish, M.; Viswanathan, B.; Viswanath, R., Alternate synthetic strategy for the preparation of CdS nanoparticles and its exploitation for water splitting. *Int. J. Hydrogen Energy* **2006,** *31* (7), 891-898.

116. Yin, Y.; Jin, Z.; Hou, F., Enhanced solar water-splitting efficiency using core/sheath heterostructure CdS/TiO_2 nanotube arrays. *Nanotechnology* **2007,** *18* (49), 495608.

117. Xu, Y.; Zhao, W.; Xu, R.; Shi, Y.; Zhang, B., Synthesis of ultrathin CdS nanosheets as efficient visible-light-driven water splitting photocatalysts for hydrogen evolution. *Chem. Commun. (Cambridge, U. K.)* **2013,** *49* (84), 9803-9805.

118. Wei, R.-B.; Kuang, P.-Y.; Cheng, H.; Chen, Y.-B.; Long, J.-Y.; Zhang, M.-Y.; Liu, Z.-Q., Plasmon-enhanced photoelectrochemical water splitting on gold nanoparticle decorated ZnO/CdS nanotube arrays. *ACS Sustainable Chemistry & Engineering* **2017,** *5* (5), 4249-4257.

119. Kim, T. W.; Choi, K.-S., Nanoporous $BiVO_4$ photoanodes with dual-layer oxygen evolution catalysts for solar water splitting. *Science* **2014,** *343* (6174), 990-994.

120. Ng, Y. H.; Iwase, A.; Kudo, A.; Amal, R., Reducing graphene oxide on a visible-light $BiVO_4$ photocatalyst for an enhanced photoelectrochemical water splitting. *J. Phys. Chem. Lett.* **2010,** *1* (17), 2607-2612.

121. Pihosh, Y.; Turkevych, I.; Mawatari, K.; Uemura, J.; Kazoe, Y.; Kosar, S.; Makita, K.; Sugaya, T.; Matsui, T.; Fujita, D., Photocatalytic generation of hydrogen by core-shell WO_3/$BiVO_4$ nanorods with ultimate water splitting efficiency. *Sci. Rep.* **2015,** *5*, 11141.

122. Ding, C.; Shi, J.; Wang, D.; Wang, Z.; Wang, N.; Liu, G.; Xiong, F.; Li, C., Visible light driven overall water splitting using cocatalyst/$BiVO_4$ photoanode with minimized bias. *Phys. Chem. Chem. Phys.* **2013,** *15* (13), 4589-4595.

123. Jia, Q.; Iwase, A.; Kudo, A., $BiVO_4$–Ru/$SrTiO_3$: Rh composite Z-scheme photocatalyst for solar water splitting. *Chem. Sci.* **2014,** *5* (4), 1513-1519.

124. Saito, R.; Miseki, Y.; Sayama, K., Highly efficient photoelectrochemical water splitting using a thin film photoanode of $BiVO_4$/SnO_2/WO_3 multi-composite in a carbonate electrolyte. *Chem. Commun. (Cambridge, U. K.)* **2012,** *48* (32), 3833-3835.

125. Ye, S.; Wang, R.; Wu, M.-Z.; Yuan, Y.-P., A review on g-C_3N_4 for photocatalytic water splitting and CO2 reduction. *Appl. Surf. Sci.* **2015,** *358*, 15-27.

126. Che, W.; Cheng, W.; Yao, T.; Tang, F.; Liu, W.; Su, H.; Huang, Y.; Liu, Q.; Liu, J.; Hu, F., Fast photoelectron transfer in (Cring)–C_3N_4 plane heterostructural nanosheets for overall water splitting. *J. Am. Chem. Soc.* **2017,** *139* (8), 3021-3026.

127. Yan, J.; Wu, H.; Chen, H.; Zhang, Y.; Zhang, F.; Liu, S. F., Fabrication of TiO_2/C_3N_4 heterostructure for enhanced photocatalytic Z-scheme overall water splitting. *Applied Catalysis B: Environmental* **2016,** *191*, 130-137.

128. Li, Z.; Kong, C.; Lu, G., Visible photocatalytic water splitting and photocatalytic two-electron oxygen formation over Cu-and Fe-doped g-C_3N_4. *J. Phys. Chem. C* **2015,** *120* (1), 56-63.

129. Higashi, M.; Domen, K.; Abe, R., Highly stable water splitting on oxynitride TaON photoanode system under visible light irradiation. *J. Am. Chem. Soc.* **2012,** *134* (16), 6968-6971.

130. Abe, R.; Higashi, M.; Domen, K., Facile fabrication of an efficient oxynitride TaON photoanode for overall water splitting into H_2 and O_2 under visible light irradiation. *J. Am. Chem. Soc.* **2010,** *132* (34), 11828-11829.

131. Liu, Z.; Zhang, Q.; Zhao, T.; Zhai, J.; Jiang, L., 3-D vertical arrays of TiO_2 nanotubes on Ti meshes: Efficient photoanodes for water photoelectrolysis. *J. Mater. Chem.* **2011,** *21* (28).

132. Bu, X.-Z.; Zhang, G.-K.; Gao, Y.-Y.; Yang, Y.-Q. J. M., Preparation and photocatalytic properties of visible light responsive N-doped TiO_2/rectorite composites. *Microporous mesoporous*

materials **2010,** *136* (1-3), 132-137.

133. Kubo, T.; Nakahira, A., Local structure of TiO_2-derived nanotubes prepared by the hydrothermal process. *J. Phys. Chem. C* **2008,** *112* (5), 1658-1662.

134. Zhang, Z.; Wang, P., Optimization of photoelectrochemical water splitting performance on hierarchical TiO_2 nanotube arrays. *Energy Environ. Sci.* **2012,** *5* (4).

135. Zhang, X.; Cui, H.; Humayun, M.; Qu, Y.; Fan, N.; Sun, X.; Jing, L., Exceptional performance of photoelectrochemical water oxidation of single-crystal rutile TiO_2 nanorods dependent on the hole trapping of modified chloride. *Sci. Rep.* **2016,** *6*, 21430.

136. Pandolfo, A. G.; Hollenkamp, A. F., Carbon properties and their role in supercapacitors. *J. Power Sources* **2006,** *157* (1), 11-27.

137. Zhang, L. L.; Zhao, X. S., Carbon-based materials as supercapacitor electrodes. *Chem. Soc. Rev.* **2009,** *38* (9), 2520-31.

138. Chevrier, V. L.; Ceder, G., Challenges for Na-ion Negative Electrodes. *J. Electrochem. Soc.* **2011,** *158* (9).

139. Ellis, L. D.; Wilkes, B. N.; Hatchard, T. D.; Obrovac, M. N., In Situ XRD Study of Silicon, Lead and Bismuth Negative Electrodes in Nonaqueous Sodium Cells. *J. Electrochem. Soc.* **2014,** *161* (3), A416-A421.

140. Irisarri, E.; Ponrouch, A.; Palacin, M. R., Review—Hard Carbon Negative Electrode Materials for Sodium-Ion Batteries. *J. Electrochem. Soc.* **2015,** *162* (14), A2476-A2482.

141. Li, C.-H.; Sengodu, P.; Wang, D.-Y.; Kuo, T.-R.; Chen, C.-C., Highly stable cycling of a lead oxide/copper nanocomposite as an anode material in lithium ion batteries. *RSC Advances* **2015,** *5* (62), 50245-50252.

142. Nitta, N.; Wu, F.; Lee, J. T.; Yushin, G., Li-ion battery materials: present and future. *Materials Today* **2015,** *18* (5), 252-264.

143. Obrovac, M. N.; Chevrier, V. L., Alloy negative electrodes for Li-ion batteries. *Chem. Rev. (Washington, DC, U. S.)* **2014,** *114* (23), 11444-502.

144. Wood, S. M.; Klavetter, K. C.; Heller, A.; Mullins, C. B., Fast lithium transport in PbTe for

lithium-ion battery anodes. *J. Mater. Chem. A* **2014,** *2* (20).

145. Wood, S. M.; Pham, C. H.; Heller, A.; Mullins, C. B., Communication—Stages in the Dynamic Electrochemical Lithiation of Lead. *J. Electrochem. Soc.* **2016,** *163* (6), A1027-A1029.

146. Yuan, Z.; Peng, Z.; Chen, Y.; Liu, H., Synthesis and electrochemical performance of nanosized tin lead composite oxides as lithium storage materials. *Mater. Chem. Phys.* **2010,** *120* (2-3), 331-335.

147. Gaines, L., The future of automotive lithium-ion battery recycling: Charting a sustainable course. *Sustainable Materials and Technologies* **2014,** *1-2*, 2-7.

148. Jow, T.; Shacklette, L.; Maxfield, M.; Vernick, D., The role of conductive polymers in alkali-metal secondary electrodes. *J. Electrochem. Soc.* **1987,** *134* (7), 1730-1733.

149. Martos, M.; Morales, J.; Sanchez, L., Lead-based systems as suitable anode materials for Li-ion batteries. *Electrochim. Acta* **2003,** *48* (6), 615-621.

150. Wang, J.; King, P.; Huggins, R., Investigations of binary lithium-zinc, lithium-cadmium and lithium-lead alloys as negative electrodes in organic solvent-based electrolyte. *Solid State Ion.* **1986,** *20* (3), 185-189.

151. Cho, J.; Kim, C. S.; Yoo, S. I., Improvement of structural stability of $LiCoO_2$ cathode during electrochemical cycling by sol-gel coating of SnO_2. *Electrochemical Solid-State Letters* **2000,** *3* (8), 362-365.

152. Cho, J.; Kim, Y. J.; Park, B., Novel $LiCoO_2$ cathode material with Al_2O_3 coating for a Li ion cell. *Chem. Mater.* **2000,** *12* (12), 3788-3791.

153. Cho, J.; Kim, Y. J.; Park, B., $LiCoO_2$ cathode material that does not show a phase transition from hexagonal to monoclinic phase. *J. Electrochem. Soc.* **2001,** *148* (10), A1110-A1115.

154. Cho, J.-H.; Park, J.-H.; Lee, M.-H.; Song, H.-K.; Lee, S.-Y. J. E.; Science, E., A polymer electrolyte-skinned active material strategy toward high-voltage lithium ion batteries: a polyimide-coated $LiNi_{0.5}Mn_{1.5}O_4$ spinel cathode material case. *Energy Environ. Sci.* **2012,** *5* (5), 7124-7131.

155. Choi, N.-S.; Han, J.-G.; Ha, S.-Y.; Park, I.; Back, C.-K., Recent advances in the electrolytes for interfacial stability of high-voltage cathodes in lithium-ion batteries. *RSC Advances* **2015,** *5* (4), 2732-2748.

156. Gu, M.; Belharouak, I.; Zheng, J.; Wu, H.; Xiao, J.; Genc, A.; Amine, K.; Thevuthasan, S.; Baer, D. R.; Zhang, J.-G., Formation of the spinel phase in the layered composite cathode used in Li-ion batteries. *ACS Nano* **2012,** *7* (1), 760-767.

157. Guan, D.; Jeevarajan, J. A.; Wang, Y., Enhanced cycleability of $LiMn_2O_4$ cathodes by atomic layer deposition of nanosized-thin Al_2O_3 coatings. *Nanoscale* **2011,** *3* (4), 1465-1469.

158. Higuchi, M.; Katayama, K.; Azuma, Y.; Yukawa, M.; Suhara, M., Synthesis of LiFePO4 cathode material by microwave processing. *J. Power Sources* **2003,** *119*, 258-261.

159. Kosova, N.; Uvarov, N.; Devyatkina, E.; Avvakumov, E., Mechanochemical synthesis of $LiMn_2O_4$ cathode material for lithium batteries. *Solid State Ion.* **2000,** *135* (1-4), 107-114.

160. Lee, M.-J.; Lee, S.; Oh, P.; Kim, Y.; Cho, J., High performance $LiMn_2O_4$ cathode materials grown with epitaxial layered nanostructure for Li-ion batteries. *Nano Lett.* **2014,** *14* (2), 993-999.

161. Liu, H.; Cao, Q.; Fu, L. J.; Li, C.; Wu, Y.; Wu, H., Doping effects of zinc on $LiFePO_4$ cathode material for lithium ion batteries. *Electrochem. Commun.* **2006,** *8* (10), 1553-1557.

162. Song, Y.-M.; Kim, C.-K.; Kim, K.-E.; Hong, S. Y.; Choi, N.-S., Exploiting chemically and electrochemically reactive phosphite derivatives for high-voltage spinel $LiNi_{0.5}Mn_{1.5}O_4$ cathodes. *J. Power Sources* **2016,** *302*, 22-30.

163. Sun, Y.-K.; Han, J.-M.; Myung, S.-T.; Lee, S.-W.; Amine, K., Significant improvement of high voltage cycling behavior AlF_3-coated $LiCoO_2$ cathode. *Electrochem. Commun.* **2006,** *8* (5), 821-826.

164. Tang, D.; Sun, Y.; Yang, Z.; Ben, L.; Gu, L.; Huang, X., Surface structure evolution of $LiMn_2O_4$ cathode material upon charge/discharge. *Chem. Mater.* **2014,** *26* (11), 3535-3543.

165. Wang, D.; Wu, X.; Wang, Z.; Chen, L., Cracking causing cyclic instability of $LiFePO_4$ cathode material. *J. Power Sources* **2005,** *140* (1), 125-128.

166. Zhang, W.-J., Structure and performance of $LiFePO_4$ cathode materials: A review. *J. Power Sources* **2011,** *196* (6), 2962-2970.

Acknowledgements

4 년반의 짧은 대학원 생활을 마치고 이제 정든 실험실과 유니스트를 떠나려 합니다. 지금 와서 돌이켜보니 제 인생에 있어서 가장 중요한 시기가 아니었나 싶습니다. 우선, 생명공학부를 졸업해서 배터리에 관해서 아무런 지식도 없고, 군대에서 갓 제대한 학생을 포텐셜만 보고 선발해 주신 교수님께 감사의 말씀을 전하고 싶습니다. 교수님의 노력하시는 모습, 목표를 성취하기위해 끊임없이 고민하는 모습을 보면서 연구는 이렇게 하는거구나 하는 표본을 알게되었습니다. 이제는 교수님의 그늘에서 벗어나 교수님께서 항상 말씀하시는 문제해결능력을 더 키워서 독립적인 그리고 주도적인 연구자가 되도록 하겠습니다.

두번째로 랩 구성원 분들에게 감사의 말씀을 전하고 싶습니다. 늘 조언을 아끼지 않으신 황수민 박사님, 김경호 교수님, 매번 귀찮도록 질문을 많이 해도 이해하기 쉽도록 잘 설명해주는 용일이, 코인셀 엔지니어링 쪽으로 고민할 때 항상 아이디어를 제공해주는 원년맴버 정선이, 실험실의 궂은 일을 도맡아 희생하는 랩장 영준이, 힘들때 항상 웃게해주는 실험실 분위기메이커 현우, 착한 입학 동기 현태, 오피스 짝꿍 우석이, 긍정의 아이콘 제희, 실험실 맏형 영진이형님, 열심히 하려고 노력하는 진호, 얼굴도 마음도 예쁜 다송이, 잘생긴 몸짱 남혁이, 그리고 새로 들어온 신입생 Linh, 세영이, 원석이, 도완이에게도 감사의 말씀을 전합니다. 저 혼자라면 정말 힘들었을 길을 함께 걸어주어서 오늘의 영광이 있을 수 있었습니다.

마지막으로 저를 항상 응원해주는 가족들에게 감사의 말씀을 전하고 싶습니다. 지금은 하늘 나라에 계시지만 제가 박사가 되었다고 말씀드리면 누구보다 좋아하실 우리 아버지, 저를 위해 평생을 희생하면서 뒷바라지 해주시는 우리 엄마, 못난 동생이지만 항상 응원해주는 우리 누나와 매형, 10 년 동안 나만 바라보며 믿어주는 우리 지영이, 사랑하는 우리 딸 재이에게 고마운 마음을 전합니다. 이제는 듬직하고 든든한 아들이자 남편이자 아빠가 될 수 있도록 노력하겠습니다. 그리고 미국에서 저를 지도한다고 고생많으셨던 이응제 박사님, 항상 질문했을 때 친절하게 설명해주시는 김지현 박사님, 권법진 박사님께도 감사의 말씀을 전하고 싶습니다. 여기에 다 적지는 못했지만 저를 도와줬던 많은 분들께도 이자리를 통해 감사의 말씀을 전하고 싶습니다. 감사한 이 마음 평생 잊지 않겠습니다.

Permission from Elsevier B. V.